

VYSOKÉ UČENÍ TECHNICKÉ V BRNĚ
BRNO UNIVERSITY OF TECHNOLOGY



FAKULTA STROJNÍHO INŽENÝRSTVÍ
ÚSTAV MATEMATIKY
FACULTY OF MECHANICAL ENGINEERING
INSTITUTE OF MATHEMATICS

APPLICATION OF ADAPTIVE FILTERS IN PROCESSING OF SOLAR CORONA IMAGES

APLIKACE ADAPTIVNÍCH FILTRŮ PŘI ZPRACOVÁNÍ SNÍMKŮ SLUNEČNÍ KORÓNY

DIZERTAČNÍ PRÁCE
DOCTORAL THESIS

AUTOR PRÁCE
AUTHOR

Ing. HANA DRUCKMÜLLEROVÁ

VEDOUCÍ PRÁCE
SUPERVISOR

doc. PaedDr. DALIBOR MARTIŠEK, Ph.D.

BRNO 2014

Abstrakt

Fotografování sluneční koróny patří mezi nejobtížnější úlohy astrofotografie a zároveň je jednou z klíčových metod pro studium koróny. Tato práce přináší ucelený souhrn metod pro pozorování sluneční koróny pomocí snímků. Práce obsahuje nutnou matematickou teorii, postup pro zpracování snímků a souhrn adaptivních filtrů pro vizualizaci koronálních struktur v digitálních obrazech. Dále přináší návrh nových metod určených především pro obrazy s vyšším obsahem šumu, než je běžné u obrazů bílé koróny pořízených během úplných zatmění Slunce, např. pro obrazy pořízené pomocí úzkopásmových filtrů. Fourier normalizing-radial-graded filter, který byl navržen v rámci této práce, je založen na aproximaci hodnot pixelů a jejich variability pomocí trigonometrických polynomů s využitím dalších vlastností obrazu.

Abstract

Solar corona photography counts among the most complicated tasks in astrophotography. It also plays a key role for research of the solar corona. This thesis brings an a complete overview of methods for imaging the solar corona. The thesis contains necessary mathematical background, the sequence of steps for image processing, an overview of adaptive filters used for visualization of corona structures in digital images, and new methods are proposed, especially for images which contain more noise than it is typical for images of the white corona taken during total solar eclipses, e.g. images taken with narrow-band filters. The Fourier normalizing-radial-graded filter method that I proposed during my PhD study are based on approximation of pixel values and their variability with trigonometric polynomials using other properties of the image.

klíčová slova

sluneční koróna, adaptivní filtry, zpracování obrazů, Fourier normalizing-radial-graded filter

key words

solar corona, adaptive filters, image processing, Fourier normalizing-radial-graded filter

DRUCKMÜLLEROVÁ, H. Application of adaptive filters in processing of solar corona images. Brno: Vysoké učení technické v Brně, Fakulta strojního inženýrství, 2014. 120 s. Vedoucí dizertační práce doc. PaedDr. Dalibor Martišek, Ph.D.

I declare that I have written the doctoral thesis *Application of adaptive filters in processing of solar corona images* on my own according to advice of my supervisor doc. PaedDr. Dalibor Martišek, Ph.D., and using the sources listed in references.

March 31, 2014

Hana Druckmüllerová

I would like to express my gratitude to prof. Shadia Rifai Habbal, Ph.D. of Institute for Astronomy, University of Hawaii at Manoa for her hospitality during my stay at IfA UH in Honolulu, Hawaii in October 2010 to January 2011 and for the fruitful discussions we have had together.

I would like to express my gratitude to my father prof. RNDr. Miloslav Druckmüller, CSc. for showing me the beauty of total solar eclipses and passion for image processing.

Finally, I would like to thank my man Ing. Vladimír Kutálek, Ph.D. for his programming hints and inspirational comments to my work.

Contents

1	Introduction	3
2	Imaging the solar corona	5
2.1	The solar corona	5
2.2	Brightness gradient in the solar corona	6
2.3	Imaging possibilities for the solar corona	8
2.4	Methods of compensation for the brightness gradient	9
2.4.1	Mechanical and optical methods	9
2.4.2	Mathematical methods	12
3	Mathematical background	14
3.1	Digital image	14
3.1.1	Digital image as a function of two variables in Cartesian coordinates	14
3.1.2	Indexing a digital image in polar coordinates	16
3.2	Fourier transform	18
3.2.1	Fourier transform of functions $f : \mathbb{R}^2 \rightarrow \mathbb{C}$	18
3.2.2	Discrete Fourier transform	20
3.3	Image filters	25
3.3.1	Adaptive filters	26
3.3.2	Linear filters	26
4	Image acquisition and processing	30
4.1	White-light images acquired during total solar eclipses	30
4.1.1	Image acquisition	30
4.1.2	Image calibration	34
4.1.3	Image registration – phase correlation	41
4.1.4	Image composition	47
4.2	Images in spectral lines acquired during total solar eclipses	51
4.2.1	Importance of observations in spectral lines during total solar eclipses	51
4.2.2	Principle of observation in spectral lines in the visible part of the spectrum	53
4.2.3	Processing images in spectral lines	55
4.3	Images from cosmic probes	56
4.3.1	List of cosmic probes	56
4.3.2	Processing images from cosmic probes	61

5	Earlier filters for solar corona structure enhancement	63
5.1	Tangential filter	63
5.2	Adaptive convolution	66
5.3	Normalizing-radial-graded filter	68
5.4	Noise adaptive fuzzy equalization method	71
6	Fourier normalizing-radial-graded filter	74
6.1	The principle of the filter	74
6.1.1	The basic idea of the filter	75
6.1.2	Attenuation coefficients	78
6.1.3	Influence of additive noise	83
6.2	Results	85
6.2.1	Application to total solar eclipse observations	85
6.2.2	Application to space-based observations	87
6.2.3	Comparison with other methods	88
6.2.4	Other results – graphs of local brightness and contrast	91
6.3	Software implementation – FNRGF software	94
6.3.1	Parameters of the input file	95
6.3.2	Parameters of the FNRGF	96
6.3.3	Parameters of image display	98
6.3.4	Principles of the software implementation	99
6.3.5	FNRGF software user guide	101
7	Conclusion	105
	Bibliography	108
	Used symbols and abbreviations	118
A	Enclosed CD	120

Chapter 1

Introduction

The Sun is the nearest star to the Earth, therefore the research of the Sun gives the mankind a unique opportunity to study the physical parameters and properties of a star. Of course, there are both smaller and much bigger stars in the Universe, but the Sun is the most important star for us. The intensity and the spectral composition of the light emitted by the Sun as well as other particles that are spread from the Sun play a vital role for the life on the Earth. Since people are using more and more complicated electronic devices both on the Earth and in the Space and some of these devices are connected in large (global) networks, it is necessary to understand how and when the phenomena on the Sun can harm them.

As an example of what happened at a time when the electronics and computer networks were not as advanced as today can be the flare of March 9, 1989, when the subsequent geomagnetic storm caused the collapse of Hydro-Québec's electricity transmission system and other blackouts including a melted transformer in New Jersey, U.S.A. A very nice popular-scientific text on the danger of a massive solar flare including information about the March 1989 flare can be found on [dGre12]. A scientific article on this topic is for instance [cSta02]. Current electronic devices are even more sensitive than those in 1989.

Among other methods of the solar corona research, imaging methods play a crucial role. Due to the problems described in Chapter 2, sophisticated image processing techniques are necessary for taking full advantage of the current mechanical and optical systems for both Earth-based and space-born observations. Chapter 2 not only covers why it is complicated to take full advantage of the corona observations, but also gives a historical overview of mechanical and optical methods of solving these problems and an overview of numerical methods used from the early times of use of computers for image processing to nowadays. Chapter 3 describes the mathematical notions and theory that are necessary in the next chapters. Image acquisition and the steps of processing images (with mathematical reasoning) both from total solar eclipses and from cosmic probes together with a list of the most important cosmic probes that study the Sun is the content of Chapter 4. The final or almost-final step of the process is the enhancement of coronal structures. An overview of the most important methods which have been used for coronal structure enhancement can be found in Chapter 5.

Among them is the Normalizing-radial-graded filter (NRGF), which was the inspiration for the Fourier normalizing-radial-graded filter (FNRGF) proposed, implemented, and tested on many types of data as of part of my Ph.D. study and described in Chapter 6. The filter brings new possibilities for studying the corona, because its latest implementation

is relatively fast and some faint structures are enhanced better than with any of the previous methods. Chapter 6 not only describes the principle of the filter, but also its software implementation and contains many examples of images processed with this filter. Chapter 7 is the Conclusion followed by the Bibliography, and the List of used symbols and abbreviations and the description of the content of the CD which is enclosed to the thesis.

Chapter 2

Imaging the solar corona

2.1 The solar corona

The Sun can be divided into the interior and the atmosphere. The interior consists of the core, which is the source of the Sun’s energy, the place where hydrogen is transformed to heavier elements in thermonuclear reactions, the radiative zone, where energy is transmitted by radiation, and the convective zone. The Sun’s magnetic field has its origin in the transition layer between the radiative and the convective zone. The tops of the convective cells form the layer called the photosphere, which is also the border between the interior and the Sun’s atmosphere. The temperature of the photosphere is about 5 780 K. We often refer to the interior and the photosphere as ‘the Sun’, since the edge is clearly defined. The photosphere is what we see when we look at the Sun during a sunny day (with a suitable filter, otherwise we would risk damaging our eyes).

The solar atmosphere, which is above the photosphere, has only a fuzzy transition to the interplanetary space. The solar atmosphere comprises the chromosphere, the transition region, the corona, and the heliosphere. The chromosphere is a thin layer of variable thickness containing mainly neutral hydrogen. The temperature reaches its minimum between the photosphere and the chromosphere, where the temperature rises with height to about 20 000 K. Higher in the solar atmosphere, the notion of temperature becomes problematic, since the matter is so thin (would be called a good vacuum in an Earth-based laboratory) that it allows particles of very different energies to coexist in the same places. Observations and measurement report temperatures of 10^6 K and even higher in the corona. The temperature increase from 10^4 K to 10^6 K is found within about 500 km, less than a thousandth of the solar radius (the radius of the photosphere) [cGoP10].

Due to the extremely low density of the corona, there are extremely high-energy particles that are spread to the interplanetary space without having interfered with other particles [cHDM10b]. The origin of these particles and of their extremely high energy is still unknown – it is the so called ‘coronal heating problem’ (for a review on the coronal heating see e.g. [cBaO07]).

Since the corona is composed of plasma, the features that are visible in the corona from the extra-ultraviolet part of the spectrum to the infrared one are driven by the magnetic field that is generated in the transition region. The corona is extremely faint relatively to the visible disk of the Sun, having a maximum brightness ratio of $\approx 1 : 10^6$, decreasing to $\approx 10^6$ within a single diameter away from the visible limb. [cGoP10]. This is the

reason why the corona cannot be observed directly from the Earth without any special instruments – that it is too faint next to the bright photosphere. Section 2.3 is devoted to the possibilities that we have to observe the corona. An example of an image of the inner corona observed in the ultraviolet part of the spectrum can be found in Figure 2.1.

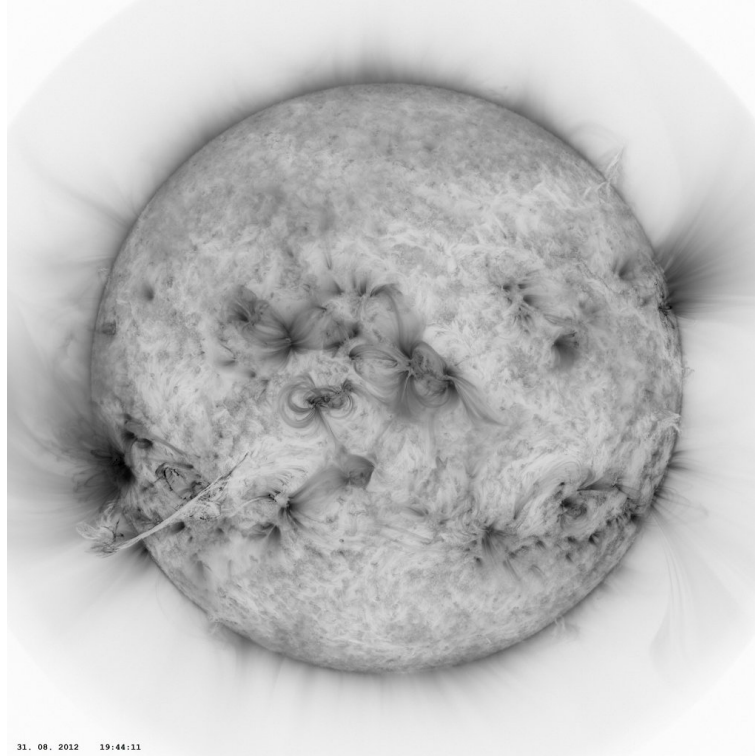


Figure 2.1: An image of the inner corona as observed by the Atmospheric Imaging Assembly, which is a part of the Solar Dynamics Observatory (NASA) in the ultraviolet part of the spectrum – 171 Å. For more information about this instrument see page 59 Image downloaded from [dVso13], in negative.

Due to the extreme brightness gradient in the corona, the photography of the inner corona counts among the most complicated tasks in astrophotography – the reasons to be discussed in details in Section 2.3. Therefore, sophisticated image processing methods have to be employed. The results of the processing can help to understand the processes in the corona and broaden our knowledge about the Sun.

2.2 Brightness gradient in the solar corona

The brightness of the corona is approximately exponentially decreasing with height above the photosphere, see the graphs in [cKSK78, cNDS70]. The decrease was described empirically for the first few solar radii with the Baumbach-Allen formula [cASC05]

$$n_e(R) = 10^8 \left(2.99 \left(\frac{R}{R_s} \right)^{-16} + 1.55 \left(\frac{R}{R_s} \right)^{-6} + 0.036 \left(\frac{R}{R_s} \right)^{-1.5} \right) \text{ cm}^{-3},$$

where n_e is the line-of-sight integrated density of the corona, which has three components: the K-corona (photospheric light scattered on free electrons), the E-corona (emission of

highly ionized atoms) and the F-corona (scattered light on dust particles). The light intensity is proportional to the density of the corona. There are newer measurements of the electron density, among the latest [cCLW09], whose results are presented in Figure 2.2.

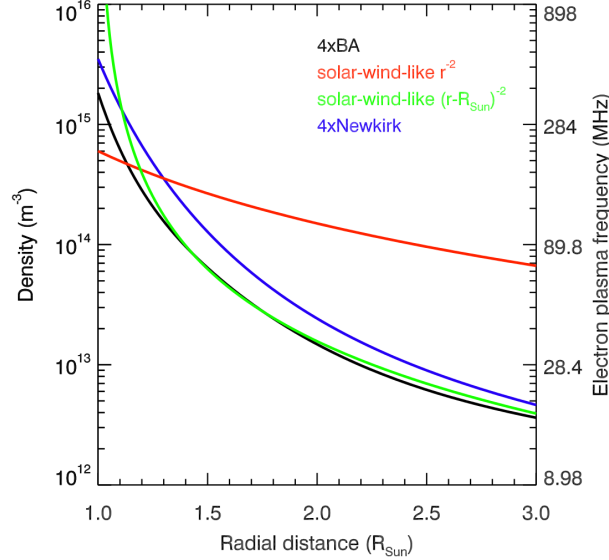


Figure 2.2: Comparison of different models of electron density taken from [cCLW09]. The black line is a renormalized Baumbach-Allen formula, the green line is work of [cCLW09], the blue line is a renormalized Newkirk formula [cNew61]. The red line is not of interest for our purpose here.

The radial brightness decrease can also be estimated with methods proposed in this thesis (FNRGF), even though they do not give absolute numbers on the y -axis as in Figure 2.2. With the distance from the Sun, not only the absolute brightness, but also the contrast of the structures decreases. This is illustrated by Figure 6.4c on page 82 and then further in Section 6.2.4.

The problem is that even if there was a method, either by means of classical or digital photography, to capture the whole brightness range in the field of view of a lens into one frame or image file, there is no technical means to make it visible for the human vision due to the enormous brightness range of the image. There is no printing method, screen or projector that would be capable of visualizing such high number of brightness levels. As a result, we are unable to directly interpret the information in the images. For viewing the images we need a method that removes information that is unnecessary for the human vision and lowers the dynamic range of the image from originally 16 or even more bits per pixel (in a gray-scale image) to 8 bits, since human vision is only able to distinguish about 150 to 250 levels of brightness in images with contrast typical for computer displays or for prints (depending on the conditions). Of course, the original high-dynamic-range images are necessary for photometric measurements alongside with structure-enhanced images that give us a clue what to focus on in the original images.

Remark 2.1. The term radial gradient is commonly used among solar astronomers. It means that the brightness gradient of the image is a vector whose direction is approximately radial, i.e. there is a high directional derivative of the image in the radial direction.

2.3 Imaging possibilities for the solar corona

Before the development of coronagraphic and later space-born observations, total solar eclipses provided the unique opportunity for exploring the properties of the plasma in the inner corona both through imaging and spectroscopy (we are not going to deal with spectroscopy in this thesis), since the photosphere, which is about one million times as bright as the inner corona, is obscured by the Moon and the sky brightness is significantly reduced. The invention of the coronagraph by Bernard Lyot in 1930 [cLyo32] brought completely new possibilities by enabling daily observations of the inner corona in visible light and in specific spectral lines as well as the polarization research. Current cosmic probes such as SOHO LASCO [cBHK95] still use coronagraphs. However, due to diffraction on the edge of the occulter (see Figure 2.3), the innermost part of up to 1.05 solar radii ($1.05 R_{\odot}$) the corona still remains unobservable with coronagraphs.

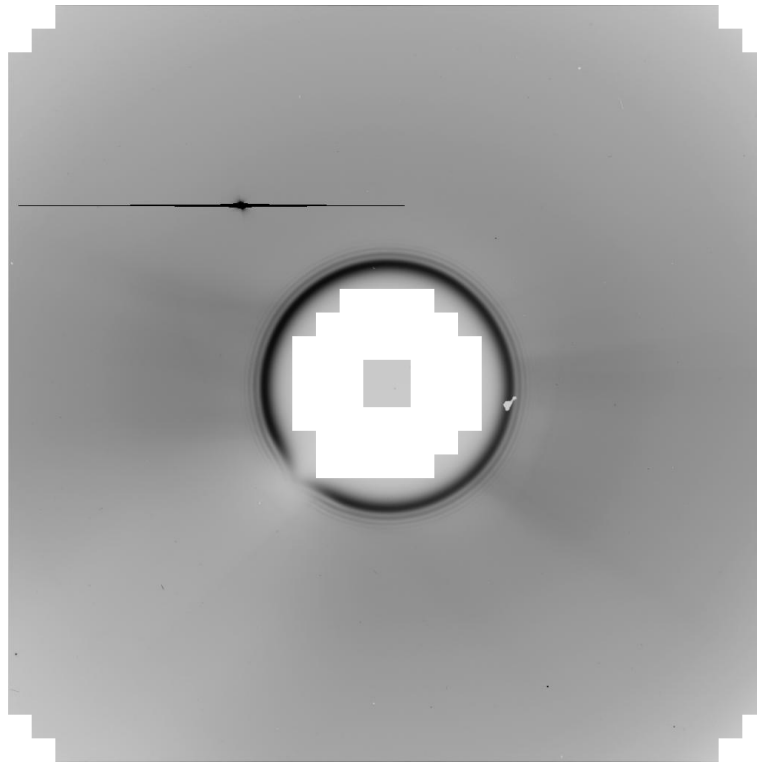


Figure 2.3: A sample image from LASCO C2 coronagraph (in negative). Blooming of the image of Venus and the diffraction patterns on the edge of the occulter are clearly visible. Downloaded from [dVso13].

A possibility to observe the innermost corona is imaging in the ultraviolet, extra-ultraviolet (EUV) part and X-ray wavelength ranges, where the photosphere is completely black. This has to be done from outside the Earth's atmosphere, which filters out ultraviolet and extra-ultraviolet radiation. Among the instruments that observe in EUV is the instrument SWAP in Proba2 cosmic probe (a project of Centre Spatial de Liège and the Royal Observatory of Belgium), which observes the radiation of Fe X at the wavelength of 17.4 nm (see page 60). However, such spectral lines are only collisionally excited and cannot be observed as high as the lines that have a radiative component as well, such as Fe X 637.4 nm, which have significantly higher wavelength. A comprehensive discussion

on the spectral lines with and without a radiative component, i.e. on the collisional and collisionless plasma is given in [aHDM11].

Even though there are sophisticated methods of continuous observation of the solar corona, the rare occasions of total solar eclipses are still the only times when the innermost corona can be observed in the visible part of the spectrum with by orders of magnitude cheaper equipment than spaceborn missions and with high resolution.

The process of acquisition and processing images of the solar corona mostly from total solar eclipses is described in Sections 4.1 and 4.2. The most important cosmic probes that study the Sun are listed in Section 4.3.1 together with methods of processing of these images.

2.4 Methods of compensation for the brightness gradient

2.4.1 Mechanical and optical methods

This section gives an overview of mechanical and optical methods used for removing the steep brightness gradient in the images of the solar corona, this means modifying the image before it is taken.

Rotating sector

The first attempts to use optical or mechanical methods to compensate for the steep decrease of brightness in the solar corona long before the era of digital photography were mechanical. They were prepared for the 1962 total solar eclipse by Owaki and Saito as a special rotating sector [cOwS67], which attenuated the brightness decrease, but its integrated transmission (over time when the sector is rotating) was not smooth enough. The profile of the sector is shown in Figure 2.4.

Radially graded filter

A step forward was made in early 1960s by Laffieneur and his colleagues [cGoP10] who pioneered the technique of a radially graded filter with density chosen to match the model of the average profile of the corona intensity. Newkirk and his colleagues [cNDS70], incorporated his own filter of similar properties in the optical system. He used a radially graded filter for some of his eclipse images from November 12, 1966 and later. The transmission function of the filter is shown in Figure 2.5. They state:

In order to photograph the entire corona with a single exposure, two frames were made through a radially graded, neutral filter whose transmission function was chosen to compensate for the steep decrease of coronal radiance with distance above the photosphere. We did not employ either of these photographs for quantitative analysis.

At their time, it was a big step forward to photograph the entire corona in a single frame and the technique was used over three decades as the best imaging technique for eclipse images of the corona.



Figure 2.4: The profile of the rotating sector of Owaki and Saito taken from [cOwS67]. As they say in their article, *this rotating sector vane, 82 mm in radius, was placed at the focal plane and driven at a speed of 750 rpm by a synchronous motor which is not visible.*

However, this approach has big drawbacks. First of all, the production of the radial filter is expensive. Moreover, the filter has to be centered precisely to the center of the Sun. Even with a precise mount and good observing conditions, it is not an easy task to center the center of the frame to the center of the Sun (which is obscured by the Moon), centering to the center of the Moon may not be precise enough. The photograph shows the corona in the whole field of view, but later photometric analysis and use of other image-processing techniques (that may even be invented after the photograph is taken) is very problematic, since the image has to be compensated for the filter before the analysis. The transmissivity of the filter has to be known with high precision and since the transmissivity differs in orders of magnitude, the compensation is numerically problematic.

Furthermore, the filter is more suited for eclipses during the maximum of solar activity, when the plumes and streamers are about evenly spread around the Sun. Otherwise the intensity profile is very different in different directions and the universal profile of the filter may cause misleading dark areas in the corona images during the solar minimum. In principle, it might be possible to use a filter that is not radially symmetric for these images. The transmission of such filter would have to take into account the predicted shape of the corona (for an example of the predicted shape of the corona for the 2008 eclipse see [cRDA10]). Such filters would have to be produced one-purpose for each eclipse and in a short time before the eclipse. Also the alignment of the filter is more complicated. For a radially symmetric filter, it is enough to center the filter to the center of the Sun. For the specially designed filter, it would also be necessary to set correctly the rotation of the filter.

Some observers used the Newkirk filter together with computer image processing techniques of composing images of different exposures and then enhancing coronal structures (see e.g. <http://touro.ligo-la.caltech.edu/~jkern/Eclipse01/>), but the explanation of some of the structures in the image may be rather complicated. Figure 2.6 shows

one of the images that Jonathan Kern (the author of the previous link) took together with Wendy Carlos and used for the composition.

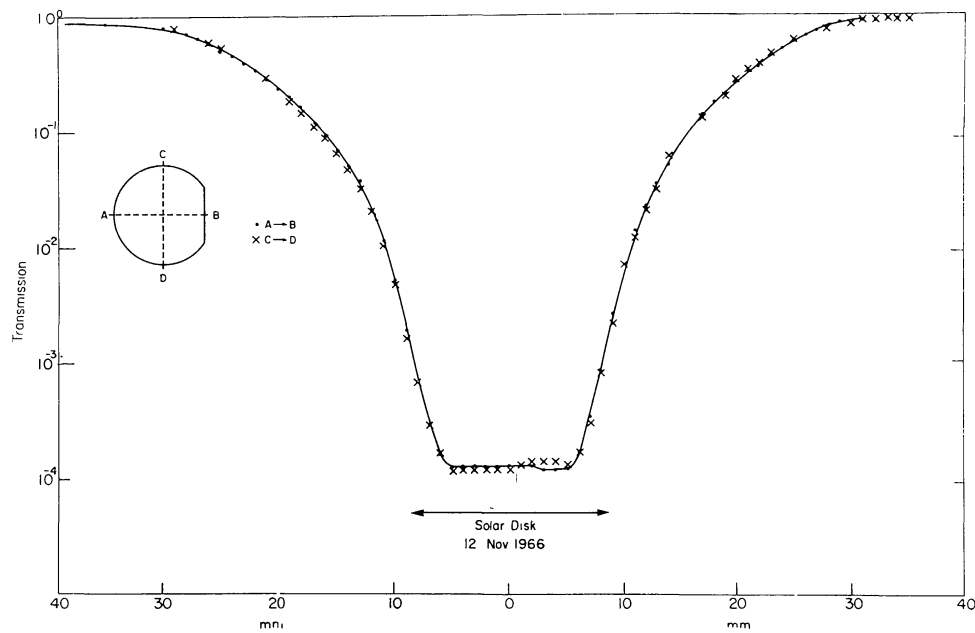


Figure 2.5: The transmission function of the radially graded filter used by Newkirk. Taken from [cNDS70].



Figure 2.6: An example of an image taken through the Newkirk filter. Downloaded from [dKer01]. Courtesy of Jonathan Kern and Wendy Carlos.

Modern negative films

Negative films since 1980s have been able to record a dynamic range of many stops (about 10, different sources give very different numbers). This made it possible to use techniques

such as moving a paper disk at various heights in the photographic enlarger between the head and the baseboard when producing a paper photograph. The information about the brightness in the whole corona was recorded in one frame and the purpose of the technique was to make it visible in a single photographic paper. The original negative films are untouched by image processing and can be later used for photometry or other image-processing techniques can be applied to them after digitalizing them. An example of the enormous dynamic range of negative films and of an image processed by a technique proposed after the image was taken is the image set by Ronald E. Royer of the eclipse in 1991, where the whole brightness range of the observed corona was recorded in a single frame of a $6\text{ cm} \times 6\text{ cm}$ negative film. The resulting image that I made together with my father with a description of the image set can be found on http://www.zam.fme.vutbr.cz/~druck/eclipse/Ecl1991m1/Tse1991rdd_c1/0-info.htm.

2.4.2 Mathematical methods

Since the 1980s, the increasing power of computers enabled software implementation of mathematical image-processing techniques and they can be more and more complicated with more powerful computers. Apart from classical high-pass filters with relatively small kernels of 3×3 or 5×5 pixels, which brought about significant noise enhancement, other methods of digital image processing were proposed, e.g. the MaD Max II method introduced by Olga Koutchmy and her colleagues [cKKN88]. The method is based on searching for the direction with the largest square of the second directional derivatives (or rather differences). As Koutchmy stated, the method gives less noisy images and is therefore suitable even for images recorded in spectral lines.

In late 1990s, the increasing power of computers made possible the use of larger kernels for filters and went together with the development of image processing software for common users. In 2000 Fred Espenak described a powerful technique for visualization of coronal structures in digitalized images which uses a common image-processing software – Adobe Photoshop [cEsp00]. This technique (with more details given in Section 5.1) and its variations have been commonly used since that time.

The method proposed and implemented by myself and by my father Miloslav Druckmüller [bDru03, aDru05, cDRM06] in the Corona software gives results that are closer to human sensation during the total solar eclipse (TSE), because they use multiple two-dimensional direction-invariant kernels with different sizes. This method, which is later referred to as the Adaptive Circular High-pass Filter (ACHF)¹ is described in Section 5.2.

The Normalizing-radial-graded-filter (NRGF) was published by Huw Morgan and his colleagues in 2006 [cMHW06]. It is completely automated, therefore it has been used as a standard tool for processing images from coronagraphs. Section 5.3 is dedicated to the NRGF.

During my Ph.D. study I proposed and implemented the Fourier normalizing-radial-graded filter (FNRGF), which was first published in [aDMH11]. It is inspired by the Normalizing-radial-graded filter. The FNRGF is described in Chapter 6.

¹I stick to the original capitalization and hyphenation in the names of filters taken from the articles where the name was first used. Therefore, there are different hyphenation and capitalization styles for different filters.

A recently developed method for visualization of structures in the solar corona on the solar disk (in extreme ultraviolet images) is the Noise adaptive fuzzy equalization method (NAFE) proposed, implemented, and published by my father Miloslav Druckmüller in [cDru13]. Its improvement accepted for publication [aDrD14] is our common work. This filter is described in Section 5.4.

Chapter 3

Mathematical background

In this chapter, I describe the mathematical background that is necessary for the applications in Chapters 4, 5, and 6. I state basic notions about digital images and mathematical tools for image processing and show the principle of transformation to polar coordinates that is necessary for the description of filters for solar corona structure enhancement including the FNRGF method. It is a special kind of transformation used for digital images that enables us to access the image in polar coordinates, but does not involve interpolation.

Some of the notions necessary for the image processing techniques described in the following chapters are well known mathematical tools, which therefore will not be explained here. Among them are the Fourier series, which are very well explained in [cBJS88] and [cFol92]. Image filters are broadly used, but the definition of a filter or even an adaptive filter is not given in most of the texts that deal with image filters, and if they are defined, the definition is not unified. Therefore a systematic introduction to image filters is given. The definitions of image noise in [aDru10] will be sufficient for this text. The topic of image noise involves some basic notions from probability and statistics, which can be found in [cLiM82] and [cWil01]. These are not repeated in the thesis.

3.1 Digital image

The digital image is defined in various ways depending among other aspects on the field the author specializes in and how technical or theoretical the text is. The definition that is used in this thesis was chosen so that the image can be read both in Cartesian and polar coordinates and so that we do not need to care about the dynamic range and rounding in pixel values.

3.1.1 Digital image as a function of two variables in Cartesian coordinates

Definition 3.1 (Gray-scale image). Let $M = \{0, 1, 2, \dots, w - 1\} \times \{0, 1, 2, \dots, h - 1\}$, where $w, h \in \mathbb{N}$, let $R \subset \mathbb{R}$. Function

$$f : M \rightarrow R$$

is called a *gray-scale image*. Numbers w and h are called the *image width* and *image height* respectively. Elements of $[x, y] \in M$ are called *pixels* and the value of function

f in pixel $[x, y]$, $f(x, y)$ is called the *pixel value*. The cardinality of R , $|R|$, is called the *dynamic range* of f . We say that the *dynamic range is n bits per pixel* (it is an n -bit image) if $R \subset \mathbb{Z}$ and $|R| = 2^d$ for a natural d .

Convention 3.2. In most parts of this thesis, we will not care about rounding and the dynamic range of the image. We will assume for simplicity that set R from the previous definition is the set of all real numbers, if not stated otherwise, and that all images have a dynamic range that is high enough for the image processing techniques.

The term *image matrix* is commonly used, because of the way how images are stored in computer memories. The only difference is that in mathematics, matrices are indexed from 1, whereas in computers they are commonly indexed from 0. Even though the image pixel values are stored in matrices, matrix operations such as multiplication do not have any sense for image matrices. This is the reason for defining images as functions with discrete domain. The image matrix then describes the pixel values of the image (as a function table).

Convention 3.3. For displaying an image, it is necessary to know the orientation of its axes. The images in this thesis have the origin $[0, 0]$ in the top left corner of the image matrix, which means that the orientation of the coordinate system in the image is left-handed.

An image taken with a digital camera usually has square sensors arranged in a rectangular grid, therefore if we assume a gray-scale image to take values in discrete points only, we have to keep in mind that the pixel values originated from integrals of the intensity of the light recorded over square areas. For simplicity, we can assume that the pixel value $f(x, y)$ is integrated over $\langle x - \frac{1}{2}, x + \frac{1}{2} \rangle \times \langle y - \frac{1}{2}, y + \frac{1}{2} \rangle$.

All images in the thesis will be gray-scale images if not stated otherwise. In most applications of the filters, the images that are processed have only one color component (images from coronagraphs, images in spectral lines). If the filters are used on color images, they have to be applied to the brightness / lightness component only. (A description of the hue-saturation-lightness/value (HSL / HSV) color spaces can be found on http://en.wikipedia.org/wiki/HSL_and_HSV.)

Let us define here the notion of a color image.

Definition 3.4 (Color image). Let $M = \{0, 1, 2, \dots, w - 1\} \times \{0, 1, 2, \dots, h - 1\}$, where $w, h \in \mathbb{N}$, let $R \subset \mathbb{R}^3$. The vector function

$$f(x, y) : M \rightarrow R, \quad f(x, y) = (r(x, y), g(x, y), b(x, y))$$

is called a *color image*. Functions r, g, b are called the *color components* of image f .

In the definition above, the color components r, g, b are most often used for the red, green and the blue components of the image. However, these triples can be converted to other spaces such as HSV or $YCbCr$ [cŽBF98], which also have three color components. There are also color images that have more than three color components, the other components have a different meaning – opacity (alpha channel), elevation etc. Most often, color images are stored in image matrices where each element of the matrix is a triple. Alternatively, color images are stored as three separate gray-scale images, each image for one color component.

3.1.2 Indexing a digital image in polar coordinates

Digital images are naturally stored in computer memories in Cartesian coordinates. It is how they are taken with digital cameras. However, since the solar corona is (very roughly said) circularly symmetric, many filters (such as ACHF (Section 5.2), NRGF (Section 5.3) and FNRGF (Chapter 6)) that enhance coronal structure are described in polar coordinates. Storing digital images in polar coordinates would mean that data originally taken in Cartesian coordinates are transformed to polar coordinates, which involves interpolation and in most cases also loss of information. Therefore the filters used for solar corona structure enhancement are applied to images stored in Cartesian coordinates with the possibility to index the image not only in Cartesian coordinates, but also in polar coordinates. The reasoning in this section gives us a tool for that, which enables us to switch between the Cartesian and polar coordinates (and back) without any difficulties.

Convention 3.5 (Center of the Sun). Since this thesis deals with processing of images of the solar corona, the information about the position of the Sun in the input images is a crucial input. It can be known with precision higher than one pixel. In the following text, the point $O = [o_x, o_y] \in \mathbb{R}^2$ will refer to the position of the center of the Sun in the image to be processed.

As some of the methods described in this thesis involve calculations on whole circles that lie completely in the image and cannot process parts of images that do not lie on any circle lying completely in the image, we will need the following denotations:

$$r_c = \min\{o_x, o_y, w - 1 - o_x, h - 1 - o_y\}$$

as the radius of the largest circle that has its center in the center of the Sun in the image and lies completely in the image and denote

$$M_o = \{A \in M, \text{Round}(\rho(A, O)) \leq r_c\}$$

as the part of the domain of the gray-scale image that lies inside or on that largest circle, ρ stands for the Euclidean metric.

Let \sim be the following binary relation on M_o :

$$A = [a_x, a_y] \sim B = [b_x, b_y] \quad \text{iff} \quad \text{Round}(\rho(A, O)) = \text{Round}(\rho(B, O)),$$

where Round means the rounding to the nearest integer. It is straightforward that \sim is reflexive, symmetric, and transitive, and thus is an equivalence relation. Each equivalence class contains pixels that have the same (rounded) distance from the center of the Sun in the image. The equivalence classes will be denoted by M_r , i.e.

$$M_r = \{A \in M_o, \text{Round}(\rho(A, O)) = r\}.$$

It further holds that for a fixed $r \in \{0, 1, 2, \dots, r_c\}$ and any $\varphi \in \langle 0, 2\pi \rangle$ there is at most one¹ $A \in M_r$ such that

$$\rho(A, O) \cos \varphi = a_x - o_x, \quad \rho(A, O) \sin \varphi = o_y - a_y. \quad (3.1)$$

¹Note that if the coordinates of the center of the Sun are integers, the set M_0 contains exactly one element, $M_0 = \{O\}$. In other cases, the set may contain either none or one element. For instance, if

The coordinates of A and O are swapped between the cosine and the sine, because the coordinate system of a gray-scale image is left-handed (due to the traditional way a computer screen is addressed), whereas the usual coordinate system where we are used to calculating sines and cosines is right-handed.

Proof. Let us suppose that there is a pixel A that satisfies Equations (3.1). And suppose that there is another $B \neq A, B \in M_r$ such that Equations (3.1) are satisfied for B . But since the distance of any two different pixels in the image C and D , $\rho(C, D) \geq 1$ and since both points A and B lie on the same ray starting in O , it must hold that

$$\rho(B, O) \geq \rho(A, O) + 1,$$

therefore

$$\text{Round}(\rho(B, O)) > \text{Round}(\rho(A, O)),$$

which is a contradiction. \square

Let $p : M_o \rightarrow \mathbb{N}_0 \times \langle 0, 2\pi \rangle$ be a vector function assigning to each pixel its rounded distance r from the center of the Sun, $r = \text{Round}(\rho(A, O))$, and oriented angle φ such that for $A = [x, y] \neq O$ equations (3.1) are satisfied. For $A = O$ define $p(A) = (0, 0)$. Let us denote

$$M_p = \{[r, \varphi] \in \mathbb{N}_0 \times \langle 0, 2\pi \rangle, \exists A \in M_o : p(A) = (r, \varphi)\}.$$

Then due to the reasoning above, p is a bijection between M_o and M_p .

Finally, it holds that

$$f(M_o) = f(p^{-1}(M_p))$$

as a gray-scale image restricted to M_o . This means that a gray-scale image restricted to M_o can equivalently be read in Cartesian coordinates (x, y) as well as heliocentric polar coordinates (r, φ) , where $r \in \{0, 1, 2, \dots, r_c\}$ and $\varphi \in \langle 0, 2\pi \rangle$ is a suitable number for which $p^{-1}(r, \varphi) \in \mathbb{N}_0^2$. This enables us to address the part of the image to be used for some of the filters in polar coordinates without any interpolation, which is exactly how the FNRGF (Chapter 6) is implemented.

Some other methods enable us to process also parts of images that do not lie on circles lying completely in the image. The reasoning above can be used in a similar way, the only difference would be that r_c will be replaced the distance between the center of the Sun in the image and the most distant pixel in the image and the whole image can be addressed equivalently in Cartesian and in heliocentric polar coordinates, which is used in the description of the tangential filter and the Adaptive-Circular-High-pass-Filter (ACHF) in Sections 5.1 and 5.2.

$O = [115.5, 116.5]$, the set M_0 is empty, since the nearest pixels are $\frac{\sqrt{2}}{2}$ far from O and they belong to M_1 . If $O = [115.9, 116.1]$, there is one element in M_0 , i.e. $[116, 116]$. In a special case when one of the coordinates of O is integer and the other is an integer plus one half, there are two pixels with distance 0.5 from the center of the Sun, but 0.5 is rounded to 1 and therefore $M_0 = \emptyset$ in this case. However, it is unimportant for the practical applications what the set M_0 looks like. The filters are applied out of the Moon (or an occulter) and the the interior of the Moon is irrelevant.

3.2 Fourier transform

The Fourier transform is an integral transform that transforms a function of one or more variables (in spatial domain) to another function (in frequency domain) of the same number of variables. Since the Fourier transform of a function is in the general case a function with a complex image and since a digital image is a function of two spatial variables, we will deal here for simplicity with functions $f : \mathbb{R}^2 \rightarrow \mathbb{C}$ in Section 3.2.1. The following Section 3.2.2 deals with the Fourier transform of functions with a square-organized discrete domain. Digital images are rectangles, for simplicity we deal here with square images only. All computations that use the Fourier transform are performed using the discrete Fourier transform (or more precisely by special algorithms that speed up the discrete Fourier transform, such as the Fast Fourier transform [cČíž81]). However, some derivations of image processing methods are better done with the Fourier transform of functions with the domain \mathbb{R}^2 since operations like rotation and rescaling are easily modeled on these functions. The connection between the Fourier transform of functions defined on \mathbb{R}^2 and the discrete Fourier transform is shown in a part of Section 3.2.2 which starts from page 23. Most of the definitions and theorems in this section are adapted from my master thesis [aDru10].

3.2.1 Fourier transform of functions $f : \mathbb{R}^2 \rightarrow \mathbb{C}$

The standard definition of the Fourier transform of a function of two variables is as follows.

Definition 3.6 (Fourier transform). Let $f(x, y) : \mathbb{R}^2 \rightarrow \mathbb{C}$ be a function such that

$$\iint_{\mathbb{R}^2} |f(x, y)| \, dx dy$$

exists and is finite. The *Fourier transform* of f is function $\mathcal{F}\{f\} = F(\xi, \eta)$ defined as

$$F(\xi, \eta) = \iint_{\mathbb{R}^2} f(x, y) e^{-i(x\xi + y\eta)} \, dx dy.$$

Function F is also called the *Fourier spectrum* of function f .

Other definition of the Fourier transform can be found in literature. They differ in a multiplicative constant before the integral or a multiplicative constant in the exponent.

The issue of integration over \mathbb{R}^2 is treated e.g. in [aDru10]. It is not unified in literature what the double integral over \mathbb{R}^2 means. Some definitions require integrals on parts of the domain to converge and the original integral exists only if all these integrals exist and converge, some definitions consider the integral in the sense of the Cauchy principal value. Different theorems can be proved with different definitions of the integral, therefore one has to be very careful when taking information about the Fourier transform from different sources.

Remark 3.7. The theory of distributions enables us to define the Fourier transform for a richer class of functions and even for distributions, which is necessary for working with functions which are as commonly used as $\sin x$. This topic is treated e.g. in [HuN01].

Definition 3.8 (Inverse Fourier transform). Let $F(\xi, \eta) : \mathbb{R}^2 \rightarrow \mathbb{C}$ be a function such that

$$\iint_{\mathbb{R}^2} |F(\xi, \eta)| \, d\xi d\eta$$

exists and is finite. The *inverse Fourier transform* of function F is function $\mathcal{F}^{-1}\{F\}(x, y) = f(x, y) : \mathbb{R}^2 \rightarrow \mathbb{C}$ defined as

$$f(x, y) = \frac{1}{4\pi^2} \iint_{\mathbb{R}^2} F(\xi, \eta) e^{i(x\xi + y\eta)} \, d\xi d\eta.$$

It is not true in general that the inverse Fourier transform of a Fourier transform of a function ($\mathcal{F}^{-1}\{\mathcal{F}\{f\}\}$) is the function itself. The inverse Fourier transform may not exist at all, if it exists, it may differ from the original function values. However, the following theorem was proved [cFol92, cStW75].

Theorem 3.9 (Fourier Inversion Theorem). Let $f(x, y) : \mathbb{R}^2 \rightarrow \mathbb{C}$ be a continuous function such that

$$\iint_{\mathbb{R}^2} |f(x, y)| \, dx dy$$

exists and is finite. Let $F(\xi, \eta)$ be the Fourier transform of f . Then for every $(\xi, \eta) \in \mathbb{R}^2$

$$f(x, y) = \lim_{\epsilon \rightarrow 0} \frac{1}{4\pi^2} \iint_{\mathbb{R}^2} F(\xi, \eta) e^{i(x\xi + y\eta)} e^{-\epsilon^2 \frac{\xi^2 + \eta^2}{2}} \, d\xi d\eta.$$

If also the integral

$$\iint_{\mathbb{R}^2} |F(\xi, \eta)| \, d\xi d\eta$$

exists and is finite, then

$$\mathcal{F}^{-1}\{\mathcal{F}\{f(x, y)\}\} = \frac{1}{4\pi^2} \iint_{\mathbb{R}^2} F(\xi, \eta) e^{i(x\xi + y\eta)} \, d\xi d\eta = f(x, y).$$

Since digital gray-scale images are defined only in a finite number of points, they can be approximated with arbitrarily smooth functions defined on \mathbb{R}^2 , which also have finite integrals of the absolute value and the same holds for the Fourier transform. Therefore, we do not need to worry about the ‘pathologic’ cases when $\mathcal{F}^{-1}\{\mathcal{F}\{f\}\} \neq f$.

The notions of the *amplitude spectrum* and *phase spectrum* are commonly used in image processing. Their definition follows.

Definition 3.10 (Amplitude spectrum, phase spectrum). Let function $f(x, y) \in \mathcal{L}(\mathbb{R}^2)$ have Fourier spectra $F(\xi, \eta)$. The *amplitude spectrum* [aDru10] of function f is a function $A(\xi, \eta) : \mathbb{R}^2 \rightarrow \mathbb{R}_0^+$ defined as

$$A(\xi, \eta) = |\mathcal{F}\{f(x, y)\}| = |F(\xi, \eta)|.$$

The *phase spectrum* [aDru10] of function f is a function $\Phi(\xi, \eta) : \mathbb{R}^2 \rightarrow \langle 0, 2\pi \rangle$ defined as

$$\begin{aligned} \Re F(\xi, \eta) &= A(\xi, \eta) \cos \Phi(\xi, \eta), \\ \Im F(\xi, \eta) &= A(\xi, \eta) \sin \Phi(\xi, \eta). \end{aligned}$$

If $A(\xi, \eta) = 0$ for some (ξ, η) , we define $\Phi(\xi, \eta) = 0$.

3.2 FOURIER TRANSFORM

The Fourier transform gives us a tool to transform convolution to multiplication and vice versa, which has useful applications in image processing.

Definition 3.11 (Convolution). Let functions $f_1(x, y), f_2(x, y)$ fulfill the assumptions of Definition 3.6. The *convolution* [cBJS88] $f_1 * f_2$ of functions f_1, f_2 is a function

$$f(x, y) = \iint_{\mathbb{R}^2} f_1(s, t) f_2(x - s, y - t) \, ds \, dt.$$

Theorem 3.12. Let functions $f_1(x, y), f_2(x, y)$ fulfill the assumptions of Definition 3.6. Let $F_1(\xi, \eta), F_2(\xi, \eta)$ be their Fourier spectra. Then

$$\begin{aligned} \mathcal{F}\{f_1(x, y) * f_2(x, y)\} &= F_1(\xi, \eta) \cdot F_2(\xi, \eta), \\ \mathcal{F}\{f_1(x, y) \cdot f_2(x, y)\} &= \frac{1}{4\pi^2} F_1(\xi, \eta) * F_2(\xi, \eta). \end{aligned}$$

For proofs see [aDru10]. Note that the left-hand sides of the equations in the theorem require that the functions that are transformed fulfill the conditions of Definition 3.6 of the Fourier transform. These properties of function multiplication and convolution are also proved in [aDru10].

3.2.2 Discrete Fourier transform

The two-dimensional discrete Fourier transform is most commonly defined for functions $f(x, y)$ defined on $\{0, 1, \dots, N_1 - 1\} \times \{0, 1, \dots, N_2 - 1\}$, where N_1, N_2 are natural numbers. This notation is used in [cBJS88] and [aDru10], for instance. Here we treat the simplified case when $N_1 = N_2 = N$.

There is also a different notation used in the theory of the discrete Fourier transform, e.g. in [cČiz81]. The objects that are used are finite sequences (in the case of the one-dimensional discrete Fourier transform), their elements are a_k . This approach might be confusing in the two dimensional case, it is necessary to use two indexes. Therefore, we stick here to functions $f(x, y)$ defined on a discrete domain.

Definition 3.13 (Discrete Fourier transform). Let $f(x, y)$ be a function $\{0, 1, \dots, N - 1\} \times \{0, 1, \dots, N - 1\} \rightarrow \mathbb{C}, N \in \mathbb{N}$. The *discrete Fourier transform* of function $f(x, y)$ is function $\mathcal{D}\{f\}(\xi, \eta) = F(\xi, \eta) : \{0, 1, \dots, N - 1\}^2 \rightarrow \mathbb{C}$ defined as

$$F(\xi, \eta) = \sum_{x=0}^{N-1} \sum_{y=0}^{N-1} f(x, y) e^{-\frac{2\pi i}{N}(x\xi + y\eta)}. \quad (3.2)$$

Function F is also called the *Fourier spectrum* of function f .

Definition 3.14 (Inverse discrete Fourier transform). Let $f(x, y)$ be a function $\{0, 1, \dots, N - 1\}^2 \rightarrow \mathbb{C}, N \in \mathbb{N}$ and let $F(\xi, \eta)$ be its discrete Fourier transform. The *inverse discrete Fourier transform* of function $F(\xi, \eta)$ is function $\mathcal{D}^{-1}\{F\}(x, y) : \{0, 1, \dots, N - 1\}^2 \rightarrow \mathbb{C}$ defined as

$$\mathcal{D}^{-1}\{F\}(x, y) = \frac{1}{N^2} \sum_{\xi=0}^{N-1} \sum_{\eta=0}^{N-1} F(\xi, \eta) e^{\frac{2\pi i}{N}(x\xi + y\eta)}. \quad (3.3)$$

Since all the sums in the formulae for the discrete Fourier transform and the inverse discrete Fourier transform are finite, there is a Fourier inversion theorem that says that the inverse discrete Fourier transform of the discrete Fourier transform of a function is the function itself. If the computations are preformed with a finite precision (single, double, extended), numerical errors was cause that these functions differ slightly. However, this is a general problem of numerical computations.

Theorem 3.15 (Fourier Inversion Theorem). Let $f(x, y)$ be a function $\{0, 1, \dots, N - 1\}^2 \rightarrow \mathbb{C}$, $N \in \mathbb{N}$ and let $F(\xi, \eta)$ be its discrete Fourier transform. Then the inverse discrete Fourier transform of function $F(\xi, \eta)$ is function $f(x, y)$, i.e.

$$\mathcal{D}^{-1} \{ \mathcal{D} \{ f(x, y) \} \} = f(x, y).$$

Proof. For proof see [aDru10]. □

When talking about digital images or signals, the notions *high frequencies*, *low frequencies* are commonly used. They refer to parts of the domain of the Fourier spectrum of a function. They are rather fuzzy-notions. When talking about functions defined on \mathbb{R}^2 , low frequencies lie in a neighborhood of the origin of the Fourier spectrum, whereas high frequencies lie further from the origin. In the case of the discrete Fourier transform, low frequencies correspond to regions that are close to the corners $([0, 0], [N - 1, 0], [0, N - 1], [N - 1, N - 1])$ of the spectrum, the high frequencies are in the center of the domain of the spectrum.

The definition of the amplitude and the phase spectrum of functions defined on $\{0, 1, \dots, N - 1\}^2$ is analogous to the definition for functions defined on \mathbb{R}^2 .

Definition 3.16 (Amplitude spectrum, phase spectrum). Let $f(x, y)$ be a function $\{0, 1, \dots, N - 1\}^2 \rightarrow \mathbb{C}$, $N \in \mathbb{N}$ with Fourier spectrum $F(\xi, \eta)$. The *amplitude spectrum* [cBJS88] of function f is function $A(\xi, \eta) : \{0, 1, \dots, N - 1\}^2 \rightarrow \mathbb{R}$ defined as

$$A(\xi, \eta) = | \mathcal{D} \{ f(x, y) \} | = | F(\xi, \eta) |.$$

The *phase spectrum* [cBJS88] of function f is function $\Phi(\xi, \eta) : \{0, 1, \dots, N - 1\}^2 \rightarrow \langle 0, 2\pi \rangle$ defined as

$$\begin{aligned} \Re F(\xi, \eta) &= A(\xi, \eta) \cos \Phi(\xi, \eta), \\ \Im F(\xi, \eta) &= A(\xi, \eta) \sin \Phi(\xi, \eta). \end{aligned}$$

If $A(\xi, \eta) = 0$ for some (ξ, η) , we define $\Phi(\xi, \eta) = 0$.

In the previous section, we discussed the connection of the convolution and the Fourier transform. Here we do the same with the discrete Fourier transform and the discrete periodic convolution. The periodic extension of a function defined on $\{0, 1, \dots, N - 1\}^2$ is necessary for this to be defined. Since Equation (3.2) can be evaluated for any $(\xi, \eta) \in \mathbb{Z}^2$, this allows us to define the periodic extension as follows:

Definition 3.17 (Periodic extension of function and its Fourier spectrum). Let $f(x, y)$ be a function $\{0, 1, \dots, N - 1\}^2 \rightarrow \mathbb{C}$, $N \in \mathbb{N}$ and let $F(\xi, \eta)$ be its Fourier spectrum.

3.2 FOURIER TRANSFORM

The *periodic extension of the Fourier spectrum* F [aDru10] is function $\tilde{F}(\xi, \eta) : \mathbb{Z}^2 \rightarrow \mathbb{C}$ defined as

$$\tilde{F}(\xi, \eta) = \sum_{x=0}^{N-1} \sum_{y=0}^{N-1} f(x, y) e^{-\frac{2\pi i}{N}(x\xi + y\eta)}.$$

The *periodic extension of function* f is function $\tilde{f}(x, y) : \mathbb{Z}^2 \rightarrow \mathbb{C}$ defined as

$$\tilde{f}(x, y) = \frac{1}{N^2} \sum_{\xi=0}^{N-1} \sum_{\eta=0}^{N-1} F(\xi, \eta) e^{\frac{2\pi i}{N}(x\xi + y\eta)}.$$

It is straightforward that the definition has the following consequences (for details see [aDru10]):

Corollary 3.18. Let $f(x, y)$ be a function $\{0, 1, \dots, N-1\}^2 \rightarrow \mathbb{C}, N \in \mathbb{N}$. Then for every $(x, y), (\xi, \eta) \in \{0, 1, \dots, N-1\}^2$ and $k, l \in \mathbb{Z}$ it holds:

$$f(x, y) = \tilde{f}(x + kN, y + lN),$$

$$F(\xi, \eta) = \tilde{F}(\xi + kN, \eta + lN).$$

In particular,

$$\tilde{f}(x, y) = f(x, y), \quad \tilde{f}(-x, -y) = f(N - x, N - y),$$

$$\tilde{F}(\xi, \eta) = F(\xi, \eta), \quad \tilde{F}(-\xi, -\eta) = F(N - \xi, N - \eta).$$

Definition 3.19 (Discrete Fourier transform of function's periodic extension). Let $f(x, y)$ be a function $\{0, 1, \dots, N-1\}^2 \rightarrow \mathbb{C}, N \in \mathbb{N}$. The discrete Fourier transform of the periodic extension of function f , $\tilde{f}(x, y) : \mathbb{Z}^2 \rightarrow \mathbb{C}$ is function $\mathcal{D}\{f\}(\xi, \eta) = F(\xi, \eta) : \{0, 1, \dots, N-1\}^2 \rightarrow \mathbb{C}$ defined as

$$F(\xi, \eta) = \sum_{x=0}^{N-1} \sum_{y=0}^{N-1} \tilde{f}(x, y) e^{-\frac{2\pi i}{N}(x\xi + y\eta)}.$$

Definition 3.20 (Inverse discrete Fourier transform of function's periodic extension). Let $f(x, y)$ be a function $\{0, 1, \dots, N-1\}^2 \rightarrow \mathbb{C}, N \in \mathbb{N}$ and let $F(\xi, \eta)$ be its discrete Fourier transform with periodic extension $\tilde{F}(\xi, \eta) : \mathbb{Z}^2 \rightarrow \mathbb{C}$. The inverse discrete Fourier transform of function $\tilde{F}(\xi, \eta)$ is function $\mathcal{D}^{-1}\{\tilde{F}\}(x, y) : \{0, 1, \dots, N-1\}^2 \rightarrow \mathbb{C}$ defined as

$$\mathcal{D}^{-1}\{\tilde{F}\}(x, y) = \frac{1}{N^2} \sum_{\xi=0}^{N-1} \sum_{\eta=0}^{N-1} \tilde{F}(\xi, \eta) e^{\frac{2\pi i}{N}(x\xi + y\eta)}.$$

Corollary 3.21. Let $f(x, y)$ be a function $\{0, 1, \dots, N-1\}^2 \rightarrow \mathbb{C}, N \in \mathbb{N}$ with Fourier spectrum $F(\xi, \eta)$. For every $(x, y) \in \{0, 1, \dots, N-1\}^2$, it holds:

$$\mathcal{D}\{f(x, y)\} = \mathcal{D}\{\tilde{f}(x, y)\},$$

$$\mathcal{D}^{-1}\{\mathcal{D}\{\tilde{f}(x, y)\}\} = \mathcal{D}^{-1}\{\tilde{F}(\xi, \eta)\} = f(x, y).$$

We can finally give the definition of the discrete periodic convolution and its connection with the discrete Fourier transform.

Definition 3.22 (Discrete periodic convolution). Let $f_1(x, y), f_2(x, y)$ be functions $\{0, 1, \dots, N-1\}^2 \rightarrow \mathbb{C}, N \in \mathbb{N}$. Function $f(x, y) : \{0, 1, \dots, N-1\}^2 \rightarrow \mathbb{C}$ is called the *discrete periodic convolution* [aDru10] of functions f_1, f_2 , denoted by $f(x, y) = f_1(x, y) * f_2(x, y)$, if

$$f(x, y) = \sum_{s=0}^{N-1} \sum_{t=0}^{N-1} f_1(s, t) \tilde{f}_2(x-s, y-t).$$

Theorem 3.23. Let functions $f_1(x, y), f_2(x, y) : \{0, 1, \dots, N-1\}^2 \rightarrow \mathbb{C}, N \in \mathbb{N}$ have Fourier spectra $F_1(\xi, \eta), F_2(\xi, \eta)$. Then [aDru10]

$$\begin{aligned} \mathcal{D}\{f_1(x, y) * f_2(x, y)\} &= F_1(\xi, \eta) \cdot F_2(\xi, \eta), \\ \mathcal{D}\{f_1(x, y) \cdot f_2(x, y)\} &= \frac{1}{N^2} F_1(\xi, \eta) * F_2(\xi, \eta). \end{aligned}$$

For proofs see [aDru10].

Remark 3.24. The approach with periodic extension used here is used e.g. in [cBJS88]. There is also another approach which uses modulo arithmetics used e.g. in [cČíž81].

Connection between the Fourier series and the discrete Fourier transform, sampling

The connection between the discrete Fourier transform and the Fourier series is described in [cBJS88]. Let f be a p -periodic function $\mathbb{R} \rightarrow \mathbb{R}$ and $\Phi_f(x)$ its Fourier series. The Fourier series in the exponential form is [cFol92]

$$\Phi_f(x) = \sum_{k=-\infty}^{\infty} c_k e^{2\pi i \frac{kx}{p}} = c_0 e^0 + \sum_{k=1}^{\infty} \left(c_k e^{2\pi i \frac{kx}{p}} + c_{-k} e^{-2\pi i \frac{kx}{p}} \right) = \quad (3.4)$$

$$\begin{aligned} &= c_0 + \sum_{k=1}^{\infty} \left(c_k \cos \frac{2\pi kx}{p} + c_k i \sin \frac{2\pi kx}{p} + c_{-k} \cos \frac{2\pi kx}{p} - c_{-k} i \sin \frac{2\pi kx}{p} \right) = \\ &= c_0 + \sum_{k=1}^{\infty} \left((c_k + c_{-k}) \cos \frac{2\pi kx}{p} + i(c_k - c_{-k}) \sin \frac{2\pi kx}{p} \right), \end{aligned} \quad (3.5)$$

where

$$c_k = \frac{1}{p} \int_0^p f(x) e^{-2\pi i \frac{kx}{p}} dx$$

are complex numbers. The Fourier series can also be written in the real form as [cFol92]

$$\Phi_f(x) = \frac{a_0}{2} + \sum_{k=1}^{\infty} \left(a_k \cos \frac{2\pi kx}{p} + b_k \sin \frac{2\pi kx}{p} \right), \quad (3.6)$$

3.2 FOURIER TRANSFORM

where a_k, b_k are real numbers. Comparing Equations (3.5) and (3.6), we obtain these connections between c_k and a_k, b_k :

$$\begin{aligned} c_0 &= \frac{a_0}{2} \\ c_k + c_{-k} &= a_k \\ i(c_k - c_{-k}) &= b_k. \end{aligned} \tag{3.7}$$

Let us now see what the fact that a_k, b_k are real means for c_k . Let us split the complex numbers c_k in its real and imaginary parts $c_k = \alpha_k + \beta_k i$. Plugging it in Equations (3.7), (3.8) and noting that the left-hand side of these equations is real

$$\begin{aligned} c_k + c_{-k} &= (\alpha_k + \alpha_{-k}) + i(\beta_k + \beta_{-k}) \text{ is real} \implies \beta_k = -\beta_{-k} \\ c_k - c_{-k} &= (\alpha_k - \alpha_{-k}) + i(\beta_k - \beta_{-k}) \text{ is imaginary} \implies \alpha_k = \alpha_{-k}. \end{aligned}$$

Hence $c_k = c_{-k}^*$.

Next, function f is sampled with equidistant sampling with N steps of length $\frac{p}{N}$ in each interval of length p . Let us denote

$$\overset{\square}{f}(n) = f\left(n\frac{p}{N}\right), \quad n \in \mathbb{Z}. \tag{3.9}$$

Plugging formally Equation (3.4) in Equation (3.9) in a point where Φ_f converges to f , we get

$$\overset{\square}{f}(n) = \sum_{k=-\infty}^{\infty} c_k e^{2\pi i \frac{k}{p} n \frac{p}{N}} = \sum_{k=-\infty}^{\infty} c_k e^{2\pi i \frac{kn}{N}}. \tag{3.10}$$

Function $e^{2\pi i \frac{kn}{N}}$ is periodic in variable k with period N , therefore we can separate k as $k = l + Nm$, where $m \in \mathbb{Z}, l \in \{0, 1, \dots, N-1\}$, and rewrite Equation (3.10) as

$$\overset{\square}{f}(n) = \sum_{m=-\infty}^{\infty} \sum_{l=0}^{N-1} c_{l+Nm} e^{\frac{2\pi i}{N} n(l+Nm)} = \sum_{m=-\infty}^{\infty} \sum_{l=0}^{N-1} c_{l+Nm} e^{2\pi i \frac{nl}{N}}.$$

Due to absolute convergence we can rearrange the series and swap the order of summation

$$\overset{\square}{f}(n) = \sum_{l=0}^{N-1} \sum_{m=-\infty}^{\infty} c_{l+Nm} e^{2\pi i \frac{nl}{N}}.$$

Denoting

$$\overset{\square}{F}(l) = \sum_{m=-\infty}^{\infty} c_{l+Nm},$$

we can write $\overset{\square}{f}(n)$ as

$$\overset{\square}{f}(n) = \sum_{l=0}^{N-1} \overset{\square}{F}(l) e^{2\pi i \frac{nl}{N}},$$

which is almost exactly the formula for the (one-dimensional) inverse discrete Fourier transform, just with the factor $\frac{1}{N}$ missing. Now, knowing the formula for the one-dimensional discrete Fourier transform, we can express $\overset{\square}{F}(l)$ from the last equation.

$$\overset{\square}{F}(l) = \frac{1}{N} \sum_{n=0}^{N-1} \overset{\square}{f}(n) e^{-2\pi i \frac{nl}{N}}$$

This yields the final connection between the Fourier series and the discrete Fourier transform as

$$N\bar{F}(l) = N \sum_{m=-\infty}^{\infty} c_{l+Nm} = \sum_{n=0}^{N-1} \bar{f}(n) e^{-\frac{2\pi i}{N}nl}. \quad (3.11)$$

There is something more to be discussed about Equation (3.11). If there is a subsequence of length N or less of the sequence of c_k , each $\bar{F}(l)$ equals to zero or to one particular c_k . This means that the original function f can be fully reconstructed from $\bar{F}(l)$ almost everywhere. These functions are called *band-limited*. If this is not true about the function, the so called aliasing effects may occur (more information with applications to image processing can be found in [cŽBF98]). It may help to increase N . If there are infinitely many non-zero elements of c_k , the original function can never be reconstructed from finitely many samples (without knowing additional information about function f - such as “it is a polynomial” or “it is an exponential”). For a band-limited function, the Fourier series and the discrete Fourier transform of a sampled function (with enough samples) are equivalent notions.

3.3 Image filters

Image filtering is broadly used in applications for reduction of noise in images, for sharpening, enhancing edges or other desired types of structures. These filters are based on various operations with the neighborhood of the processed pixel or they make use of unitary transforms [cPra01] that process the image as a whole. There are thousands of publications that deal with filters, but they do not define the notion of a filter (or to be precise, I have not succeeded finding a definition). In this section, I define a filter in a very broad way. Even a transformation that maps an arbitrary image to an image of a tiger of the same size is a filter according to this definition.

Definition 3.25 (Size-preserving image transformation). A *size-preserving image transformation* Φ is a mapping $\Phi : f \mapsto g$ that maps a gray-scale image to a gray-scale image with the same width and height (in the sense that the width of f is the same as the width of g , the same with their heights).

This notion includes all transformations that can be made with an image preserving its size – any local changes, local distortions of the image etc. It even includes creating a linear combination of two images (one of them fixed in the definition) or replacing an image with another image of the same size. It does not include transformations that change the size of the image such as enlarging and rotations by general angles.

Definition 3.26 (Pixel-value transformation, image filter). A size-preserving image transformation $\Phi : f \mapsto g$ is called a *pixel-value transformation* if Φ can be expressed for each pixel $[x, y] \in M$ as

$$g(x, y) = \phi(f(x, y)) = (\phi \circ f)(x, y).$$

An image transformation that is not a pixel-value transformation is called an *image filter*.

This means that for a pixel value transformation, only the pixel value $f(x, y)$ is necessary for the evaluation of the transformed image g in a pixel $[x, y]$. For the evaluation

3.3 IMAGE FILTERS

of the value of the filtered image g in a pixel $[x, y]$, we need the values of more pixels, usually values of f in a neighborhood of $[x, y]$. The function ϕ can be constructed in many different ways, it can contain information about the image like its histogram, but the most important thing is that there is only one function $\phi(t)$ for the whole image. It is a function of one variable – the pixel value in the input image. The information about the position of this pixel cannot be used.

A typical example of the pixel-value transformation is the *gamma-transformation*, which preserves the maximal and minimal pixel value while brightening or darkening the image. If we assume both the input and output values in $\langle 0, 1 \rangle$, the transformation is

$$\phi(t) = t^{\frac{1}{\gamma}},$$

where γ is a positive number. γ is inversed so that $\gamma > 1$ means brighter images, $\gamma < 1$ means darker images. The transformation is a power function, e.g. $\gamma = 2$ means the square root function. For constructing the function ϕ , it is necessary to know the maximal and minimal pixel value in the image.

3.3.1 Adaptive filters

An *adaptive filter* is a more complicated notion, which is commonly used, but I have never seen its definition. It is almost impossible to define an adaptive filter in a mathematically rigorous way. Therefore, the notion will be defined in this thesis only intuitively. Generally, an adaptive filter is an intelligent filter which changes the algorithm of image filtering locally based on the properties of the image. It makes no sense to search for a boundary of adaptive filters, to say which filter is adaptive and which is not.² Adaptive filters may respect the distribution and properties of structures in the image, the properties of noise in different parts of the image. They can be designed for processing images of specific types, such as images of the solar corona, images of the night sky (which contain stars that must not be interpreted as impulse noise), images of blood cells etc.

The filters for solar corona structure enhancement described in this thesis are adaptive filters. They were designed one-purpose for enhancing structures in images of the solar corona, are specific because of the big brightness gradient and the decrease of the contrast of the structures with distance from the Sun.

3.3.2 Linear filters

An image filter is linear if each pixel value in the filtered image g is an affine combination of values of pixels in a neighborhood of that pixel in the original image f . A more precise definition follows.

Definition 3.27 (Incomplete convolution). Let $f(x, y)$ be a gray-scale image with width w and height h . Let $C(i, j)$ be a function $C : \{-n, -n + 1, \dots, n - 1, n\} \times \{-n, -n + 1, \dots, n - 1, n\} \rightarrow \mathbb{R}$ for a natural n and let $w(x, y)$ be a function $w : \mathbb{Z}^2 \rightarrow \{0, 1\}$. Then

²It is a similar case as if we tried to search for the boundary of algebra or the boundary of variational methods of solving ODEs.

function

$$(f \circledast C)_w(x, y) = \frac{\sum_{i=-n}^n \sum_{j=-n}^n f((x-i) \bmod w, (y-j) \bmod h) C(i, j) w(x-i, y-j)}{\sum_{i=-n}^n \sum_{j=-n}^n C(i, j) w(x-i, y-j)}$$

is called the *partial convolution of function f with kernel C and weight function w* (adapted from [cDru09b].)

The weight function in the definition of the incomplete convolution is set to zero for pixels out of the domain of the image if incomplete convolution is used for standard image filtering. Furthermore, it can be set to zero in pixels which are defective or pixels that belong to a part of the image that is supposed not to be taken into consideration for the filtration (e.g. the pixel belongs to a completely different part of the image from pixel $[x, y]$).

For most adaptive filters, we also need to define the incomplete convolution with variable kernel, where the kernel is not a function of only two variables describing the position in the kernel, but also two other variables describing the position of the processed pixel in the image. The kernel may vary for different pixels in the image.

Definition 3.28 (Incomplete convolution with variable kernel). Let $f(x, y)$ be a gray-scale image with width w and height h . Let $C(i, j, x, y)$ be a function $C : \{-n, -n+1, \dots, n-1, n\} \times \{-n, -n+1, \dots, n-1, n\} \times M \rightarrow \mathbb{R}$ for a natural n and let $w(x, y)$ be a function $w : \mathbb{Z}^2 \rightarrow \{0, 1\}$. Then function

$$(f \circledast C)_w(x, y) = \frac{\sum_{i=-n}^n \sum_{j=-n}^n f((x-i) \bmod w, (y-j) \bmod h) C(i, j, x, y) w(x-i, y-j)}{\sum_{i=-n}^n \sum_{j=-n}^n C(i, j, x, y) w(x-i, y-j)}$$

is called the *partial convolution of function f with variable kernel C and weight function w* .

Definition 3.27 is a special case of Definition 3.28.

Definition 3.29 (Linear filter). An image filter is called *linear* if it is an incomplete convolution with a (possibly) variable kernel of an image. A linear filter is called *non-adaptive* if its kernel is constant for the whole image (i.e. Def. 3.27) and the weight function $w(x-i, y-j)$ is equal to 1 if the pixel to be used $[x-i, y-j]$ belongs to the image ($[x-i, y-j] \in M$) and 0 if the pixel is out of the domain of the image ($[x-i, y-j] \notin M$). A linear filter is called *adaptive* if its kernel is not constant for the whole image or the weight function is equal to zero for some pixels of the image.

The definition of a linear adaptive filter is in compliance with the description of an adaptive filter in Section 3.3.1. Assuming an image with cells on a background, a filter that blurs the background, omitting from the calculation all pixels that belong to the cells, is an adaptive filter. It requires information about the position of the cells. Such a filter has a constant convolution kernel $C(i, j)$ and a weight function w which is equal to zero for pixels that belong to cells. The tangential filter and the ACHF (Sections 5.1 and 5.2) for solar corona structure enhancement are also adaptive linear filters. They have w set to zero inside the Moon in the image and most often also a variable kernel. The rest of the filters in this thesis are non-linear.

The connection between a linear filter and the Fourier transform

Let us now suppose that the image to be filtered is a square and the weight function is equal to 1 everywhere. Then the notion of an incomplete convolution is identical with a specific case of the discrete periodic convolution (Def. 3.22), where $f_2 = f$,

$$\tilde{f}_1(x, y) = \begin{cases} C(x, y) & \text{for } [x, y] \in \{-n, -n+1, \dots, n-1, n\}^2 \\ 0 & \text{otherwise} \end{cases}$$

and

$$\sum_{x=0}^{N-1} \sum_{y=0}^{N-1} \tilde{f}_1(x, y) = 1. \quad (3.12)$$

With this denotation, the filtered image $g = f_1 * f$. According to Theorem 3.23, the Fourier spectrum $G(\xi, \eta) = \mathcal{D}\{g(x, y)\}$ of the filtered image g can be expressed as a product of the Fourier spectrum of the original image f and the Fourier spectrum of the kernel f_1 ,

$$G(\xi, \eta) = \mathcal{D}\{g(x, y)\} = \mathcal{D}\{(f_1 * f)(x, y)\} = \mathcal{D}\{f_1\} \cdot \mathcal{D}\{f\} = F_1(\xi, \eta) \cdot F(\xi, \eta).$$

This gives us a tool for computing a convolution. Since there are really fast algorithms for the discrete Fourier transform, it may be faster to compute the filtered image is

$$g = \mathcal{D}^{-1}\{\mathcal{D}\{g\}\} = \mathcal{D}^{-1}\{F_1(\xi, \eta) * F(\xi, \eta)\},$$

especially for larger kernels.

Some filters do not involve normalization in the sense of Equation (3.12). They can change significantly the range of pixel values in the image. They usually work with floating-point data formats and the author of the algorithm does not have to care about the range of the pixel values. The pixel values are only transformed to $\{0, 1, 2, \dots, 255\}$ for displaying the image on a screen or saving the results in a standard file format.

Unsharp masking

A commonly used method for applying high-pass filters on images is computing a so called (*unsharp*) *mask*, which is subtracted from the original image to obtain the filtered image. The mask is the core of the filter. The idea is derived below.

A high-pass filter is a filter that enhances information on higher spatial frequencies and reduces information on lower spatial frequencies. High-pass filters are used e.g. for sharpening images. A high-pass filter can be described with convolution as (adapted from [cDru13])

$$g = f_1 * f = k \cdot [(d(x, y) - l(x, y)) * f] + q = k \cdot (d * f - l * f) + q = k \cdot (f - m) + q, \quad (3.13)$$

where k and q are suitable constants that ensure that f_1 is normalized to 1 in the sense of Equation (3.12). We do not care about the image edges here, so we approximated an incomplete convolution with a discrete periodic convolution. Function $d(x, y)$ is the *discrete impulse function* [cČiž81, aDru10], a function that plays the analogous role for the

discrete Fourier transform as the Dirac distribution for the Fourier transform of functions defined on \mathbb{R}^2 . It is a function defined on $\{0, 1, \dots, N - 1\}^2$ as

$$d(x, y) = \begin{cases} 1 & \text{if } (x, y) = (0, 0) \\ 0 & \text{else.} \end{cases}$$

Applying the discrete periodic convolution with the discrete impulse function on function f does not change the function, $d * f = f * d = f$. The digital image $m(x, y)$ in Equation (3.13) is called the (*unsharp*) *mask*.

We can also read only the first and the last terms in Equation (3.13) skipping the steps that involve convolution. It would mean that the filter is applied by subtracting a mask from the original image (and applying a linear pixel-value transformation). The important step is creating the unsharp mask. There are many sophisticated filters that are not linear in the sense of Definition 3.29, but they involve unsharp masking. Several filters for enhancing structures in images of the solar corona are presented in this work. Most of them are based on unsharp masking, the difference between them is in the way the mask is computed.

Chapter 4

Image acquisition and processing

This chapter is devoted to the process that the images of solar corona undergo from their acquisition to structure enhancement. The process consists of many steps. We are going to discuss how the steps are done, and if possible, also the mathematical reasons and principles of these steps. The largest part of the chapter deals with processing of images taken in white light during total solar eclipses. That is what we started with in 1999 and what we have developed special a set of one-purpose programs for. The process for this kind of images will be described first in Section 4.1 and after that, the following sections give an overview of the methods used for other kinds of images such as images in spectral lines taken during total solar eclipses or images from cosmic probes.

4.1 White-light images acquired during total solar eclipses

By white-light images we will mean images in the whole visible part of the spectrum, not only specific spectral lines in the visible part of the spectrum. These images are nowadays taken with regular digital single-lens reflex (DSLR) cameras or with scientific cameras producing gray-scale images in a broad part of the (visible or near-visible) spectrum. Earlier they were taken with classical cameras and negative or positive films.

4.1.1 Image acquisition

In this section we are going to discuss the image acquisition of white-light images during total solar eclipses. This is the most critical step of the whole process, since there is hardly a way to take back any mistakes that one may have done. A total solar eclipse lasts only a few minutes at one observing site and all the equipment has to be prepared, rehearsals should be done to minimize the risks of human error. Bad focusing of the lenses and incorrect timing the image acquisitions are the most common mistakes. But there are many aspects that have to be decided ahead – what camera to use, what lens, what exposure times to take, how to control the camera. Some recommendations can be found in [dEsA08, bDrD09].

Camera

The first question is if to use a digital or a classical camera. Glass plates (see [dDru07], for instance) and later negative films were used for total eclipse observations till 2000s. From about 2005, DSLR cameras have played a dominant role. Compared to digital photography, negative films have higher dynamic range, which means that a smaller range of exposure times is sufficient to capture the whole brightness range of the corona with a selected lens (see http://www.zam.fme.vutbr.cz/~druck/eclipse/Ecl1991m1/Tse1991rdd_c1/0-info.htm). The nowadays used digital cameras have many advantages compared to the classical ones. The images are directly saved as files, the step of scanning and the scanned images retouching is not present. They have higher resolution than regular 36×24 mm film frames and low noise and the cameras can be controlled by computers, which enables us to use several cameras at one observing site operated by one or two people. What is very important for image processing and analysis, the sensors in digital cameras have linear response to the intensity of the incident light, whereas classical frames have non-linear response to incident light.

Generally, any DSLR camera which can save images in a completely raw format, is suitable for TSE observation. Professional cameras are faster in saving files on memory cards, have higher resolution and lower noise. Even amateur cameras like Canon EOS 350D or 450D give high-quality images and their price is their undeniable advantage, which makes it possible to observe with several cameras at reasonable a cost (see e.g. the pictures in <http://www.zam.fme.vutbr.cz/~druck/eclipse/Ecl2008m/Expedition/0-info.htm>). Another option might be cooled scientific cameras, but their downloading time is usually much longer, which makes them unsuitable for observations of phenomena as short as total solar eclipses. Nowadays, Nikon cameras have better signal : noise ratio and higher dynamic range than Canon cameras.

Dust on the chip can be a serious problem. It is necessary to minimize its amount by cleaning the chip before the observation. There are special wipes or sticks that can be used for removing the most prominent dust particles. However, it is advised to have the camera body cleaned in a special service.¹ Newer models of DSLR cameras have a sensor cleaning tool, which usually means that the camera vibrates the chip to remove the dust from the chip. The dust is then collected on a sticky surface. Most often, cameras run this vibration when they are turned on. This feature can remove most of the dust particles from the chip. A problem is that some of the particles are not removed with the vibration and they move on the chip as the chip vibrates. To remove dark spots in images caused by dust particles, it is necessary that they are at the same position in all images including the calibration images (flat-fields). Therefore, the sensor cleaning function can be used before the eclipse to remove as many dust particles as possible. Then it must be disabled until all images in the observing series including the calibration images are taken.

The camera and the lens have to be attached to a parallactic mount (in the case of shorter focal lengths such as 200 mm a tripod is sufficient) that is robust enough to hold the system even during the longest exposure times required for this system.

¹A service in Brno both for Nikon and Canon: <http://www.afoto.cz/>, in Prague for Canon: <http://www.awh.cz/>, in Bratislava for Canon: <http://www.prolaika.sk/clanky/servis-2/>.

Lens – focal length

Fred Espenak and Jay Anderson in their eclipse bulletin [dEsA08] show the relation between the diameter d of the solar disk on the camera sensor or a film frame and the focal length f of the used lens as

$$d \doteq \frac{f}{109}.$$

The relation is only approximate, because the distance of the Earth from the Sun varies during the year. The formula implies that with a 1 000 mm lens the image of the Sun on the chip will be about 9.2 mm, with a 200 mm lens about 1.8 mm. Note that the size of a frame of a classical film or the chip of the full-frame camera is 36×24 mm. The choice of the lens depends on the quality of the parallactic mount that holds the cameras with lenses. The best solution is to cover the extent of the corona by several lenses such as 200, 500, 1 000 and 1 600 mm. Amateur and semi-professional cameras have smaller chips, in the case of Canon cameras they are about 1.6 times smaller (22.2×14.8 mm for Canon EOS 450D [dDpr08]) in the case of Nikon cameras they are 1.5 times smaller. This means that the same lens has a narrower field of view and the choice of lenses has to be changed accordingly.

The topic of a particular lens selection (reflector / refractor, brand, f-number) is beyond this work.

Exposure sequence

The extreme contrast in the corona demands the use of many different exposure times during the time of totality. Table 4.2 in the TSE 2010 bulletin [dEsA08] summarizes the relation between the used ISO, the lens' f-number, the exposure time and what part of the corona is correctly exposed in the image. Figure 4.1 gives us an idea of a set of images that are necessary to be taken to record the full extent of the corona for this field of view. Digital enhancement of coronal structures means strong enhancement of information on high spacial frequencies including noise. Therefore it is necessary to take not only a large variety of images with different exposure times, but also to take as many images as possible to eliminate the noise in the final image. The contrast of structures in the corona decreases with height, that is why it is better to take more images with longer exposure times than those with shorter exposure times. An example of suitable sequences can be found in [bDrD09]. A correct sequence contains images of all exposure times (separated by one stop or less) starting with an image with correctly exposed prominences and ending with an image where a large part of the corona is overexposed, but the overexposed part does not touch the edges of the image.

Camera control

During the eclipse, cameras should be controlled either manually with a cable release or by a computer. (Pressing the shutter release manually would shake the camera shortly before the exposure, which makes this option unusable.) Most programs control each camera with a single USB cable. In this case the camera cannot use its cache and there must be some time left between taking individual frames to let the camera save the image to a memory card. Thus an advantage of taking images manually is the possibility to obtain

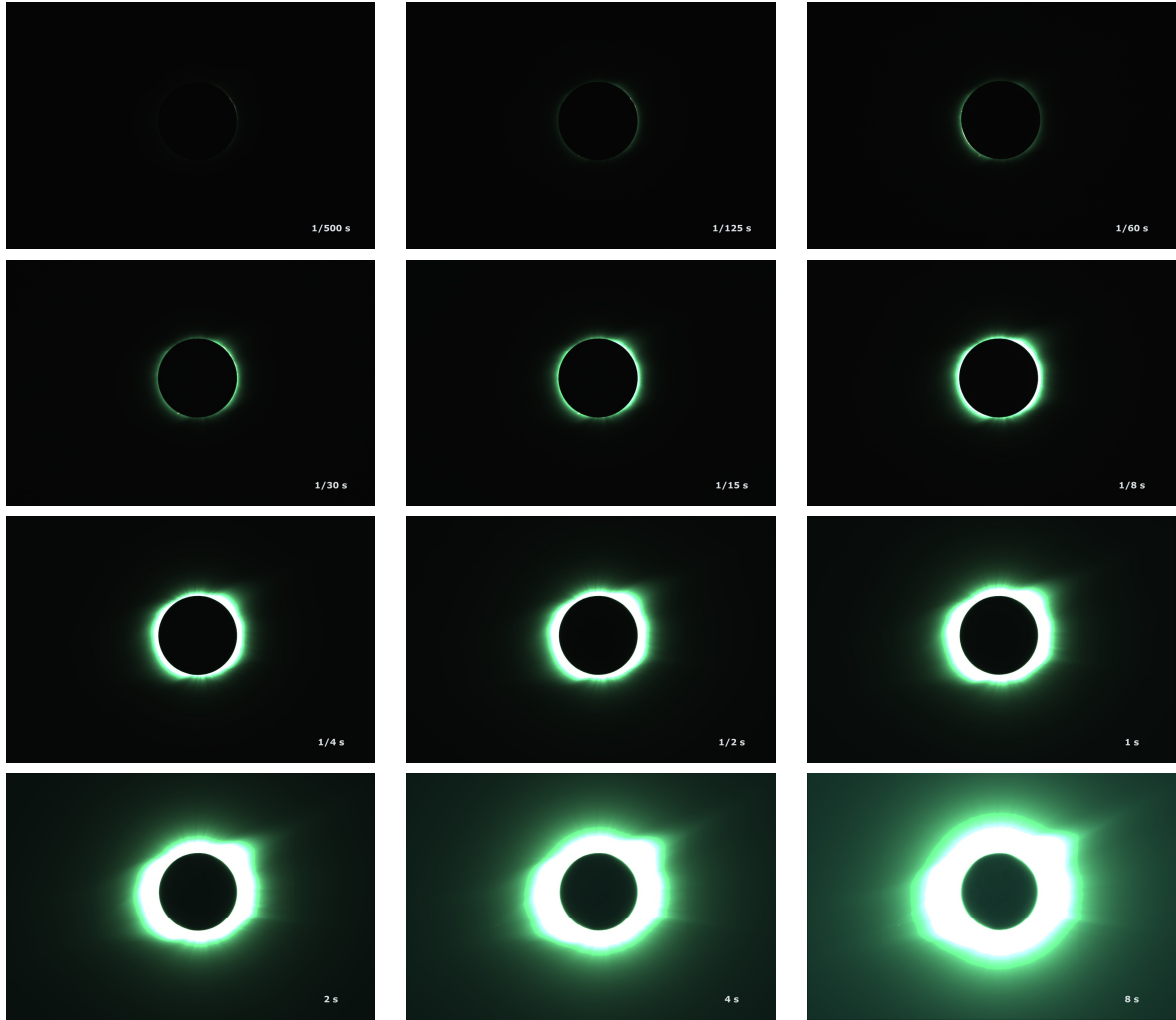


Figure 4.1: A sequence of images with various exposure times taken during the 2008 TSE. Lens Maksutov-Cassegrain 3M-6A, 6.3/500 mm, digital camera Canon EOS 350D, ISO 100. Images are completely raw, linear, before normalization by sensitivity of color sensors.

more images, but every camera has to have its own mount (because the person operating the camera shakes the mount when setting exposure times on the camera body).

A simple application for Linux that can control up to six Canon cameras of the older type (EOS 350D, 20D, 5D, 300D), is Multican created by Jindřich Nový [dNov07]. Its input passed as parameters are files of the format `CameraX_YYYYYYYYYY`, where X is the number assigned to a camera connected to a computer in sequential numbering and YYYYYYYYYY is the serial number of the camera. This number is written on the camera bottom or can be read by calling Multican with no parameter. An example showing a part of a script file² with a correct structure is:

```
# Camera 1
# Canon EOS 350D
# Ser. Num: 1330441536
```

²There is also a generator of these scripts available upon request that generates suitable scripts based on the camera type, lens focal length and f-number and the duration of the eclipse.

4.1 WHITE-LIGHT IMAGES ACQUIRED DURING TOTAL SOLAR ECLIPSES

```
# Pentacon, 2.8/135mm
#
00:00:55.990 tv=4000
00:00:56.090 iso=100
00:00:56.190 shot
00:01:00.000 shot
00:01:03.810 shot
00:01:07.519 tv=2000
00:01:07.619 shot
...
00:27:51.666 nop
```

Lines starting with a hash are comments that are skipped by Multican. Time in hours, minutes, seconds and milliseconds counted from the time when the Enter key was pressed are followed with commands that are performed at these times – setting exposure times, setting the ISO and taking images. The sequence must end with `nop` command.

When Multican is called with script files as parameters

```
multican Camera1_1330441536 Camera2_5675931124,
```

it loads the scripts, checks if these cameras are present and waits to start the sequence until the Enter key is pressed. The times between `shot` commands must include the exposure time and the saving time. If the camera receives a command earlier, the communication with this camera and possibly with the other cameras fails, so this parameter must be tested ahead.

The advantage of Multican is precise timing of the exposures and the possibility to generate script files by any tools in a simple way. Some users may consider it a disadvantage that it does not have a GUI. Other software tools that can control digital cameras are the Eclipse Orchestrator for Windows (<http://www.moonglowtech.com/products/EclipseOrchestrator/>) with Free and Pro, version that can also use the serial port to control the shutter thus enabling the camera to use the cache, and Solar Eclipse Maestro for MacOS X (http://xjubier.free.fr/en/site_pages/solar_eclipses/Solar_Eclipse_Maestro_Photography_Software.html) that is a sophisticated tool for observing solar eclipses.

4.1.2 Image calibration

The theory for this topic is covered by [dCor04]. The following text is based on this source.

Ideally, an image taken by a CCD (or CMOS) camera would give accurate information about the light flux distribution over the observed scene. Unfortunately, this is generally not the case. Instrument properties, imperfections and the discrete nature of light itself introduce errors in the measured data. The errors (differences between the measured values and the ‘true’ ones) are the result of several factors, some random in nature, and some deterministic.

The goal of the image calibration is to minimize the contribution of deterministic factors in the errors, in other words to remove the instrument signature from the data. In this section, we describe the way the general image calibration process works (also called *image reduction*), and in the process we define bias, dark and flat images.

The whole process is described for gray-scale images, even though standard color DSLR cameras are commonly used for eclipse observations. However, a vast majority of DSLR cameras gives gray-scale images. In every pixel they have only one measurement – of the red, green, or blue part of the observed scene. A color image is then made from this gray-scale image by interpolating the information about each color component. The process of calibration has to be done with the raw gray-scale image. There is a paragraph about conversion of raw images to color images (if sensors take measurements in different parts of the spectrum) at the end of this section.

CCD camera response model

Raw pixel values for a CCD frame can be expressed as follows:

$$s(x, y) = B(x, y) + tD(x, y) + tG(x, y)I(x, y) + R(x, y), \quad (4.1)$$

where $B(x, y)$ is the bias value of each pixel, t is the integration (exposure) time, $D(x, y)$ is the dark current, $G(x, y)$ is the sensitivity, $I(x, y)$ is the light flux reaching the pixel, and $R(x, y)$ is a random component – noise. The bias value is a preset value that is set to the sensors before the shutter is opened. It ensures that even with negative data values caused by noise no underflow occurs. The value varies slightly pixel-to-pixel. It is approximately 128 for Canon EOS 5D, 256 for Canon EOS 350D and 1024 Canon EOS 5D Mark II as an example. The dark current depends on the camera, but for each camera it depends on temperature. The higher temperature, the higher dark current. That is one of the reasons why some scientific cameras are cooled. $G(x, y)$ describes not only the sensitivity of each sensor on the chip, but also the vignetting effects³ of the optical system and the effects of dust particles on the chip. When taking a photograph, we are interested in the values of $I(x, y)$ or $tI(x, y)$. $R(x, y)$ will be used in a similar way as a generic constant in ODEs, even after division by or adding a constant or another function, it remains $R(x, y)$.

To estimate the flux values entering the optical system, we need to estimate B , D and G . After that, Equation (4.1) can be solved for I . B , D and G are calculated starting from calibration frames taken under controlled conditions: bias, dark and flat frames.

Bias frames

If we take very short exposures without opening the camera shutter – t can be considered as 0 and $I(x, y) = 0$ – so called *bias frames*, Equation (4.1) becomes

$$b(x, y) := s(x, y) = B(x, y) + R(x, y).$$

Since the noise $R(x, y)$ is random, we use b as an estimate of B ,

$$\tilde{B}(x, y) := b(x, y).$$

³Vignetting is a centrally symmetric darkening of the image with distance from the axis of the optical system caused by its optical properties. It is almost negligible with some lenses, especially if they are set to higher aperture numbers, but with most lenses it should be taken into consideration. Therefore, the Sun should be centered in the field of view so that the center of the vignetting is also the center for the radial direction in the corona.

4.1 WHITE-LIGHT IMAGES ACQUIRED DURING TOTAL SOLAR ECLIPSES

In the whole section about image calibration (Section 4.1.2), we use the tilde to denote the estimate. If we average more bias frames together, we can get arbitrarily close to B (its standard deviation decreases with a square root of the number of the images due to Chebyshev's inequality [cWil01]). Therefore a better estimate than the last equation is

$$\tilde{B}(x, y) := \frac{1}{N} \sum_{i=0}^{N-1} b_i(x, y).$$

We will call this the *master bias frame*.

Dark frames

If we now take longer exposures with (with exposure time t_0) with the shutter closed, we obtain *dark frames*

$$d(x, y) := B(x, y) + t_0 D(x, y) + R(x, y).$$

From this, we can subtract the estimation of bias and divide by the exposure time, and we get our dark current estimate,

$$\tilde{D}(x, y) := \frac{d(x, y) - \tilde{B}(x, y)}{t_0}.$$

Of course, to reduce the noise contribution we can also average several dark frames and estimate the dark current as

$$\tilde{D}(x, y) = \frac{1}{t_0} \frac{1}{M} \sum_{i=0}^{M-1} d_i(x, y) - \tilde{B}(x, y).$$

It is convenient to work with a different form of the dark current frame,

$$\tilde{D}'(x, y) = t_0 \tilde{D}(x, y) = \frac{1}{M} \sum_{i=0}^{M-1} d_i(x, y) - \tilde{B}(x, y).$$

which is called the *bias subtracted master dark frame*.

If we have a data frame (image of the observed scene) with an integration time of t_1 , the first two terms in Equation (4.1) are estimated by the *master dark frame* \tilde{D}_M

$$\tilde{D}_M(x, y) = \tilde{B}(x, y) + t_1 \tilde{D}(x, y) = \tilde{B}(x, y) + \frac{t_1}{t_0} \tilde{D}'(x, y). \quad (4.2)$$

If the integration (exposure) time of the data frame and the dark frames is the same, $t_1 = t_0$, the master dark frame can be simply computed as an average of dark frames,

$$\tilde{D}_M(x, y) = \frac{1}{M} \sum_{i=0}^{M-1} d_i(x, y). \quad (4.3)$$

The function $B(x, y)$ is specific for each camera and it does not change much with time or temperature. On the contrary, the function $D(x, y)$ depends strongly on temperature and ISO. Dark-frame images for an image set have to be taken shortly before or after this image set at the same conditions (not transporting the camera to another place if possible).

Flat-field frames

With B and D out of the way, we need a way to estimate G in Equation (4.1) before we can recover the incident flux. To do this, we apply a flat-field (even) illumination to the camera and acquire several flat-field frames

$$f(x, y) := s(x) = B(x, y) + t_f D(x, y) + t_f G(x, y) L + R(x, y), \quad (4.4)$$

where L is the light flux reaching each pixel, assumed equal across the frame. Images of the blue sky acquired with the lens covered with flimsy paper can be considered as flat-field frames for white-light images taken with telephoto lenses. For wider-angle lenses, special panels emitting light evenly have to be used. Flat-field images for a collection of images have to have the same ISO, aperture value and focusing as the images in the collection. The camera also should not be moved (and also not switched off and on in the case of newer cameras with automatic sensor cleaning) between taking the data frames and the flat-field images so that dust particles on the chip do not move. The exposure should be selected so that none of the pixels in the flat-field frames is close to saturation, the best possibility is the image histogram centered in the range of possible values. Aperture priority mode can often be used for taking flat-field frames.

We then calculate a master dark frame for the flat fields $D_M^F(x, y)$ and subtract it from the flats, obtaining

$$f'(x, y) = f(x, y) - D_M^F(x, y) = t_f G(x, y) L + R(x, y).$$

The master dark frame for flat fields $D_M^F(x, y)$ can either be computed by Equation (4.2) or there are dark frames available with the same exposure time as the flat-fields, then we can use an average of them, Equation (4.3). Again, to reduce the noise contribution, we usually average several flat frames, to arrive at a *master flat frame*

$$\tilde{F}_M(x, y) = \frac{1}{K} \sum_{i=0}^{K-1} f'_i(x, y) = \frac{1}{K} \sum_{i=0}^{K-1} f(x, y) - D_M^F(x, y) \quad (4.5)$$

If we knew L , we could solve the Equation (4.4) for $G(x, y)$. However, the absolute value of L is not known and varies between different sets of images. So, instead of calibrating the absolute value of $G(x, y)$, we only try to remove its variation across the frame. We introduce \bar{G} as the average of G over the whole image

$$G(x, y) = \bar{G} g(x, y),$$

where the average of $g(x, y)$ across the frame is 1. The variability of G across one image is caused by different sensitivity of sensors, by dust particles on the chip and by optics vignetting. Then the estimate of f' is

$$\tilde{F}'_M(x, y) = t_f \bar{G} g(x, y) L + R(x, y). \quad (4.6)$$

By taking the average of $\tilde{F}'_M(x, y)$ across the frame

$$\begin{aligned} \bar{F} &= \sum_{x=0}^{w-1} \sum_{y=0}^{h-1} t_f \bar{G} g(x, y) L + \bar{R} = \\ &= t_f \bar{G} L \sum_{x=0}^{w-1} \sum_{y=0}^{h-1} g(x, y) + \bar{R} \\ &= t_f \bar{G} L + \bar{R} \end{aligned}$$

4.1 WHITE-LIGHT IMAGES ACQUIRED DURING TOTAL SOLAR ECLIPSES

(where \bar{R} is the average of $R(x, y)$ over the image) and then dividing equation by \bar{F} , we obtain the estimation of $g(x, y)$

$$\frac{\tilde{F}_M(x, y)}{\bar{F}} = \tilde{g}(x, y), \quad (4.7)$$

which is the final result we can learn from flat-fields.

The above process assumes a camera where all pixels are equivalent, they all make measurement in the same part of the spectrum. However, this is not the case of common DSLR cameras with Bayer matrix, where half of the sensors measure the intensity of incident flux in the green part of the spectrum, a fourth in the red part of the spectrum and a fourth in the blue part of the spectrum. The sensors are identical, but there are color filters that select only a part of the spectrum for each sensor. A typical organization of the Bayer matrix (as patented by Bryce Bayer in 1976) can be found in Figure 4.2.

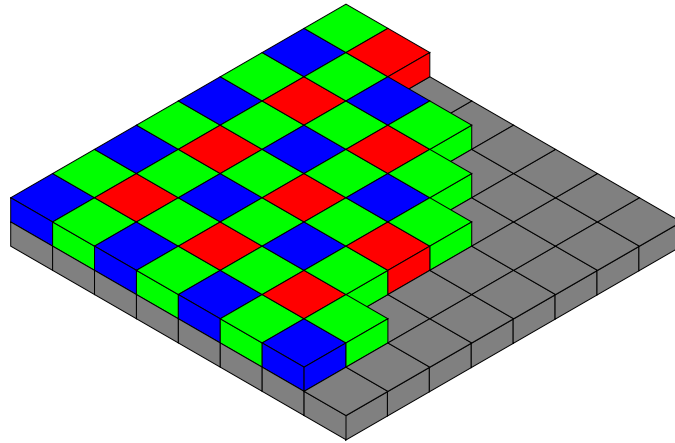


Figure 4.2: A schematic illustration of the Bayer matrix on the chip of a DSLR camera. Image downloaded from [dCbu06].

The pixel values of the flat-fields measured by red sensors (sensors with filters which select the red part of the spectrum) will differ from those measured by green sensors and from those measured by blue sensors due to different transmissivity of the filters, different sensitivity of the sensors in different parts of the spectrum and of course different spectral characteristics of the light source used for the flat-fields. Calibrating the images, we need to compensate for these differences. Let $\bar{V}_R, \bar{V}_G, \bar{V}_B$ be the average values of all red, green, and blue pixels, respectively, and let \bar{V} be the average pixel value in the whole image. We renormalize the master flat frame from Equation (4.5) by computing

$$\tilde{F}_M^N(x, y) = \begin{cases} \frac{\tilde{F}_M(x, y)}{\bar{V}_R} \bar{V} & \text{if pixel } [x, y] \text{ is red} \\ \frac{\tilde{F}_M(x, y)}{\bar{V}_G} \bar{V} & \text{if pixel } [x, y] \text{ is green} \\ \frac{\tilde{F}_M(x, y)}{\bar{V}_B} \bar{V} & \text{if pixel } [x, y] \text{ is blue.} \end{cases}$$

The renormalized master flat frame is then used instead of the master flat frame in Equations (4.6) and (4.7). This process is invariant to the spectral properties of the light source used for calibration, it is only required that all three color components are strong enough, otherwise the calibration process would bring too much noise in the image.

Reducing the data frames

Having the master dark and master flat frames, we can proceed to reduce the data frames. Starting from

$$s(x, y) = B(x, y) + t_1 D(x, y) + t_1 \bar{G} g(x, y) I(x, y) + R(x, y),$$

we subtract the master dark frame (Equation (4.2)) and divide by the normalized master flat (Equation (4.7)) to obtain

$$\frac{\bar{F}}{\tilde{F}_M(x, y)} \left(s(x, y) - \tilde{D}_M(x, y) \right) = t_1 \bar{G} I(x, y) + R(x, y) \quad (4.8)$$

$$\tilde{I}(x, y) = \frac{1}{\bar{G} \cdot t_1} \frac{\bar{F}}{\tilde{F}_M(x, y)} \left(s(x, y) - \tilde{D}_M(x, y) \right) \quad (4.9)$$

We have obtained an estimate of the incident light flux up to a multiplicative constant ($\bar{G}t_1$) which represents the average sensitivity of the camera multiplied by the integration time, which is the best we can do without a reference source calibrated in absolute units.

In some applications, we want to preserve the information of t_1 in the images, i.e. keep them brighter if they were exposed longer. Then Equation (4.8) is the result of image calibration.

Frame combining methods

Earlier in this section we used the term to ‘average’ several frames (bias and dark frames, flat-field frames) in order to reduce the noise. It was used as a general term meaning to compute a quantity that approximates the desired value. The commonly used methods follow.

Arithmetic average (mean) is the best in noise reduction and is computationally the fastest, but is strongly affected by outliers, i.e. impulse noise present especially in longer exposures caused by hot pixels or when high-energy cosmic particles hit the chip. Another property of the arithmetic average is that the results are not discrete in the sense that the result is not necessarily one of the original image values, it may be ‘something in between’.

Median takes more time to compute than the arithmetic average, but there are fast methods of median computation available (a simple method based on histogram is implemented in the FNRGF software for estimation of the standard deviation of the additive noise in the image). Median is very little influenced by outliers, but it is less efficient in removing noise. Also, when combining integer values, the median does nothing to smooth out the quantization effects. The following methods are a combination of both median and arithmetic average to make use of the advantages of both of them.

Mean-median is a variant of the median method intended to improve the statistical efficiency of the median, and get around the quantization problem. In the mean-median method, we compute the standard deviation of the pixel values around the median, and discard all the values that are farther away than a specified number of

4.1 WHITE-LIGHT IMAGES ACQUIRED DURING TOTAL SOLAR ECLIPSES

standard deviations (usually 1.5 or 2). The remaining values are averaged together. Denoting $I_0 = \{0, 1, \dots, N-1\}$, where N is the number of images to be combined, the algorithm for combining images f_0, \dots, f_{N-1} can be written as follows:

$$e_0(x, y) = \text{median}_{i \in I_0} f_i(x, y) \quad (4.10)$$

$$s_0(x, y) = \sqrt{\frac{1}{N-1} \sum_{i=0}^{N-1} (f_i(x, y) - e_0(x, y))^2} \quad (4.11)$$

$$I_1(x, y) = \{i \in I_0, |f_i(x, y) - e_0(x, y)| \leq \kappa s_0\}$$

$$e_1(x, y) = \frac{1}{|I_1|} \sum_{i \in I_1} f_i(x, y),$$

where κ is a constant (usually 1.5 or 2, as mentioned above). e_1 is the result. Mean-median is fast, and works well for large sets.

$\kappa\sigma$ -clipping is an elaborate method that gives good results even with small sets of images.

It starts by calculating the median and the standard deviation around it. The values with large deviations relative to the standard deviation are excluded. Then, the mean and standard deviation of the remaining values are computed. Again, the values that are farther away for the mean are excluded, and the process is repeated until there is no change in the mean or the iteration limit is reached. With the denotation of Equation (4.10), each iteration step of the $\kappa\sigma$ -clipping for $k = 1, 2, \dots$ is

$$s_{k-1}(x, y) = \sqrt{\frac{1}{|I_{k-1}|} \sum_{i \in I_{k-1}} (f_i(x, y) - e_{k-1}(x, y))^2}$$

$$I_k(x, y) = \{i \in I_{k-1}, |f_i(x, y) - e_{k-1}(x, y)| \leq \kappa s_{k-1}\}$$

$$e_k(x, y) = \frac{1}{|I_k|} \sum_{i \in I_k} f_i(x, y).$$

Transformation of a raw image to a color image

As it was mentioned above, a raw image from a DSLR camera is a gray-scale image where half of the pixels describe the green part of the incident flux, a fourth of the pixels do the red part, and a fourth of the pixels do the blue part. They are organized in the Bayer matrix, see Figure 4.2. The next step of the processing, image registration treated in Section 4.1.3, applies geometrical transformations like shift by a non-integer vector. A raw image where different pixels describe different colors would be unacceptable for this purpose and such transformations. This is the reason for converting the image to a color image, where the values of color components which are not measured in the pixel are interpolated from the closest pixels that measure this color. There are various algorithms for the interpolation – so called demosaicing algorithms. A commonly used method is the bilinear interpolation, which computes a weighted average of the values in the nearest four pixels (which form corners of a rectangle in the image) $[x_1, y_1], [x_2, y_1], [x_1, y_2], [x_2, y_2]$

which is linear in both variables,

$$f(x, y) = \left(f(x_1, y_1) \frac{x_2 - x}{x_2 - x_1} + f(x_2, y_1) \frac{x - x_1}{x_2 - x_1} \right) \frac{y_2 - y}{y_2 - y_1} + \left(f(x_1, y_2) \frac{x_2 - x}{x_2 - x_1} + f(x_1, y_2) \frac{x - x_1}{x_2 - x_1} \right) \frac{y - y_1}{y_2 - y_1}.$$

An example of these color-interpolated images can be found in Figure 4.1. The reason why the images are dominated by green is not that the solar corona is green (it might be slightly greenish due to the radiation of Fe XIV on 530.3nm, but this contribution is negligible), it is the sensitivity of the sensors in the camera chip together with the transmissivity of the filters in the Bayer matrix that have maximum in the green part of the spectrum. For the next steps of image processing, the colors in the image are kept as they are, even though they are incorrect for human vision (the values of the color components would have to be multiplied by suitable constants to obtain an image with correct colors for human eyes).⁴ These interpolated images are used as input images in the next step.

4.1.3 Image registration – phase correlation

In applications it often happens that the content of images of the same scene taken at different times has moved. When processing images of the solar corona taken during TSEs, it is practically always true. For processing and analyzing the images it is necessary to transform the images so that the studied structures are at the same position in all the images. This is the task of image registration – to find the transformation.

In some applications we assume that images were shifted only, in others we allow shift, rotation and scale change (i.e. similarity), general linear transformation or even general transformations. If images from a TSE were taken with the same equipment and the focusing did not change between the frames, we can assume that the images are only shifted (rotation caused by rotation of the parallactic is negligible within a few minutes). If images from different cameras and lenses are registered or the lens was refocused, we assume a similarity between the images.

If the images to be registered overlap only partially, the goal of the registration usually is to prepare the images for blending in a panorama or a mosaic. If the positions of the structures in the image differ only slightly among the images, the goal might be increasing the image resolution using subpixel-precision registration or increasing the image quality (noise, dynamic range) by composing more images in one with the same resolution. The methods used for registration depend on the expected transformation and on the structures in the image, e.g. how prominent they are, on which spacial frequencies, if they are organized in regular patterns or not etc. An overview of image registration methods can be found in [cZiF03]. Some methods use corresponding structures or points in the images and then find a global transformation using the measurements of positions of the structures or points. These methods require these structures to be clearly visible. Other methods are based on correlation and work with the image as a whole. The phase correlation proved to be a powerful tool not only for registration of images of the solar

⁴There is no need for the images to have true colors, it is the opposite – normalizing the colors by the spectral sensitivity of the human eye would cause the resulting image to be more noisy.

corona. It can register images taken with different exposure times, different distribution of diffuse light, can be extended to subpixel precision and can be used to estimate either image shift or similarity.

The principle of the method

The idea of the phase correlation method for image registration was first published by Kuglin and Hines in 1975 [cKuH75]. I treated the phase correlation, its principles and the mathematical background in details in my master thesis [aDru10] and it was the main source for this section. The method is based on the Fourier transform. It is more easily described with the Fourier transform of functions $f : \mathbb{R}^2 \rightarrow \mathbb{C}$ and then the practical computations are done with the discrete Fourier transform, more precisely the Fast Fourier transform or other fast algorithms that implement the discrete Fourier transform.

The whole process is done with the brightness component of the image (a weighted average of the red, green, and blue color components of the image, green has higher weight than the other components). In the following reasoning, f will be a gray-scale image of the brightness component of the image.

To show the principle of the phase correlation, we define the *normalized cross-power spectrum* of functions f_1, f_2

$$Z_{f_1, f_2}(\xi, \eta) = \frac{F_1(\xi, \eta) \cdot F_2^*(\xi, \eta)}{|F_1(\xi, \eta) \cdot F_2(\xi, \eta)|},$$

where $*$ means complex conjugation, and the *phase-correlation function*

$$P_{f_1, f_2}(x, y) = \mathcal{F}^{-1} \{ Z_{f_1, f_2}(\xi, \eta) \} = \mathcal{F}^{-1} \left\{ \frac{F_1(\xi, \eta) \cdot F_2^*(\xi, \eta)}{|F_1(\xi, \eta) \cdot F_2(\xi, \eta)|} \right\}. \quad (4.12)$$

It can be proved that (see [aDru10]) for real functions f_1, f_2 the phase-correlation function is real, even with further modifications

$$\mathcal{F}^{-1} \left\{ H(\xi, \eta) \cdot \frac{F_1(\xi, \eta) \cdot F_2^*(\xi, \eta)}{(|F_1(\xi, \eta)| + p) \cdot (|F_2(\xi, \eta)| + q)} \right\}, \quad (4.13)$$

where $H(\xi, \eta)$ is a bounded real function such that $H(\xi, \eta) = H(-\xi, -\eta)$ a $p, q > 0$ are arbitrary constants. This is of great value, since it enables us to search for extremes of the phase-correlation function.

Shifted images: The phase-correlation function of a function with itself is the δ -distribution

$$P_{f, f}(x, y) = \mathcal{F}^{-1} \left\{ \frac{F(\xi, \eta) \cdot F^*(\xi, \eta)}{|F(\xi, \eta) \cdot F(\xi, \eta)|} \right\} = \mathcal{F}^{-1} \{1\} = \delta(x, y).$$

If two functions are shifted in arguments, $f_2(x, y) = f_1(x - x_0, y - y_0)$, their Fourier transforms are shifted in phase

$$F_2(\xi, \eta) = F_1(\xi, \eta) e^{-i(\xi x_0 + \eta y_0)}$$

and their phase-correlation function is the δ -distribution shifted in arguments by the opposite shift vector

$$Z_{f_1, f_2}(\xi, \eta) = \frac{F_1(\xi, \eta) \cdot F_1^*(\xi, \eta) (e^{-i(\xi x_0 + \eta y_0)})^*}{|F_1(\xi, \eta) \cdot F_1(\xi, \eta) e^{-i(\xi x_0 + \eta y_0)}|} = e^{i(\xi x_0 + \eta y_0)}$$

$$P_{f_1, f_2}(x, y) = \mathcal{F}^{-1} \{e^{i(\xi x_0 + \eta y_0)}\} = \delta(x + x_0, y + y_0).$$

This is the main idea of phase correlation. The task to find a shift between two images is converted by the phase correlation to the task of finding the only non-zero point in a matrix (computation using the discrete Fourier transform). If the images are not identical (up to a shift), the phase-correlation function is more complicated, but it still has a global maximum at the coordinates corresponding to the shift vector. To keep this maximum global, Equation (4.12) can be modified with possibilities suggested in Equation (4.13) or modifying directly the original images and the parameters of these modifications can be optimized.

Rotated and shifted images: The phase-correlation function can be also used for estimation of image rotation and rescale. The method was first published by Reddy and Chatterji in 1996 [cReC96].

Let us first describe the method for rotated and shifted images. Let f_2 be function f_1 rotated and shifted in arguments $f_2(x, y) = f_1(x \cos \theta - y \sin \theta - x_0, x \sin \theta + y \cos \theta - y_0)$. Their Fourier spectra and amplitude spectra are related as follows:

$$\begin{aligned} F_2(\xi, \eta) &= e^{-i(\xi x_0 + \eta y_0)} F_1(\xi \cos \theta - \eta \sin \theta, \xi \sin \theta + \eta \cos \theta) \\ A_2(\xi, \eta) &= A_1(\xi \cos \theta - \eta \sin \theta, \xi \sin \theta + \eta \cos \theta). \end{aligned}$$

The shift results in a phase shift and the spectra are rotated in the same way as the original functions. A crucial step here is transformation of the amplitude spectra into the polar coordinate system to obtain functions $A_1^p, A_2^p(\rho, \varphi) : \langle 0, +\infty \rangle \times \langle 0, 2\pi \rangle \rightarrow \mathbb{R}_0^+$ such that

$$A_2^p(\rho, \varphi) = A_1^p(\rho, \varphi + \theta).$$

The rotation around an unknown center of rotation was transformed to a shift. The unknown angle θ can be estimated by means of the phase correlation applied on the amplitude spectra in the polar coordinate system A_1^p, A_2^p . After rotating function f_2 by the computed angle θ , the shift vector (x_0, y_0) is then estimated by means of the standard phase correlation.

Similarity – scaled, rotated, and shifted images: Let f_2 be function f_1 scaled, rotated, and shifted in arguments $f_2(x, y) = f_1(\alpha x \cos \theta - \alpha y \sin \theta - x_0, \alpha x \sin \theta + \alpha y \cos \theta - y_0)$. Their Fourier spectra and amplitude spectra are related as follows:

$$\begin{aligned} F_2(\xi, \eta) &= \frac{1}{\alpha^2} e^{-i(\xi x_0 + \eta y_0)} F_1\left(\frac{\xi}{\alpha} \cos \theta - \frac{\eta}{\alpha} \sin \theta, \frac{\xi}{\alpha} \sin \theta + \frac{\eta}{\alpha} \cos \theta\right) \\ A_2(\xi, \eta) &= \frac{1}{\alpha^2} A_1\left(\frac{\xi}{\alpha} \cos \theta - \frac{\eta}{\alpha} \sin \theta, \frac{\xi}{\alpha} \sin \theta + \frac{\eta}{\alpha} \cos \theta\right) \end{aligned}$$

4.1 WHITE-LIGHT IMAGES ACQUIRED DURING TOTAL SOLAR ECLIPSES

The shift results in a phase shift, the spectra are rotated in the same way as the original functions and scaled with a reciprocal factor. A crucial step here is transformation of the amplitude spectra into the logarithmic-polar coordinate system

$$e^\rho = \sqrt{x^2 + y^2}, \quad x = e^\rho \cos \varphi, \quad y = e^\rho \sin \varphi$$

to obtain $A_1^{lp}, A_2^{lp}(\rho, \varphi) : \mathbb{R} \times \langle 0, 2\pi \rangle \rightarrow \mathbb{R}_0^+$, such that

$$A_2^{lp}(\rho, \varphi) = A_1^{lp}(\rho - \ln \alpha, \varphi + \theta).$$

Both rotation and scale change were transformed to a shift. The unknown angle θ and unknown factor α can be estimated by means of the phase correlation applied on the amplitude spectra in the logarithmic-polar coordinate system A_1^{lp}, A_2^{lp} . After rotating function f_2 back by the estimated angle θ and scaling by factor α , the shift vector (x_0, y_0) is estimated by means of the standard phase correlation.

Practical issues: Amplitude spectra of real functions are even functions $A(\xi, \eta) = A(-\xi, -\eta)$, therefore it is sufficient to use only a half of the domain of the spectra, e.g. $\xi \geq 0$. If amplitude spectra (computed by means of the discrete Fourier transform) are transformed to polar coordinates, only a half of the domain on the angular axis is sufficient.

The amplitude spectra have very high values in $[0, 0]$ and its close neighborhood compared to the rest of the domain, therefore instead of the values of the amplitude spectra it is better to use their logarithms $\ln(1 + A_1(\xi, \eta)), \ln(1 + A_2(\xi, \eta))$ to use the dynamic range of the amplitude spectra more effectively.

The discrete Fourier transform takes images as if they were periodic with period N on both axes. The image edges thus represent a jump in pixel values. Therefore, it is necessary to ‘remove’ image edges, to smooth them out by multiplying them with so called windowing functions. The most common are Gaussian and Hanning window functions. Most commonly they are applied radial-symmetrically. If there are important structures closer to image corners, they may also keep untouched a square or a rectangle and then decrease to zero.

Subpixel-precision image registration: In certain applications, it is necessary to estimate the shift between two images with higher precision than one pixel. The use of methods depends on the structures in the image and on the required precision. Oversampling the image is a robust method, but it leads to immense memory demands. Methods that fit a function through the pixels around the global maximum are suitable for images that are not too different from each other and do not contain much noise. A robust method that proved to be suitable for TSE images is based on geometric moments [cDru09a]. The sub-pixel precision estimate of the shift vector (\bar{x}_0, \bar{y}_0) is computed as

$$[\bar{x}_0, \bar{y}_0] = \left[\frac{M_{1,0}}{M_{0,0}}, \frac{M_{0,1}}{M_{0,0}} \right],$$

where $M_{k,l}$ is the geometric moment computed over a circle with center $[x_0, y_0]$ and radius $\varepsilon \in \mathbb{R}^+$, i.e.

$$M_{k,l} = \sum_{x^2+y^2 < \varepsilon} x^k y^l P(x_0 + x, y_0 + y), \quad k, l = 0, 1,$$

where $P(x, y)$ is the phase correlation function. We may consider the point (\bar{x}_0, \bar{y}_0) as the center of gravity of the peak in P and its neighborhood with radius ε . This computation is then repeated with a center in $[\bar{x}_0, \bar{y}_0]$ and the process is iterated until the computed center of gravity is stable. Usual values of ε range from 3 to 8. This parameter is a parameter which needs to be set manually when two image are to be registered.

The subpixel extension of the phase-correlation method was described for estimating of a non-integer shift between images. It can also be used for enhancing the precision of the estimation of rotation and scale-change between similar images. The only difference is that the integer-valued vector (x_0, y_0) is replaced by a value of $(\ln \alpha, \theta)$ corresponding to integer indices in the matrix representing the phase-correlation function. The subpixel estimation gives us non-integer indices in the matrix, which correspond to a more precise value of $(\ln \alpha, \theta)$.

This method is suitable for images of the solar corona during a TSE, where a precision of a tenth of a pixel is enough. It is not sufficient for detection of local shifts of structures on the solar disk in images from the Solar Dynamics Observatory as it was shown in [aKoD13]. The solution for this application is using the modification of the phase-correlation function of Equation (4.13) and optimizing the shape of the weight function H . Constants p, q are kept very low just to prevent division by zero.

Any subpixel precision method requires high ‘quality’ of the phase-correlation function. Completely different methods from the method described above are used for subpixel precision registration of images that are almost identical, e.g. images taken shortly one after another in a video sequence. Among these methods is fitting functions to the values of P around the global maximum. The shift is then computed as the maximum of the fitted function.

Registration of TSE images

Digital images of the solar corona taken during total solar eclipses are specific in many aspects. The extreme contrast of the solar corona yields the necessity of many images with various exposure times. Images taken with very short exposure times are mostly underexposed with only a small part of the image correctly exposed. There are no stars (except for the Sun) in the images, only the structures of the inner corona and the chromosphere. Images taken with longer exposure times have a part which is overexposed (saturated), a part which is correctly exposed, and a part with very low pixel values containing almost no information. Sometimes, there are stars visible, the innermost corona is saturated. Images taken with the longest exposure times have a large overexposed part and the rest is correctly exposed. Registration methods based on matching corresponding structures are unusable for TSE images. The specific methods and extensions of the phase-correlations used for solar corona image registration are described in [cDru09a].

Usually, there are not many structures visible in the original images. There is very high contrast, which may be eliminated by using a suitable high-pass weight function on the normalized cross-power spectrum. However, there are aspects that cause that it is better to replace the high-pass weight function by another procedure. The most contrasty structure in solar corona images from total solar eclipses is the edge of the Moon. The Moon moves in front of the Sun during the eclipse, which causes that registration of the images with respect to the Moon does not give the same results as registration with respect to the corona. If we do not remove the Moon edge from the images used for image

4.1 WHITE-LIGHT IMAGES ACQUIRED DURING TOTAL SOLAR ECLIPSES

registration, the images will be registered to the Moon and the corona will be registered incorrectly. Furthermore, a contrasty and sharp structure in the images is the edge of the saturated part of the image.

A solution to this problem is masking out the Moon and the edge of the saturated part and removing the information on spatial frequencies in radial direction and preserving the information on the spatial frequencies in tangential direction only. This cannot be done by applying a weight function on the spectrum. A weight function is unable to treat the image differently in its different parts (inside the Moon's disk, at its edge, in the corona). This must be done by a filter T_ς applied on the images

$$T_\varsigma(f(r, \varphi)) = f(r, \varphi) - \frac{1}{\varsigma\sqrt{2\pi}} \int_{l_1}^{l_2} f\left(r, \varphi + \frac{l}{\rho}\right) e^{-\frac{l^2}{2\varsigma^2}} dl, \quad (4.14)$$

The origin (o_x, o_y) of the polar coordinate system should be in the center of the Sun, which is not easy to be found at this stage of the process. Therefore the center of the Moon is used instead as its approximation, which has no influence on the precision of image registration. The integral in formula (4.14) may be understood as an unsharp mask created by means of a one-dimensional low-pass filter with Gaussian kernel applied along a circle centered in the center of the Sun. Limits l_1, l_2 are usually set to $l_1 = -3\varsigma, l_2 = 3\varsigma$. The value of ς must be chosen according to the image quality. For sharp images, we choose e.g. $\varsigma = 8$, for less sharp images, we increase ς slightly. Since $f(x, y)$ is defined only for integer-valued (x, y) , its values must be interpolated to compute the integral, the final value is then rounded for each pixel. Such a filter gives both positive and negative pixel values, therefore the image after filtration is stored in a signed type array, e.g. $\{-32\,768, \dots, 32\,767\}$.

The window function must be applied too. Due to the shape of the solar corona, circular window functions are usually more suitable and also faster. However, a bigger part of the images is discarded. If the exposure time of the image was long and a large part of the image is saturated, there is only little space left in the annulus between the edge of the saturated part and the image edge. Then it is better to use a rectangular window function so that we use the image structures far from the center of the Sun. Moreover, it is necessary to remove the edge of the Moon and the edge of the saturated part. Therefore, the window function has to vanish both at the edge of the Moon / saturated part and the edge of the image.

The transformation is estimated from the filtered image and then is applied on the original image too. The whole process of registration of all images in one image set starts from an image with the longest exposure time that has no saturated part and continues step-by-step to shorter exposure times and longer exposure times (which have a saturated part). When the quality of the global maximum of the phase-correlation function becomes not acceptable, all registered images are averaged in one, it is filtered, and used as the master image for further registration. An example of original images of the solar corona (in linear brightness scale) and filtered images used for the estimation of scale-change, rotation and shift is in Figure 4.3.

One more parameter is user-optimized when images of the TSE are registered. It is the shape of the low-pass weight function H in Equation (4.13). We use Gaussian low-pass weight function, the optimized parameter is the variance. If it was not employed, $(0, 0)$ would often be the estimated shift vector, which corresponds to dust particles on the chip

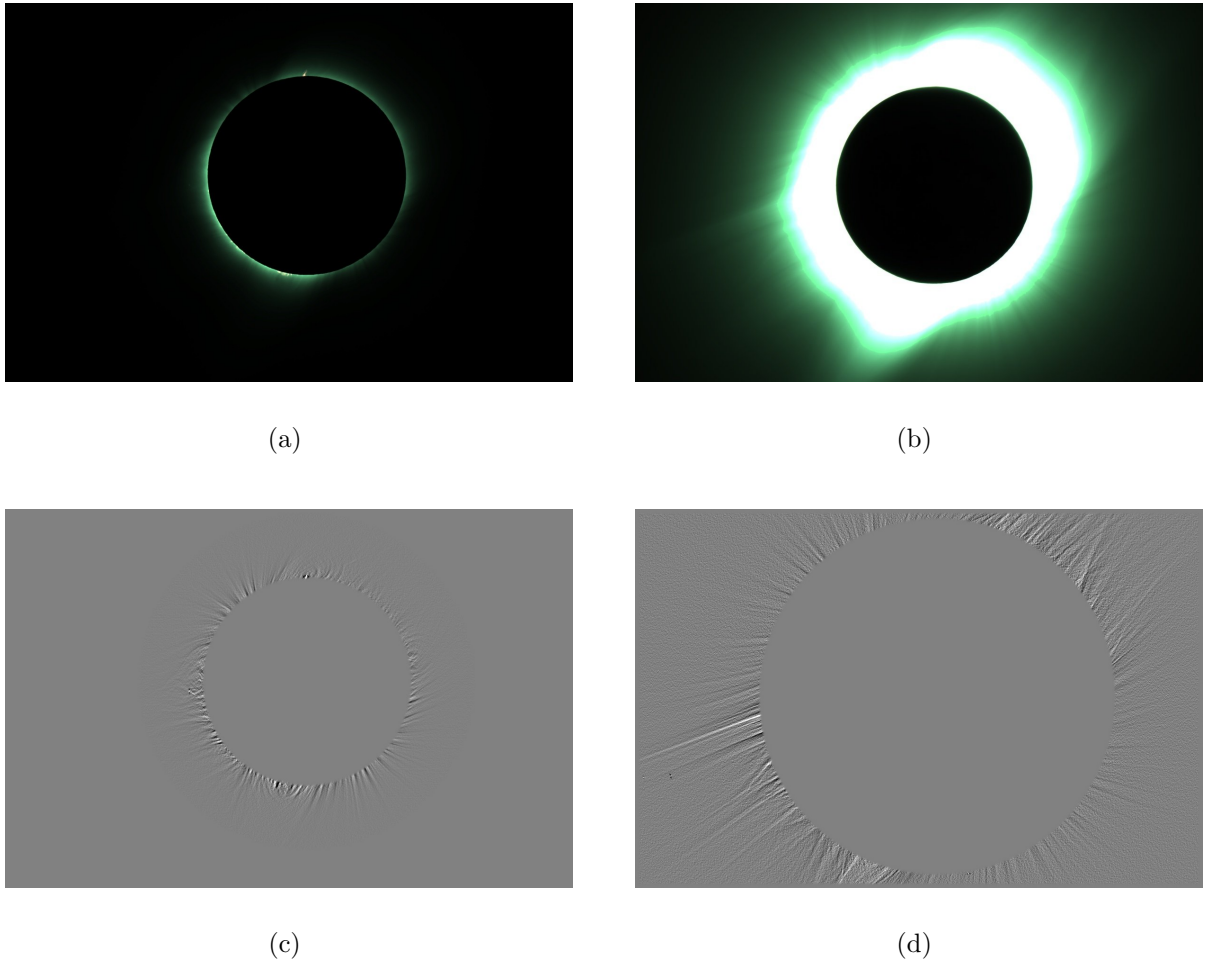


Figure 4.3: Example of solar corona images taken during a total solar eclipse. Images were taken by Constantinos Emmanoulidis in Akademgorodok, Novosibirsk, Russia on August 1, 2008 with digital camera Canon EOS 400D and Takahashi TSA102 814 mm lens. The exposure times were 1/60 s (image a) and 2 s (image b). Image (c) was created from image (a) using filter T_8 and a circular window function, image (d) was created from image (b) using filter T_8 and a rectangular window function. The exposure time of image (b) was so long that it was necessary to use a rectangular window function. Image taken from [aDru10].

and the structure of the chip. Higher values are generally used for poorer-quality images and images with bad correspondence.

4.1.4 Image composition

From the previous steps, we have a set of images that all have the same radius of the Sun and position of the center of the Sun. They were taken with different exposure times. The next step is composing all these images in one image that covers the whole brightness range of the set of images. The family of methods that solve this problem is called the high-dynamic-range imaging (HDR). Many HDR-processed images of landscape can be found on the Internet. Many of these images are quite realistic, however, they are unusable

for further scientific analysis. Different parts of the images are processed differently so that none of the image parts is too dark or too bright. Beautiful galleries of HDR-processed images can be found on the Internet, for instance: <http://www.hdrsoft.com/gallery/>. As a result, the transformation that is applied to the image is not a pixel-value transformation in the sense of Definition 3.26 on page 25. Comparing two pixels in a HDR-processed image, if one of them is brighter than the other, there is no way to tell if the light intensity in the first pixel is higher than the other. For photometry and for structure enhancement, the property of monotone dependence of the image brightness on the intensity of the incident light is crucial.

A suitable method for composing digital images for scientific purposes has to respect the linearity of the images in the image set. The composed image has to have monotone (ideally linear) dependence of the pixel value on the intensity of the incident light. Such a method can be realized by computing a weighted average of the images ignoring those parts of the images that are saturated or near to saturation and possibly also those parts of the images that contain only noise.

Linear Digital Image Composer

The method implemented by Miloslav Druckmüller in the Liner Digital Image Composer (LDIC) in 2006 produces HDR-composed images that are suitable for structure enhancement and photometry. LDIC computes a weighted sum of the set of the images, the weights are applied both based on the pixel value and on the exposure time of each image (more exactly on the brightness of the image, which is closely related to the exposure time)

$$g(r, \varphi) = \sum_{i=0}^{N-1} w(f_i(r, \varphi)) \cdot (k_i(\varphi)f_i(r, \varphi) + q_i(\varphi)). \quad (4.15)$$

g is the composed image, $\{f_i\}_{i=0}^{N-1}$ is the set of the images that are composed.

w is a weight function depending on pixel value. The lowest part of the dynamic range contains mostly noise. Adding it to the composed image would only increase its noise, it would not bring much information. There is also a reason why the highest part of the dynamic range have to be rejected. The highest value (65535 for word) is in completely saturated pixels. The camera response to incident light intensity is linear in a majority of the dynamic range of the images, however, the highest part of the dynamic range (may start from about 85 % of the dynamic range) does not show perfect linearity. This is the reason why pixel values in the highest part of the dynamic range have to be rejected too. This is the role of w . It is equal to one on a majority of the dynamic range, equal to zero in the highest and the lowest part of the dynamic range, with gradual and continuous transitions.

k and q are piecewise linear functions of φ for each image. They form a linear transformation. The image is split in $n_s = 60$ angular segments. The composition starts from the longest exposure times (the list of the image files together with exposure times and much more information is provided by the user). The linear transformation that transforms the image to be added to all already added images is determined by liner regression for each angular segment separately. The next step is approximation of the coefficients of the linear transformation by a trigonometric polynomial of a low order (0, 1, 2, or 4). These approximations are then taken as $k_i(\varphi)$ and $q_i(\varphi)$, the approximations are a linear

function of φ in each angular segment. This means that the sum in Equation (4.15) is enumerated step-by-step, functions $k_i(\varphi)$ and $q_i(\varphi)$ depend on the sum up to the $(i-1)$ th image.

Figure 4.4 documents the principle of the composition method used in the LDIC.

Exposure 2 s

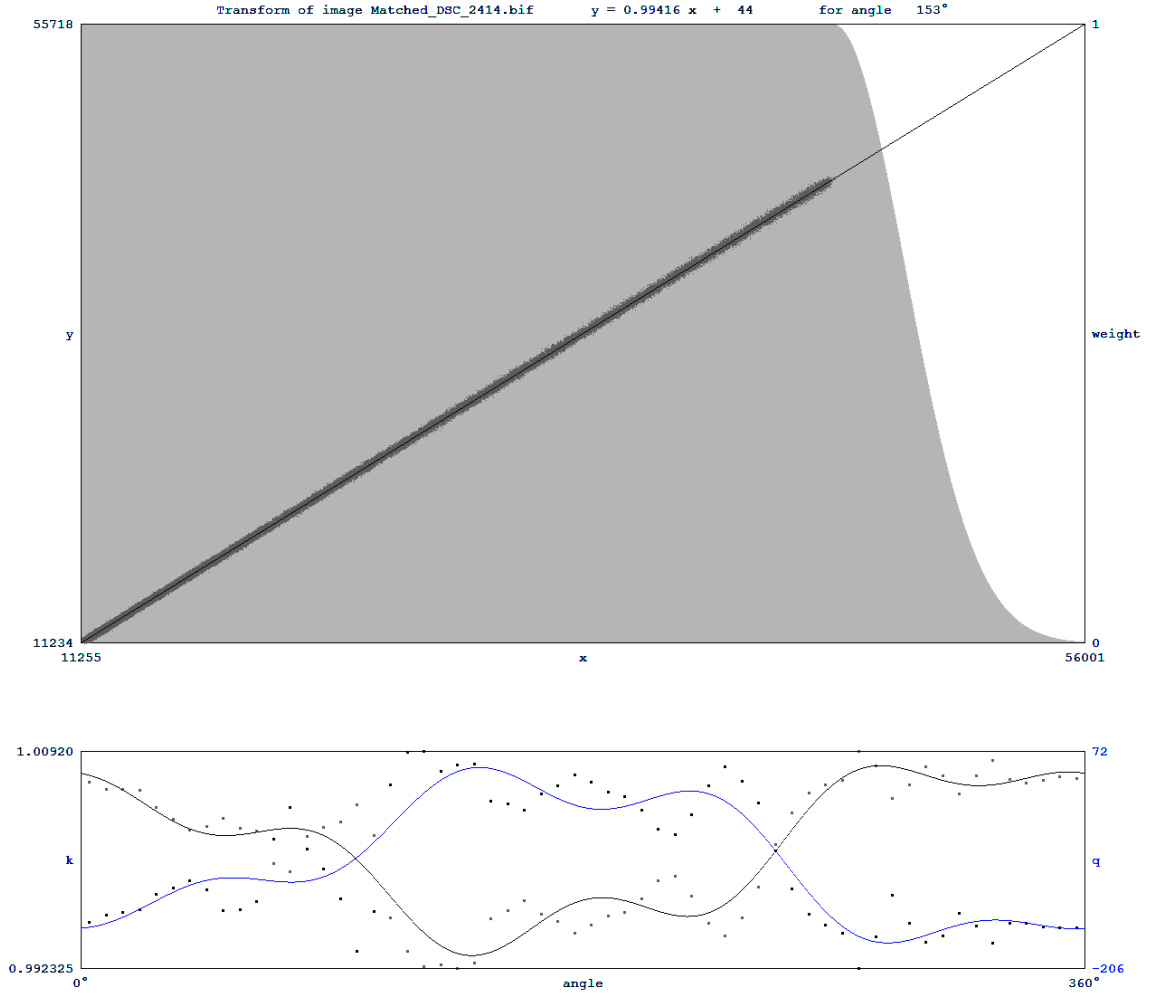


Figure 4.4: A screenshot from the LDIC illustrating the principle of the composition. The upper panel shows the linear transformation for a certain angular segment, the lower panel shows the coefficient k for the linear transformation for each segment and its approximation with a trigonometric polynomial of order four. The graph on the background of the upper panel is the weight function w .

The LDIC is much more powerful and complicated than just computing a weighted sum of images. It has to compose colors in the image correctly. It has to follow the moving position of the Moon, possibly even making a sharp composition of the Earth-lit Moon in the eclipse images. There are many parameters that affect the result. The adaptivity that functions k and q are computed separately for each segment allows to compose images with different distribution of diffuse light in the optical system (e.g. shortly after the beginning of the total eclipse and shortly before its end) or even images that were taken through thin clouds.

As a result, the method fulfills the monotone property that makes it suitable for scientific analysis. There may be only slight discrepancies in the monotonicity caused by LDIC compensating for the diffuse light in the optical system or for clouds. The composed image is very close to eliminating these effects and keeping the monotonicity property for the incident light (more precisely the light incident to the Earth's atmosphere above the clouds and out of the optical system).

After this step, the composed image is ready for structure enhancement. It is an image that will be called the *original image* in the chapters about structure enhancement in images of the solar corona (Chapters 5, 6). In some cases, there might be additional steps required, such as removing darker spots in the images caused by dust particles on the chip (with patches taken from another image set).

Comment: Determination of the position of the Sun and its radius

The position of the center of the Sun $O = [o_x, o_y]$ and its radius o_r is a substantial information not only for image composition, but also for structure enhancement. The images that are composed are registered, i.e. the position of the Sun in all these images is identical – and unknown. It is quite a simple process described in the appendix of [aDMH11] that requires the following information:

- Movement of the Moon in the images described by its position at C2 $[h_{x,0}, h_{y,0}]$ (center of the Moon), the shift vector the Moon moves by in one second (h_{dx}, h_{dy}) , and the radius of the Moon in pixels h_r . All these values are measured from several images where the edge of the Moon is clearly visible, i.e. images taken with shorter exposure times. A minimum is one image after C2 and one before C3. (C2 means the beginning of the total eclipse, C3 the end of the total eclipse.)
- Duration of the eclipse l , ratio of the size of the Moon and the Sun in the sky R_{ho} , umbral depth B in percent (a number that is 100% on the central line of the totality belt and 0% on its edges), information whether the observer was to the north or south from the central line. These information can be calculated for the particular eclipse and observing site using an eclipse calculator, one of which is <http://www.chris.obyrne.com/Eclipses/calculator.html>. It is an important feature that it uses JavaScript, the form works offline and can be used at remote observing sites with no access to the Internet.

The position of the Moon in the images is

$$\begin{aligned} h_x &= h_{x,0} + t \cdot h_{dx} \\ h_y &= h_{y,0} + t \cdot h_{dy}, \quad t \in \langle 0, l \rangle. \end{aligned}$$

The radius of the Sun in pixels o_r is computed from the measured radius of the Moon h_r and the ratio Moon : Sun as

$$o_r = \frac{h_r}{R_{ho}}.$$

The umbral depth B and the north / south position in the totality belt are converted number $\beta \in \langle -0.5, 0.5 \rangle$ with $\beta = -0.5$ on the northern edge of the totality belt and $\beta = 0.5$ on the southern edge

$$\beta = \begin{cases} h = -\left(0.5 - \frac{B}{200}\right) & \text{northern part of totality belt} \\ h = 0.5 - \frac{B}{200} & \text{southern part of totality belt.} \end{cases}$$

Next, denote

$$\delta = 2h(h_r - o_r)$$

the distance in pixels of the center of the Sun from the center of the Moon in the middle of the eclipse due to the eccentricity of the observer in the totality belt. δ is the length of the shift vector, we will have to determine its components as well. A vector that is perpendicular to the motion of the Moon in the images is

$$(n_x, n_y) = (h_{dx}, -h_{dy}).$$

The vector of the shift between the center of the Moon and the Sun in the middle of the eclipse is vector (n_x, n_y) resized to length δ

$$\begin{aligned} v &= \sqrt{n_x^2 + n_y^2} = \sqrt{h_{dx}^2 + h_{dy}^2} \\ n_{\delta,x} &= \delta \frac{n_x}{v} \\ n_{\delta,y} &= \delta \frac{n_y}{v} \end{aligned}$$

Finally, the center of the Sun in the image $[o_x, o_y]$ is the position of the center of the Moon in the middle of the eclipse shifted by $(n_{\delta,x}, n_{\delta,y})$

$$\begin{aligned} o_x &= h_{x,0} + \frac{l}{2} h_{dx} + n_{\delta,x} \\ o_y &= h_{y,0} + \frac{l}{2} h_{dy} + n_{\delta,y}. \end{aligned}$$

4.2 Images in spectral lines acquired during total solar eclipses

Images in spectral lines are images that show the radiation of one particular atom or ion at a specified spectral line. In the case of spectral lines in the visible and near-visible wavelength ranges, an image acquired through a narrow-band filter selecting this line contains not only the radiation of the ion or atom, but also of the underlying continuum. This section describes the importance of these observations, how the radiation of the atom or ion is extracted and how these images are processed.

In the previous section, the process of image acquisition and processing of white-light images of the solar corona taken during total solar eclipses was described. This section is much shorter, because most of the steps applied to images taken in spectral lines are similar to those applied to white-light images. It is partially based Habbal et al. [aHDM11].

4.2.1 Importance of observations in spectral lines during total solar eclipses

Observations from cosmic probes in extreme-ultraviolet (EUV) and X-ray wavelength ranges enable us to study the structures of the solar corona simultaneously on the solar disk and off the limb, since the photosphere is completely black in these wavelength ranges. However, the capabilities of the EUV lines and X-rays are limited to distances below about $1.5 R_{\odot}$ due to the inherent dominance of their collisional component in the

intensity of their emission, which decreases with height as the square of density. Spectral lines in the ultraviolet typically above 100 nm and in the visible and near infrared part of the spectrum, on the other hand, have a radiative component, which allow observations higher in the corona. Due to the radiation of photosphere on these wavelengths, an occulter is needed. Among successes in this field were the observation of the Ly α hydrogen line and the O VI 103.2 nm and 103.7 nm doublet lines from the Ultraviolet Coronagraph Spectrometer on the Solar Heliospheric Observatory [cKEG95]. The limits of observable heights were increased from $1.5 R_{\odot}$ to about $10 R_{\odot}$. Lower heights than $1.5 R_{\odot}$ were only observable without a coronagraph, which means with the Moon as the occulter during a total solar eclipse (of in other wavelength ranges in lines without the radiative component).

Observing conditions during total solar eclipses with the Moon as an ‘ideal’ occulter are unique opportunities for observing the spectral lines of heavy ions with radiative components both close to the limb and further from the Sun in high quality and resolution. The team of prof. Habbal recently showed that coronal forbidden lines in the visible and near infrared wavelength range provide diagnostic capabilities for exploring the inner corona which had been overlooked so far. Among them revealing the importance of Fe XI 789.2 nm line first observed during the total solar eclipse of 2006 [cHMJ07]. The radiative component is also present in other spectral lines of Fe ions in the visible and near infrared part of the spectrum, namely Fe X 637.4 nm, Fe XIII 1074.7 nm, and Fe XIV 530.3 nm [aHDM11]. Eclipse observations allow to observe these lines up to $3 R_{\odot}$.

An important property of the spectral lines with a radiative component of iron ions Fe IX, Fe X, Fe XI, Fe XIII, and Fe XIV in visible and near infrared wavelength ranges is that they are forbidden. The life times of the their excited states are longer than 10^{-3} s, whereas lines in the EUV have a life time about 10^{-12} s. Observations in spectral lines of Fe ions with a radiative component led to several discoveries of structures and their properties and origin in the inner solar corona. They led to identification of the locus of transition from collision-dominated to a collisionless plasma around 1.25 to $1.5 R_{\odot}$ [cHDM10a]. They also enabled the construction of the first two-dimensional maps of electron temperature and charge states in the corona [cHDM10b]. The temperature maps revealed the nature of prominences as the coolest suspended structures in the corona surrounded by the hottest coronal plasma [cHDM10a]. These results were enabled by the simultaneous observations of the corona in several iron lines together with white-light observations. These were also composed into images showing the radiation of more lines in one image, each line in different color. An example of such image is the composition of Fe X and Fe XIV images as observed during the 2010 TSE in Figure 4.5. The image shows active regions with intricate structures and closed field lines of the magnetic field in green representing Fe XIV, whose ionization temperature is about 1.8 MK, whereas polar regions and open lines⁵ of the solar magnetic field are dominated with cooler (0.8 MK) Fe X. These detailed images of the radiation of heavy ions with strong radiative component in the innermost corona can only be obtained during total solar eclipses. Together with white-light observations of the corona they keep the uniqueness of total solar eclipse observations.

⁵No field line of a magnetic field can be open in principle. When using the term ‘open field line’ in connection with the solar corona, it is mean that the loop of the field line is large, it goes out of the image, often much further, some of the loops are as large as the Solar System.

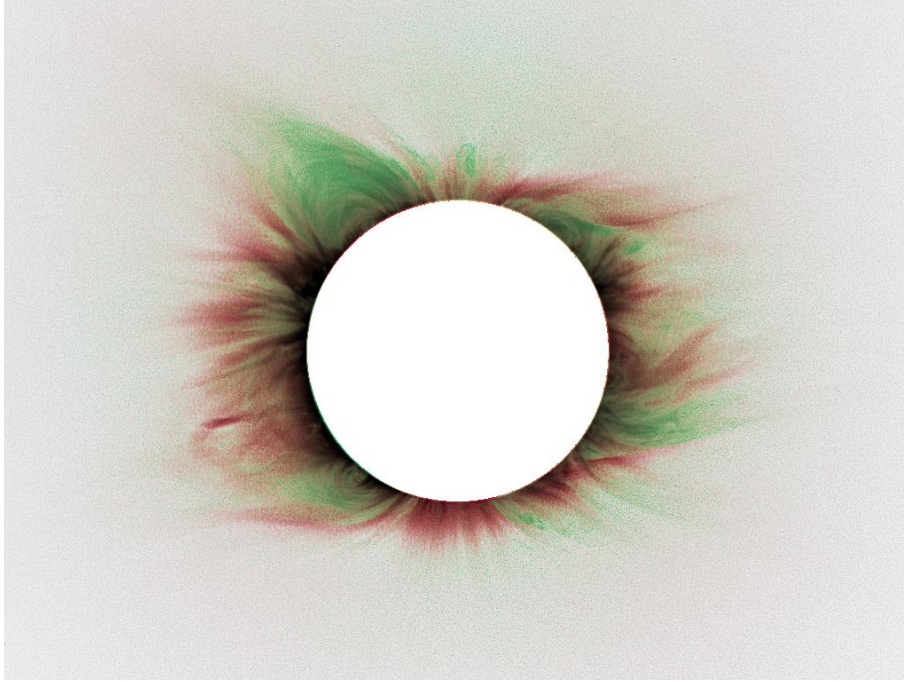


Figure 4.5: A composition of the Fe X (red) and Fe XIV (green) images as observed during the 2010 TSE (in negative). Images were calibrated so that both lines have the same average intensity. The same amount of these colors is yellow, red is where Fe X dominates and green is where Fe XIV dominates. Image taken from [aHDM11].

4.2.2 Principle of observation in spectral lines in the visible part of the spectrum

One of the advantages of observation in spectral lines that lie in the visible part of the spectrum is that they can be observed from the Earth. The disadvantage is that they can be observed in a good resolution only during a total solar eclipse, because there is a strong radiation of the K-corona in the visible range. The K-corona is formed by the photospheric light scattered on free electrons in the corona. Its spectrum is continuous. Therefore, if an image is taken with a narrow-band filter selecting a narrow range containing a prominent spectral line such as the Fe XIV 530.3 nm (which is close to the maximum of the K-corona radiation at 500.2 nm), it contains both the radiation of Fe ions and the photospheric light scattered on free electrons. Therefore, another image free of emission lines has to be taken close to this wavelength. The difference in K-corona radiation between these two images is negligible, therefore by subtracting these images the radiation of the Fe ion is isolated (For precise calibration described below, we even do not assume the difference to be negligible.). The former image is called the *on-line* image, the latter is called the *off-line* image. An example of an on-line and an off-line image is shown in Figure 4.6.

Due to the fact that only a narrow section of the spectrum is observed, scientific cameras giving gray-scale images are the most suitable. If a standard DSLR camera is used, only a part (a half or a fourth) of all pixels are used, the rest of them is completely black, where the transmissivity of the filter and on the color filter of the Bayer matrix in the camera has zero product. Or, the line can lie in a wavelength range where two color filters have non-zero transmissivity, then the image is recorded in two color groups of pixels, but at least one of the groups gives low signal. Front-illuminated chips are

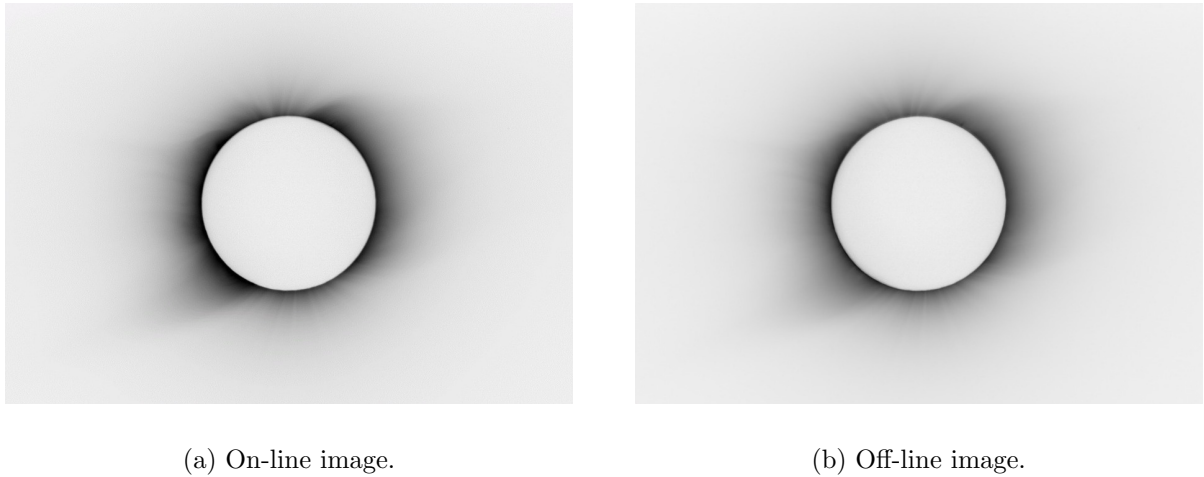


Figure 4.6: The on-line and off-line images of the Fe XIV 530.3 nm line as observed during the 2008 TSE by the Czech-Slovak-German expedition in Mongolia (in negative). Both filters used had bandwidth 0.15 nm, the on-line filter was centered at 530.3 nm, the off-line filter at 529.1 nm. It can be seen that both images show the same structures of the K-corona with the on-line image showing also intricate structures in the innermost corona which are formed by the Fe XIV radiation. Taken from [dDru09].

necessary for this type of observations. Back-illuminated chips have in general higher quantum efficiency, however etaloning causes prominent patterns in the images, which makes this type of cameras completely unusable for narrow-band observations.

There are two approaches to the use of narrow-band filters for eclipse observations. The *tilting method* requires only one camera and one filter for each spectral line, the filter is tilted between taking images. The tilting shifts the transmissivity of the filter out of the spectral line for taking off-line images. The other method involves two cameras with two filters tuned at the desired wavelengths. Images are taken with the same exposure time simultaneously with both cameras. The advantage of the first method is the lower number of cameras, lenses and filters required. Its disadvantage compared to the two-filter method is that only less than half the images can be taken during the eclipse. The fact that images are not taken simultaneously can also cause severe problems if the observing conditions are changing during the eclipse. It is not only when clouds are moving in the sky during the totality, but also the changes in the sky brightness during the eclipse. In both these methods, the cameras have to be controlled automatically, the control software depends on the type of the camera.

The exposure sequences for on-line and off-line images have to be identical, they have to be chosen based on the transmissivity of the filters, on the quantum efficiency of the cameras at the wavelength and on the intensity of the K-corona at this wavelength.

The sequence of steps for processing on-line and off-line images including the calibration, registration, subtraction, composition and structure enhancement is described in the following section.

4.2.3 Processing images in spectral lines

The first step after obtaining on-line and off-line images and their calibration images is image calibration. The algorithm is identical with the one described in Section 4.1.2 for gray-scale images. For the tilting method, the sets of dark-frames and bias frames are identical for on-line and off-line images, because the camera and the lens are identical for both image sets. Flat-field images are generally different. For the two-camera method, the image sets are calibrated as two independent sets.

The next step is image registration. Since all images contain the radiation of the K-corona, the continuum, they have common structures and they can be all registered as one image set. The phase-correlation method for image registration is described in Section 4.1.3.

In the image composition step (Section 4.1.4), it may make sense to compute the on-line and off-line composites (as shown in Figure 4.6), but the aim of the process is the image of radiation of the particular ions, which is the difference of the on-line and off-line image. This means that for each couple of images with the same exposure time, one of them on-line, the other off-line, their weighted difference is computed [aHDM11]

$$f_i(x, y) = f_{1,i}(x, y) - w f_{0,i}(x, y), \quad w = \frac{I_1}{I_0} \cdot \frac{L_1}{L_0}.$$

f_i is an image of one particular exposure time showing the radiation of the ion at the selected spectral line, i goes from 1 to the number of acquired couples of images. Images $f_{1,i}$ are on-line images, $f_{0,i}$ are corresponding off-line images. I_0, I_1 are intensities of the continuum at the wavelengths of the peak in transmissivity of each filter, L_0, L_1 are intensities of the flat-field panel at these wavelengths. Images f_i are composed in one high-dynamic range image, which should be stored in an appropriate data file, e.g. a 64bit per pixel file (gray-scale).

The final step is structure enhancement. These images have lower signal to noise ratio compared to white-light images of the corona observed during TSEs, which affects the suitability of structure enhancement methods. The standard method is the Normalizing-radial-graded filter (NRGF, Section 5.3), which is fast and does not require any user manipulation. The Adaptive-high-pass filter (ACHF, Section 5.2) is able to visualize smaller-scale structures compared to the NRGF, but it is not able to go that far from the Sun. A method that combines the advantages of both these methods is the Fourier normalizing-radial-graded filter (FNRGF) proposed in this thesis in Chapter 6. The results of application of these methods to all spectral-line images acquired by the team of prof. Habbal during the 2010 TSE can be found in [aHDM11] (NRGF and ACHF) and [aDMH11] (FNRGF).

There is also a completely alternative approach of visualization of the prominent Fe XIV line from images obtained with standard DSLR cameras without a narrow-band filter by precise calibration of color components. The method was tested on 2008 TSE images [aMaD11].

4.3 Images from cosmic probes

Cosmic probes produce terabytes of data every day. They enable us to study the Sun in various parts of the spectrum from extreme ultraviolet to visible light (radio waves are observed with Earth-based instruments), to measure the properties of the solar wind, to acquire dopplergrams, magnetograms etc. Majority of the data are available to the public on Internet search machines, e.g. [dVso13]. Images are stored in the standard astronomic format FITS, whose header contains a complete description of the data (image properties, properties of the instrument, position and orientation of the Sun in the image and many others). Processing data from cosmic probes in batch to produce an animation is an opportunity to study the dynamics of the coronal structures far beyond the possibilities of animation of images from TSEs from different sites along the totality belt. Total solar eclipses retain their uniqueness in white light and in spectral lines of the visible spectrum in the innermost corona. The list of most important cosmic probes to acquire images of the Sun are listed in the Section 4.3.1 followed by a brief account of processing methods applied to these images.

4.3.1 List of cosmic probes

The most important cosmic probes that study the Sun are listed in this section.

Yohkoh (Sunbeam in Japanese) [dYoh01] was a project of the Japanese Institute of Space and Astronautical Science together with teams of the space agencies from the Unites States and the United Kingdom (1991-2001). The instrument observed the corona during one cycle of solar activity. The scientific objective was to observe the energetic phenomena taking place on the Sun, specifically solar flares in X-ray and gamma-ray emissions. The Yohkoh Spacecraft was in a slightly elliptical low-Earth orbit, with an altitude ranging from approximately 570 km to 730 km. The orbital period was 90 minutes. It carried two spectrometers (Bragg Crystal Spectrometer, Wide Band Spectrometer) and two telescopes observing in X-rays.

Soft X-ray Telescope (SXT) with with a 1024×1024 CCD camera and a filter wheel with various filters.

Hard X-ray Telescope (HXT) sensitive to photons with energies from 14 keV to 93 keV, this range was split into four energy bands (called L, M1, M2, H). The angular resolution was about $5''$, image synthesis field of view is $2' \times 2'$. It conducted X-ray observation in the region of more than 30 keV as an imaging telescope for the first time in the world.

Solar and Heliospheric Observatory (SOHO) [dFle11, dWik13a] is a project of international cooperation between ESA and NASA to study the Sun, from its deep core to the outer corona, and the solar wind. Launched in December 1995, it begun normal operation in May 1996 in a plane passing through the First Lagrangian Point L1 point (a point of gravitational balance located approximately 0.99 astronomical unit (AU) from the Sun and 0.01 AU from the Earth). Originally planned as a two-year mission, SOHO currently continues to operate after over seventeen years in space. During the years, SOHO succeeded in measuring the acceleration of the slow and fast solar wind, identifying the source regions and acceleration mechanism of the

fast solar wind in the magnetically ‘open’ regions at the Sun’s poles and discovering new dynamic solar phenomena such as coronal waves and solar tornadoes. It brought a revolution in forecasting the space weather. It enabled a discovery of thousands of comets. There are twelve instruments aboard SOHO, among them instruments for coronal spectrometry and spectroscopy, charge, element, and isotope analysis, solar oscillation measurement, radiation measurement etc. The instruments are (among others) as follows:

Extreme ultraviolet Imaging Telescope (EIT) [cDAB95] provides full-disk images of the Sun in extreme ultraviolet (Fe IX/X at 171 Å, Fe XII at 195 Å, Fe XV at 284 Å, He II at 304 Å [dGur10]) thus enabling studies of the innermost corona. An example of and EIT image is in Figure 6.8 on page 88.

Large Angle and Spectrometric Coronagraph (LASCO) [cBHK95] contains three coronagraphs C1, C2, C3 to capture the corona in 1.1 to 3 R_{\odot} , 1.5 to 6 R_{\odot} , and 3.7 to 30 R_{\odot} respectively, which is about one seventh of the distance between the Sun and the Earth. Images from LASCO coronagraphs enabled the discoveries of thousands of comets. C1 is equipped with a tuneable, narrow band Fabry-Perot filter, whereas C2 and C3 are regular white-light coronagraphs. C1 stopped working in 1998, C2 and C3 are still operating. Images from LASCO C2 are also used in this thesis – see Figures 2.3 and 6.9 on pages 8 and 89.

Michelson Doppler Imager/Solar Oscillations Investigation (MDI/SOI).

UltraViolet Coronagraph Spectrometer (UVCS) makes measurements in ultraviolet light of the solar corona (between about 1.3 and 12 R_{\odot}) with a coronagraph. It blocks the bright light from the solar disc and allows observation of the less intense emission from the extended corona. UVCS provides valuable information about the microscopic and macroscopic behavior of the highly ionized coronal plasma.

Transition Region And Coronal Explorer (TRACE) [dLMM10, dWik13d] was a NASA space telescope (1998-2010) designed to investigate the connections between fine-scale magnetic fields and the associated plasma structures on the Sun. It was providing 1024×1024 images from a CCD detector giving an 8.5 arc minute field of view (a Cassegrain reflector with 30 cm diameter and focal length of 8.66 m). It observed the solar photosphere and transition region to the corona. A main focus of the TRACE instrument was the fine structure of coronal loops low in the solar atmosphere. The telescope is designed to take correlated images in a range of wavelengths from visible light, through the Lyman alpha line to far ultraviolet. The different wavelength passbands (see Table 4.1) correspond to plasma emission temperatures from 4 000 to 4 000 000 K. An example of an image acquired by TRACE can be found in Figure 4.7.

Solar Terrestrial Relations Observatory (STEREO) [dSte13, dWik13c], launched in 2006, is a NASA mission composed of two almost identical spacecrafts (STEREO A, STEREO B) that observe the Sun from different positions in the ecliptic plane, one ahead of Earth in its orbit (on an orbit closer to the Sun), the other trailing behind (on an orbit further from the Sun). This gives a unique opportunity to

4.3 IMAGES FROM COSMIC PROBES

Wavelength [\AA]	Width [\AA]	Observed	Temperature [kK]
5000	broad	continuum	4 - 6.4
1700	200	continuum	4 - 10
1600	275	C I, Fe II, continuum	4 - 10
1550	20	C IV	60 - 250
1216	84	HI Ly α	10-30
173	604	Fe IX	160 - 2000
195	645	Fe XII	500 - 2000
284	10.7	Fe XV	1250 - 4000

Table 4.1: Wavelength bandpasses observed by TRACE. Taken from a subpage of [dLMM10] – <http://trace.lmsal.com/Project/Instrument/inspass.htm>

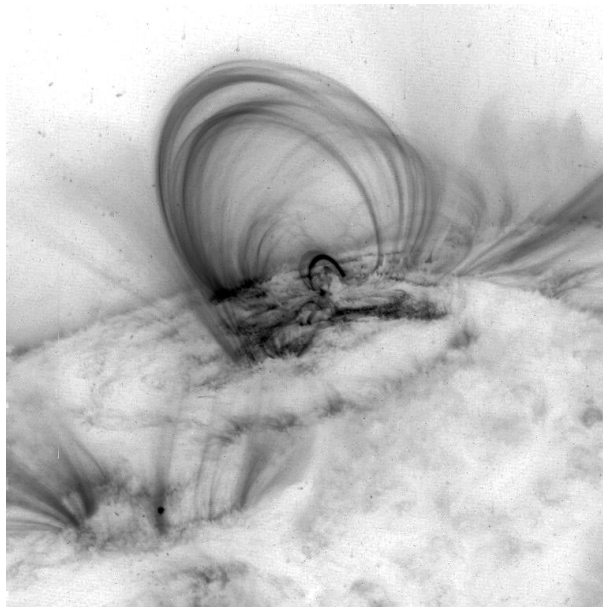


Figure 4.7: An example of an image from the TRACE instrument captured with the 171 \AA filter (in negative). The image shows loops in the low corona in contrast to the dark chromosphere. Image downloaded from http://trace.lmsal.com/POD/images/T171_20050908_114211X17.jpg.

study the coronal features from different positions. The angular distance between the spacecrafts in changing (increasing). They achieved 90 degrees separation on January 24, 2009, a condition known as quadrature. This is of interest because mass ejections seen from the side on the limb by one spacecraft can potentially be observed by the in situ particle experiments of the other spacecraft. STEREO are equipped with instruments for tracking radio disturbances (SWAVES), 3D measurements of plasma characteristics (IMPACT, PLASTIC) and the

Sun Earth Connection Coronal and Heliospheric Investigation

(SECCHI) that has four instruments: an extreme ultraviolet imager, two white-light coronagraphs and a heliospheric imager. These instruments study the 3D evolution of coronal mass ejections from birth at the Sun's surface,

through the corona and interplanetary medium, and to their eventual impacts at Earth. The EUV images are acquired at high resolution of 2048×2048 pixels.

Solar Dynamics Observatory (SDO) [dGSF13] is a mission of the NASA launched in February 2010. SDO is designed to help us understand the Sun's influence on Earth and near-Earth space by studying the solar atmosphere on small scales of space and time and in many wavelengths simultaneously. The SDO is equipped with the following instruments:

Helioseismic and Magnetic Imager (HMI) [dSSG10] is designed to study oscillations and the magnetic field at the solar surface, or photosphere. HMI provides four main types of data: dopplergrams (maps of solar surface velocity), continuum filtergrams (broad-wavelength photographs of the solar photosphere), and both line-of-sight and vector magnetograms (maps of the photospheric magnetic field).

Atmospheric Imaging Assembly (AIA) [dLHM13, dWik13b] is designed to provide an unprecedented view of the solar corona in extreme ultraviolet, taking images that span at least 1.3 solar diameters in multiple wavelengths nearly simultaneously, at a resolution of about 1 arcsec and at a cadence of 10 seconds or better. Its primary goal together with other instruments on SDO to improve the understanding of the physics behind the activity displayed by the Sun's atmosphere, which drives space weather in the heliosphere and in planetary environments. The wavelength bands and their description are listed in Table 4.2. Images from SDO AIA can be found in Figure 2.1 on page 6 and in Figures 4.8 and 4.9. The AIA provides images in high resolution of 4096×4096 , which enables even research of local movements of the photospheric or coronal structures [aKoD13].

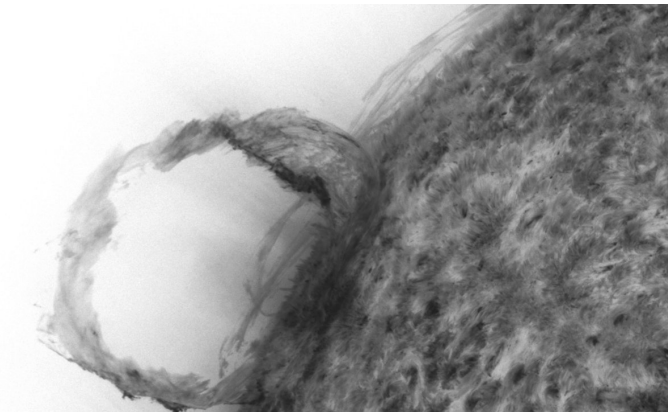


Figure 4.8: A section of one of the first images taken by SDO AIA on March 30, 2010 showing a wavelength band that is centered around 304 \AA . This extreme ultraviolet emission line is from He II, and corresponds to a temperature of approx. 50 000 K. Image downloaded from [dWik10] shown in negative.

4.3 IMAGES FROM COSMIC PROBES

AIA Wavelength Channel	Source	Region of solar atmosphere	Characteristic Temperature
White Light	continuum	Photosphere	5000 K
170 nm	continuum	Temperature minimum, photosphere	5 000 K
30.4 nm	He II	Chromosphere & transition region	50 000 K
160 nm	C IV + continuum	Transition region & upper photosphere	10^5 & 5 000 K
17.1 nm	Fe IX	Quiet corona, upper transition region	$6.3 \cdot 10^5$ K
19.3 nm	Fe XII, XXIV	Corona & hot flare plasma	$1.2 \cdot 10^6$ K & $2 \cdot 10^7$ K
21.1 nm	Fe XIV	Active region corona	$2 \cdot 10^6$ K
33.5 nm	Fe XVI	Active region corona	$2.5 \cdot 10^6$ K
9.4 nm	Fe XVIII	Flaring regions	$6.3 \cdot 10^6$ K
13.1 nm	Fe VIII, XX, XXIII	Flaring regions	$4 \cdot 10^5$ K, 10^7 K & $1.6 \cdot 10^7$ K

Table 4.2: AIA wavelength bands. Taken from [dWik13b].

Extreme Ultraviolet Variability Experiment (EVE) measures the solar extreme ultraviolet (EUV) spectral irradiance to understand variations on the time-scales which influence Earth’s climate and near-Earth space in high spectral resolution.

Project for Onboard Autonomy (Proba) 2 [dROB14] is an ESA micro-satellite launched on November 2, 2009. It carries two solar instruments:

Large Yield Radiometer, formerly Lyman alpha Radiometer (LYRA) is an ultraviolet irradiance radiometer that observes the Sun in four passbands, chosen for their relevance to solar physics, aeronomy and space weather. This instrument can also detect flares and analyze the atmospheric composition of the Earth.

Sun Watcher using Active Pixel System detector and Image Processing (SWAP) is a small EUV telescope that images the solar corona with a band-pass around 17.4 nm (Fe X), corresponding to a temperature of about 1 MK. SWAP continues the systematic CME watch program of EIT at an improved cadence and monitors events in the lower solar corona that might be relevant for space weather.

4.3.2 Processing images from cosmic probes

Images from most instruments are available calibrated - FITS level 1 or higher. Some of the calibrations do not follow the method described in Section 4.1.2, therefore the images are not only measurements of light intensity, some other processing is done to eliminate instrumental effects or even the average intensity over a period of time. This is the case of SOHO/LASCO, the specific information can be found in [dUSN12] and the related links.

Images from certain instruments contain a significant amount of impulse noise, which is often a result of high-energy cosmic particles hitting the chip. This has to be filtered out. There are various methods of filtering impulse noise, a balanced solution between speed and quality of the result is a two-pass filter that replaces pixel values which are detected as faulty by the mean (or median) of the values of pixels in its neighborhood which are not detected as faulty.

The next step is structure enhancement. Images of the corona out of the visible part of the spectrum are not that strongly dominated by the brightness gradient and there are some structures visible without further structure enhancement. Still there is much to be enhanced as it is illustrated in Figure 4.9. Images of the solar disk often differ in the center and at the limb, there are also local changes in brightness. As a result, methods that are suitable for structure enhancement on the solar disk are not that good for the corona out of the disk due to the extreme brightness gradient in the inner corona and vice versa. See the comparison of the NAFE and FNRGF filters in Figure 4.9. For structure enhancement on the solar disk, classical types of high-pass filters based on convolution can be used. The convolution kernel only has to be modified on the limb if pixels out of the disk should not be taken into account. The recently published Noise Adaptive Fuzzy Equalization (NAFE) [cDru13], which is based on adaptive histogram equalization, reveals the structure in the innermost corona (both on the solar disk and out of it) in an unprecedented way. Section 5.4 is devoted to the NAFE method.

Since its publication in 2006, the Normalizing-radial-graded filter (NRGF) (see Section 5.3 below) has become a standard tool for processing images from LASCO coronagraphs. The Fourier normalizing-radial-graded filter (FNRGF, Chapter 6) is more powerful in enhancing fine structure in coronagraph images as well as images taken in EUV. For comparison of the NRGF and FNRGF on coronagraph data see Figure 6.9 on page 89. These filters are designed for enhancing coronal structures out of the solar disk to cope with the brightness gradient.

In some cases, the very final step may be composing images from more components or in different wavelengths in one false-color image. This requires transforming the images so that the Sun has the identical center, diameter and orientation in the images. Image registration is not necessary here, since the images already contain all necessary information for the transformation.

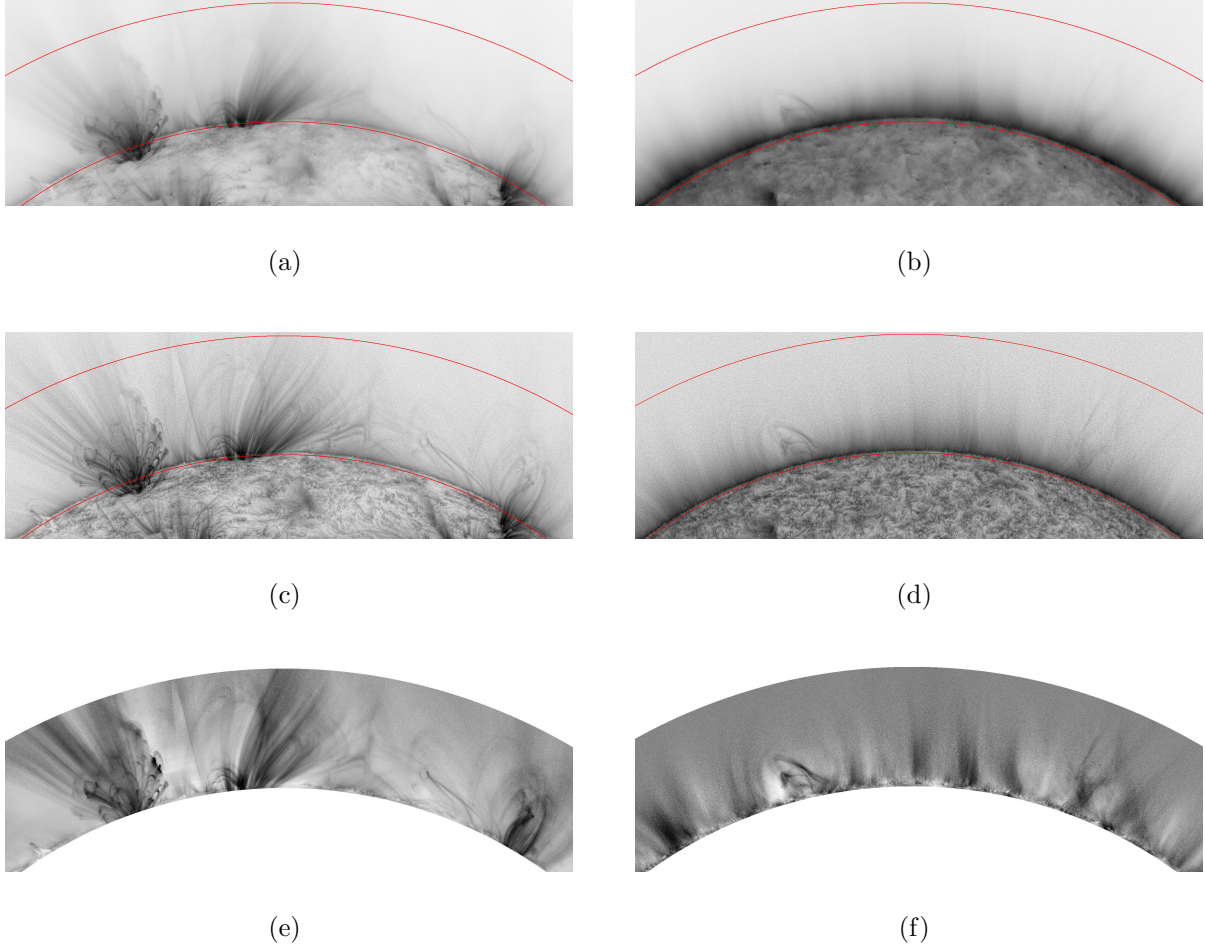


Figure 4.9: Sections of an image from SDO/AIA on 171 \AA acquired at about the time of the total solar eclipse on November 13, 2012. Original images (Figures a, b), processed with the NAFE (Figures c, d), and FNRGF (Figures e, f). The red line in the original and NAFE images limits that part of the image that was processed with the FNRGF. It is clearly visible that the coronal structures are enhanced more and further from the Sun in the FNRGF images due to the fact that the FNRGF was designed for coronal images, whereas the primary target of the NAFE method were the structures on the solar disk. Images are in negative, after contrast expansion. Original data downloaded from [dVso13].

Chapter 5

Earlier filters for solar corona structure enhancement

In this chapter, we will discuss the previous results – previously used filters for processing images of the solar corona. The principles of the filters are taken from the original articles, I added analyzes of their properties and discussions about the advantages and disadvantages of these filters. We will assume that we have an input image suitable for structure enhancement. That is an image that resulted from the process described in Chapter 4. steps are given in [aHDM11, bDrD09, dEsA08].

Since 1980s the computers have enabled a development of computing tools for image processing. At that time, it was not possible to use large neighborhoods for image filtration due to long computing times. As an example, the MaD Max II method introduced by Olga Koutchmy and her colleagues [cKKN88] was using only eight neighboring pixels and with rescaling the image and interpolating it back to the original size also partially the next neighboring pixels. This visualized only small-scale structures, but larger structures like coronal streamers remained hidden.

5.1 Tangential filter

In the late 1990s and 2000s the computing power of computers made it possible to propose and implement filters that work with larger neighborhoods. The method published in 2000 by Espenak [cEsp00] is based on the *Filter / Blur / Radial blur / Spin* procedure in Adobe Photoshop. The input image is blurred by a specified angular range, which means that each pixel in the blurred image is the average of pixels that lie on the same circle with center in the center of the Sun and differ from that pixel in the position angle by less than the specified angle. This means that the filtered image g is a linear combination of the original image f and the blurred mask

$$g(r, \varphi) = K_1 f(r, \varphi) + K_2 \left(f(r, \varphi) - \frac{1}{N_{r, \varphi}} \sum_{\phi \in \langle \varphi - \alpha, \varphi + \alpha \rangle} f(r, \phi) \right),$$

where $N_{r, \varphi}$ is the number of pixels which have the rounded distance from the center of the Sun equal to r and which have the angular coordinate $\phi \in \langle \varphi - \alpha, \varphi + \alpha \rangle$ (φ is the angular coordinate of the pixel to be processed, α is the specified angle by which the image is

5.1 TANGENTIAL FILTER

blurred). This moving-average method was a big step forward in the sense that it enhanced larger-scale structures than previous methods that use only small neighborhoods.

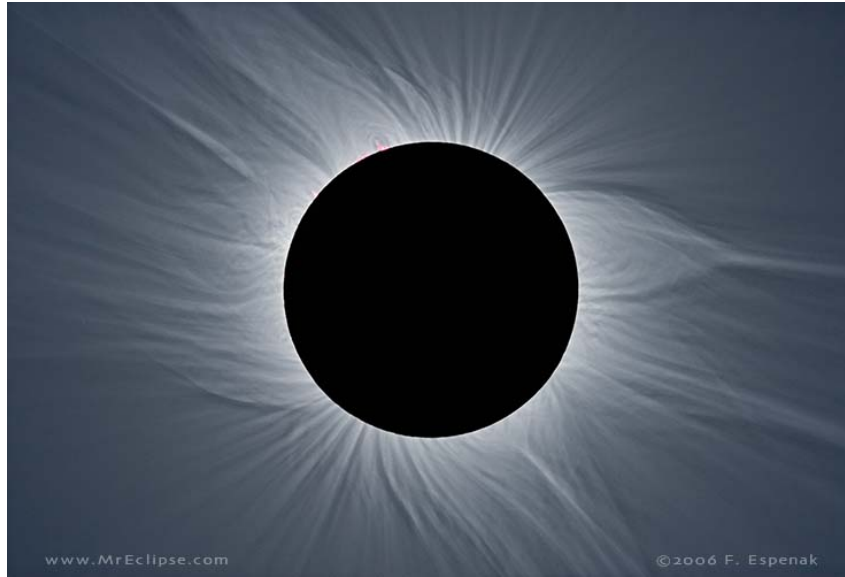


Figure 5.1: Image of the total solar eclipse of March 29, 2006 processed with Espenak's tangential filter. Courtesy of Fred Espenak. Downloaded from [dEsp07].

On the other hand, it had some drawbacks. First, since the filter averages only in the tangential direction (around the Sun), it is direction-dependent. Structures that are oriented radially, such as plumes, are enhanced the most, structures that are oriented tangentially, i.e. parallel with the edge of the Sun (such as tops of loops and helmet streamers), are not enhanced at all. The coronal features are basically visualized field lines of the solar magnetic field. There are both closed loops and ray-like field lines that are open to the heliosphere. The tops of the loops form tangentially oriented structures, which are not visualized by the Espenak filter. The filter gives images that show the most prominent features, but the physical principle how these features are formed is hidden. In some sense, the images are physically incorrect. Figure 5.2 shows the difference between the a tangential filter (Espenak filter) and the method proposed by the Druckmüllers [aDru05, cDRM06, bDru03], the predecessor of ACHF (described in Section 5.2). It is clearly visible that the tops of the loops that are visible in the right image are not present in the left one, which thus lacks physical impact. The tangential filter has been a commonly used technique for solar corona image enhancement. The mathematical models of the solar magnetic field predict the presence of both open and closed field lines of the magnetic field [cRDA10], but the tangential filter enhances only those field lines that are radially oriented, i.e. open to the space. This had been a problem before the ACHF (Section 5.2) was introduced. The idea was that the models were incorrect, because they did not show the reality shown in the Espenak-filtered images. The solution to the problem was that the eclipse images with the Espenak or similar filter applied did not show the reality, they were physically incorrect and the models were correct.

The second drawback of the Espenak filter is its frequency characteristics in the sense of the size of the enhanced structures. Since the filter is effective in one dimension only – tangentially – we can model it on functions of one variable $h(\varphi)$. Convolution in spatial

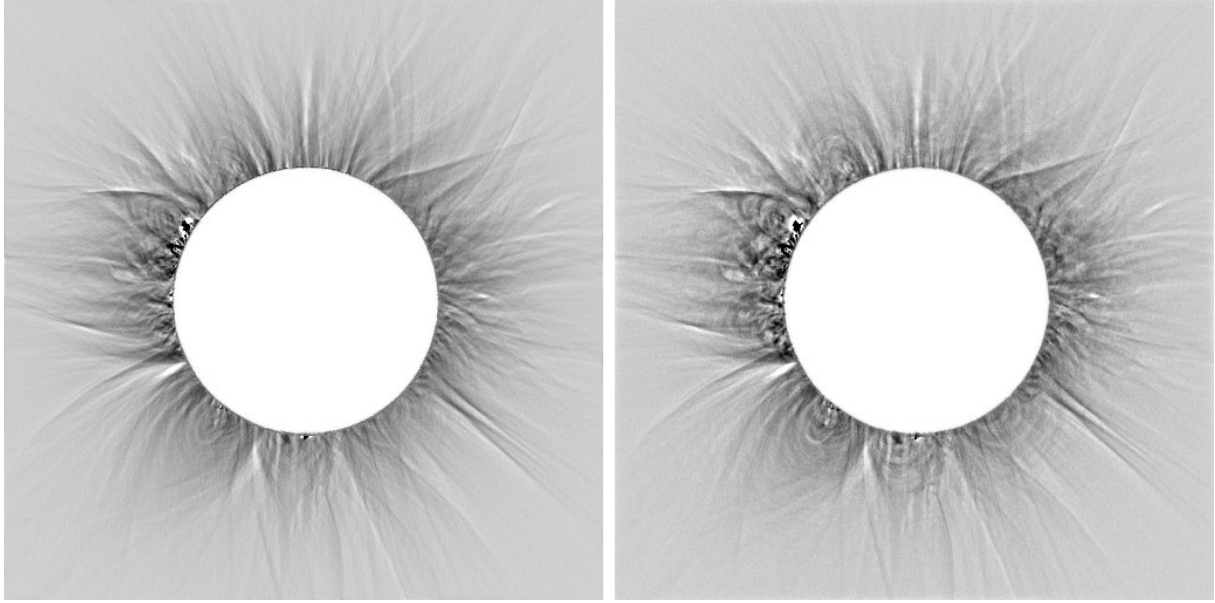


Figure 5.2: Comparison of an image processed by means of a Gaussian tangential filter (left) and by means of adaptive convolution in Corona 1 software [bDru03], a predecessor of the ACHF (right), that correctly enhances all structures in all directions. Taken from [cDRM06]. Images are shown in negative.

domain means multiplication in frequency domain. If a function $h(x)$ is

$$h(x) = \begin{cases} 1 & \text{if } x \in \langle -a, a \rangle, \\ 0 & \text{else} \end{cases}$$

for $a > 0$, its Fourier transform is

$$H(\xi) = a \operatorname{Sinc} a\xi \stackrel{*}{=} \frac{\sin a\xi}{\xi},$$

where $\stackrel{*}{=}$ means *equals almost everywhere* (in this case equals everywhere except for 0). The graph of $H(\xi)$ in Figure 5.3 models the frequency characteristics of this moving-average filter in one dimension. It shows that the frequency characteristics is not monotone with respect to positive frequencies. Some frequencies are enhanced, some attenuated, but it is more complicated than in a correct high-pass filter that enhances information on higher frequencies and attenuates information on lower frequencies (with a transition of many options). This complicated frequency characteristics may create artifacts and therefore images filtered with this filter are not suitable for further scientific interpretation.

The properties of the Espenak filter mentioned above are clear from the Fourier spectrum of the blurring component of the filter (Figure 5.4). The amplitude spectrum shows how the filter is direction-dependent and gives a clue why tops of the loops of the magnetic field lines remain hidden. The shape of the Sinc function is clearly visible in the tangential direction (from top right to bottom left corner). The phase spectrum is very complicated and contains values in the whole range of $\langle 0, 2\pi \rangle$, even though a filter that does not shift structures should have a phase spectrum with all values close to 0.

5.2 ADAPTIVE CONVOLUTION

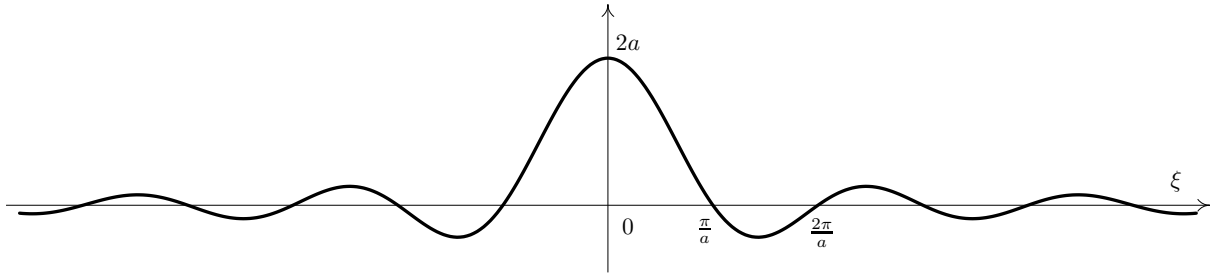
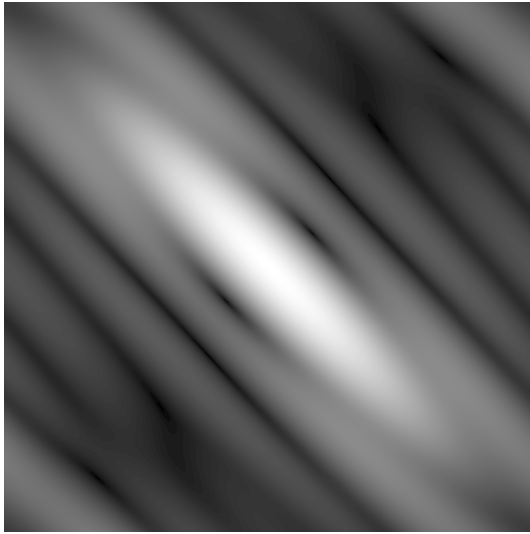
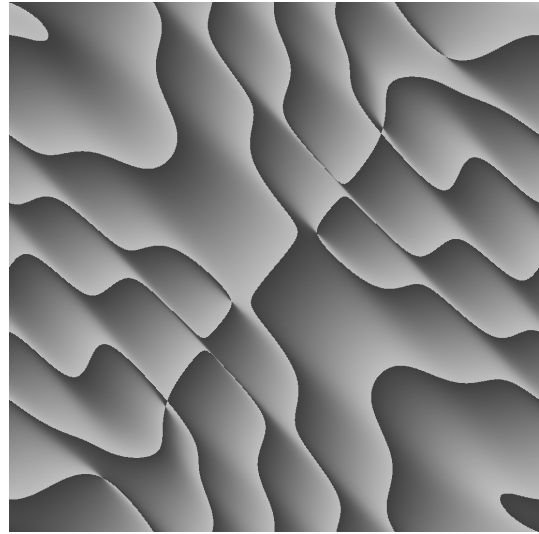


Figure 5.3: Graph of the Fourier transform of function f , which is equal to 1 for all $x \in \langle -a, a \rangle$ and equal to zero out of this interval.



(a) Amplitude spectrum (black – lowest value, white – highest value).



(b) Phase spectrum (black – 0, middle gray – π , white – slightly below 2π).

Figure 5.4: The Fourier spectrum of the blurring component of the Espenak filter for a point at $\frac{7}{8}\pi$ (zero angle is the x -axis). The amplitude spectrum (Figure (a)) shows how the filter is direction-dependent. Structures oriented radially, i.e. from the top left to the bottom right corner are blurred and thus enhanced much more than those oriented tangentially. The phase spectrum (Figure (b)) is very complicated, which implies that some of the coronal structures may be shifted or other artifacts may be produced. As it is described in Section 5.2, the spectrum should be very close to zero for all its pixels.

5.2 Adaptive convolution

As it was stated in [cDRM06], a correct high-pass filter based on convolution with kernel $C(i, j)$ that may be adaptive based on the position of the pixel $[x, y]$ in the image to be processed, the convolution kernel $C_{x,y}(i, j)$ has to have the following properties:

- (a) The Fourier spectrum of the convolution kernel $\mathcal{D}\{C_{x,y}\}$ (\mathcal{D} stands for the discrete Fourier transform – Section 3.2.2) must be real or at least the phase spectrum $\text{Arg } \mathcal{D}\{C_{x,y}\}$ must be very close to zero. This ensures that the filter does not change phase, which might shift structures in the image and bring about artifacts.

- (b) The high-pass filter amplifies high frequencies and attenuates low frequencies, i.e. the amplitude spectrum of the convolution kernel $|\mathcal{D}\{C_{x,y}\}|$ has to be monotone with respect to the distance from the origin (in spatial frequencies). This ensures reduction of the high brightness gradient whilst preserving visibility of coronal features. The amplification is limited by the amount of noise.
- (c) The Fourier spectrum $\mathcal{D}\{C_{x,y}\}$ must be centrally symmetric at least at high spatial frequencies. This ensures that the filter will enhance the visibility of coronal structures irrespective of direction.
- (d) $C_{x,y}(i, j) = 0$ for pixel $[x, y]$ if pixels $[x, y]$ and $[x + i, y + j]$ lie in two significantly different parts of the image (for example the Moon and the solar corona). This ensures adaptivity of the filter. These parts of the image are marked in advance or the decision is made automatically. The criteria are based on a maximal acceptable difference between that pixel values.

These requirements do not define a filter uniquely. There are many parameters and properties of the filter to be decided about. The filter that was implemented in the first version of the Corona software, the predecessor of the current ACHF filter, was partially described in [aDru05]. The kernel used is an approximation of the Gaussian function both in the radial and the tangential direction. First we define a weight function saying if the pixel belongs to the corona and therefore should be taken into consideration for the filtration

$$w(x, y) = \begin{cases} 1 & \text{if pixel } f(x, y) \text{ belongs to the corona,} \\ 0 & \text{if pixel } f(x, y) \text{ else, i.e. belongs to the Moon or is out of the image.} \end{cases}$$

We define this function for every $[x, y] \in \mathbb{Z}^2$ for convenience. Then we define the convolution kernel depending on the position in the image as

$$C_{r,\varphi}(\rho, \phi) = e^{-\frac{(r-\rho)^2 + (r(\varphi-\phi))^2}{2\sigma^2}}, \quad (5.1)$$

where $\sigma > 0$ is a parameter influencing the size of the structures that are enhanced. The bigger is σ the bigger structures are enhanced. The reasonable values of σ vary from 0.5 to 64. Formula (5.1) is a product of a two Gaussian functions, in the radial direction and a Gaussian function in the tangential direction (a general formula for a non-normalized centered Gaussian function is $\exp(-\frac{t^2}{2\sigma^2})$). The Gaussian functions are not normalized, as normalization is performed later in the incomplete convolution in Equation (5.2) (for the definition of incomplete convolution see Section 3.3.2). Finally, the incomplete convolution of the image f with kernel C and weights (for the incompleteness of the convolution) is computed

$$g(r, \varphi) = \begin{cases} f(r, \varphi) & \text{if } w(i, j) = 0, \\ f(r, \varphi) - \frac{\sum_{\rho \in \langle r-2\sigma, r+2\sigma \rangle} \sum_{\phi \in \langle \varphi - \frac{2\sigma}{r}, \varphi + \frac{2\sigma}{r} \rangle} f(r+\rho, \phi+\varphi) C_{r,\varphi}(\rho, \phi) w(r+\rho, \phi+\varphi)}{\sum_{\rho \in \langle r-2\sigma, r+2\sigma \rangle} \sum_{\phi \in \langle \varphi - \frac{2\sigma}{r}, \varphi + \frac{2\sigma}{r} \rangle} C_{r,\varphi}(\rho, \phi) w(r+\rho, \phi+\varphi)} & \text{if } w(i, j) = 1. \end{cases} \quad (5.2)$$

The limits of the sums are chosen so that both Gaussian functions (radial and tangential) almost vanish before they are cut. This is ensured by letting the arguments of the Gaussian

5.3 NORMALIZING-RADIAL-GRADED FILTER

functions go from -2σ to 2σ . The processed image is then a linear combination of the original and the filtered image

$$h(r, \varphi) = K_1 \cdot f(r, \varphi) + K_2 \cdot g(r, \varphi),$$

where K_1, K_2 are non-negative numbers, to keep some information about the absolute brightness of the coronal features.

Condition (a) is fulfilled, since the Fourier transform of a centered Gaussian function is a centered non-normalized Gaussian function [aDru10, cKom01]

$$\mathcal{F} \left\{ \frac{1}{\sigma\sqrt{2\pi}} e^{-\frac{x^2}{2\sigma^2}} \right\} = e^{-\frac{\sigma^2 \xi^2}{2}},$$

which is decreasing for positive arguments, thus condition (b) is fulfilled too. Figure 5.5 shows the Fourier spectrum of the filter to illustrate the precision of fulfillment of conditions (a) and (b). The use of condition (c) is more complicated in this case. The coronal features are radially oriented around the Sun, therefore the shape of the convolution kernel is modified to a part of an annulus. So that the size of the structures that are enhanced with one value of σ is constant through the whole image, the distance measured along a Sun-centered circle is used for the tangential Gaussian function. The kernel is centrally symmetric if considered in modified polar coordinates described in Section 3.1.2, where the angular axis is not angular – it is the distance from point $[s_x + r, s_y + \varphi]$ measured along a circle with radius r centered in the center of the Sun. Last but not least, condition (d) is fulfilled due to the use of function w in Equation (5.2).

The filter described above is still incorporated in the current ACHF filter (software Corona 4.1). A single filter with a particular σ -value enhances mostly coronal structures of a particular size. Therefore, ACHF uses a set of filters with several different values of σ to enhance coronal features from tiny plumes to large-scale streamers. These filters are then combined together. Other improvements are implemented too, e.g. nonlinearity in the use of filtered images. This makes ACHF the best nowadays used structure enhancement technique for images of the solar corona from total solar eclipses in white light, where the noise : signal ratio is much lower than in images taken in spectral lines. The NRGF and later FNRGF methods described in Section 5.3 and Chapter 6 were proposed especially for images in spectral lines and from coronagraphs, which contain much more noise.

Figure 5.6 in an example of application of the ACHF to a white-light observation of the solar corona during a total solar eclipse. Closed loops of the magnetic field lines are enhanced among other structures in the inner corona.

5.3 Normalizing-radial-graded filter

The normalizing-radial-graded filter (NRGF) was introduced by Huw Morgan of the Institute for Astronomy, University of Hawaii in [cMHW06] (currently of Department of Mathematics and Physics, Aberystwyth University, Wales). It solves the problem of the steep radial gradient of image brightness and structure contrast by segmenting the corona into narrow circular regions centered on the center of the Sun, and calculating an average and standard deviation of brightness for each region. Each region is processed separately, which removes the influence of radial brightness decrease. Each pixel is processed according to its height (distance from the photosphere) within the image by subtracting the

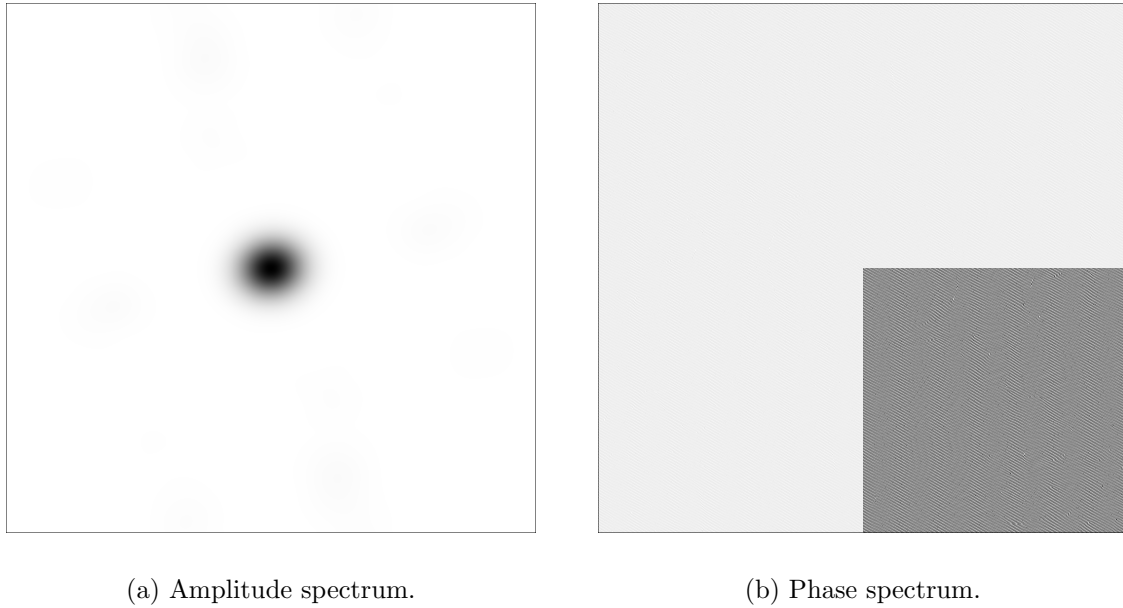


Figure 5.5: The Fourier spectrum in Cartesian coordinates of the adaptive convolution described in this section, both components in negative. The amplitude spectrum shows how the filter enhancement rate is monotone with respect to frequencies. The slight discrepancies are probably caused by clipping at image edges and at 2σ . The phase spectrum has values only values between 0 and 0.27π . Its bottom right quarter has values expanded to the whole dynamic range to show the structure of the phase spectrum. The reasons why the phase spectrum is not a constant zero are in particular rounding errors, the discreteness of pixels and cutting at 2σ .

average (thus removing the steep radial gradient) and dividing by the standard deviation (thus removing the radially decreasing brightness contrast) of values of all pixels in the region.

Let $f(x, y)$ be an image of the solar corona where the pixel values are (with some approximation) proportional to the brightness of the corona at that location. A real image of course contains noise and there are many aspects that cause that the dependence is not completely linear. These include (but are not limited to) vignetting of the lens, diffuse light in the optical system and different brightness of the corona at different times during the eclipse (that side where the photosphere has just been obscured by the Moon is brighter than the side where the photosphere is ‘deeper’ behind the Moon).

Since the NRGF removes the steep radial gradient in images of the solar corona by subtracting the average of f and then dividing by the standard deviation computed along concentric circles around the Sun, the resulting image g is computed as (denotation in accordance with [cLiM83])

$$g(r, \varphi) = \frac{f(r, \varphi) - \overline{f(\rho, \varphi)}|_{\rho=r}}{S(f(\rho, \varphi)|_{\rho=r})} = \frac{f(r, \varphi) - E(r)}{\sqrt{\frac{1}{N_r-1} \sum_{\rho=r} (f(\rho, \varphi) - E(r))^2}}, \quad (5.3)$$

$$\text{with } E(r) = \frac{1}{N_r} \sum_{\rho=r} f(\rho, \varphi),$$

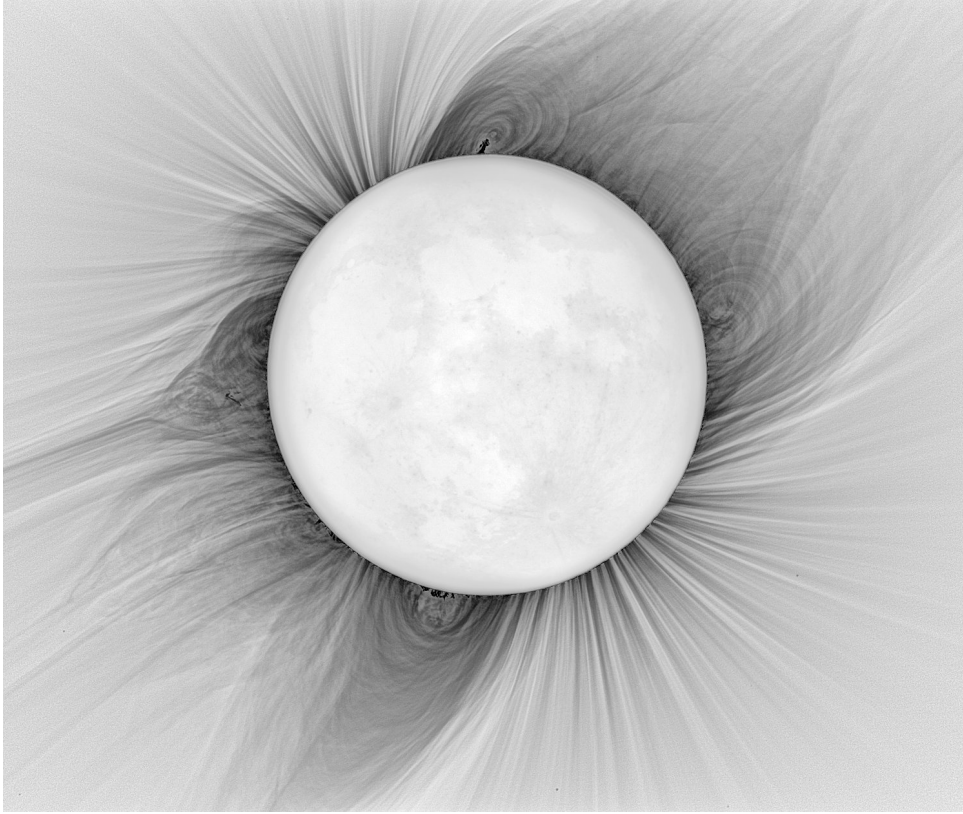


Figure 5.6: An example of an image processed with the ACHF – an image showing the inner corona during the total solar eclipse on August 1, 2008 (in negative). The images used for the creation of this image were taken by Constantinos Emmanoulidis. Image processing by Hana Druckmüllerová and Miloslav Druckmüller [dDru08]. The image is one of the best images showing the inner corona of the Sun in white light.

where N_r denotes the number of pixels in the image that have the rounded distance from the center of the Sun in the image equal to r . If we could assume that the pixel values on each circle had normal distribution, this would mean normalizing the distribution. Formula (5.3) is applied only to circles in the image that lie completely in the corona. An example of an image processed with the NRGF is in Figure 6.11.

This approach applies the same transformation to all pixels in each circle. Therefore, it cannot compensate for a different contrast of structures at the same height. The FNRGF filter described in Chapter 6 is more adaptive in this sense. On the other hand, there are no parameters that need to be set in NRGF. Once the position of the Sun and the size of the obscuring disk (in a coronagraph, or the Moon) are known, the images can be processed completely automatically. This is one of the reasons why the NRGF has become a standard tool for processing coronal images, see for example [aHDM11, cHDM10b], and has aided new insights into coronal structure and evolution [cMoH07, cKTV09] and the connection between the coronal and chromospheric features [cHMT09].

5.4 Noise adaptive fuzzy equalization method

The previous filters in this chapter are designed for structure enhancement in the corona out of the solar disk. The noise adaptive fuzzy equalization (NAFE) method proposed by Druckmüller in [cDru13] and later improved in [aDrD14] is designed for the structures on the solar disk in SDO AIA images. The method is described below. This section is based on [cDru13] and [aDrD14].

The noise adaptive fuzzy equalization method is based on adaptive equalization (see [cPra01] for details) with the modification that the pixels in the neighborhood used for equalization are weighted – the neighborhood is replaced with a fuzzy neighborhood. The method computes a convex combination of a gamma-corrected original image and a filtered image (see the item Gamma on page 98 for more information about the gamma correction).

Let us denote by C a function

$$C : \left\{ \frac{1-n}{2}, \dots, 0, \dots, \frac{n-1}{2} \right\} \times \left\{ \frac{1-n}{2}, \dots, 0, \dots, \frac{n-1}{2} \right\} \rightarrow \langle 0, 1 \rangle, n \in \mathbb{N} \text{ odd}$$

represented usually with a matrix of size $n \times n$ (in analogy with function C in Definition 3.27 on page 26). The fuzzy neighborhood $\tilde{C}_{x,y}^n(i, j)$ is a fuzzy set (fuzzy sets introduced by Zadeh in [cZad65]) with support $N_{x,y}^n$, which is a subset of the domain M of the image $f(x, y)$ and membership function $\mu_{x,y}^n : N_{x,y}^n \rightarrow \langle 0, 1 \rangle$, where the membership grade of pixel $[x + i, y + j]$ to the fuzzy neighborhood is defined as

$$\mu_{x,y}^n(x + i, y + j) = C(i, j).$$

Now let us define the fuzzy histogram of $\tilde{C}_{x,y}^n$ as

$$h_{x,y}^n(t) = \sum_{i=\frac{1-n}{2}}^{\frac{n-1}{2}} \sum_{j=\frac{1-n}{2}}^{\frac{n-1}{2}} C(i, j) \delta(t, f(x + i, y + j)) \quad (5.4)$$

where δ denotes the Kronecker delta. Then we define the cumulative fuzzy histogram

$$H_{x,y}^n(t) = \sum_{m=f_0}^x h_{x,y}^n(m),$$

and the normalized cumulative fuzzy histogram

$$L_{x,y}^n(t) = \frac{H_{x,y}^n(t)}{H_{x,y}^n(f_1)}$$

where f_0 and f_1 are the minimal and maximal pixel values in $N_{x,y}^n$. Finally, we define the fuzzy equalizing function

$$g_{x,y}^n(t) = g_0 + (g_1 - g_0)L_{x,y}^n(y), \quad (5.5)$$

where g_0 and g_1 are the minimal and maximal output pixel values. This function is different for every pixel $[x, y]$ and the output pixel $q(x, y)$ is computed according to the formula

$$q(x, y) = g_{x,y}^n(f(x, y)).$$

5.4 NOISE ADAPTIVE FUZZY EQUALIZATION METHOD

The use of fuzzy neighborhoods solves most of the problems of adaptive equalization – the influence shape of the neighborhood that may cause artifacts. Two problems that still persist are the extreme amplification of additive noise in areas with low contrast, which results in a loss of faint low-contrast details, and loss of contrast on boundaries between areas with significantly different brightness.

I adopted the solution for additive noise in the FNRGF filter, its reasoning can be found in Section 6.1.3. In the case of the NAFE filter, the solution means smoothing the fuzzy equalizing function by a convolution with a Gaussian kernel to define the noise adaptive fuzzy equalizing function (which is used instead of the fuzzy equalizing function)

$$g_{x,y}^n(t) = g_0 + (g_1 - g_0)L_{x,y}^n(t) * G_\sigma(t).$$

The convolution of the normalized cumulative fuzzy histogram with a Gaussian kernel has a significant influence only in the neighborhoods of that pixels which are dominated by noise in which the image has very low contrast. On the other hand, the influence is negligible in the high-contrast parts of the image. The higher is the value of σ , the lower is the amount of noise in the low contrast parts of the filtered image.

A solution to the second problem is described in [aDrD14]. The fuzzy histogram is computed from all pixels in the processed pixel neighborhood regardless of its values. If the position of the processed pixel is near the border of areas A_1 and A_2 with significantly different pixel values, the neighborhood contains pixels from both areas. The fuzzy equalizing function (5.5) in this case is a compromise of optimal pixel value transforms for A_1 and A_2 , which results in a significant decrease of local contrast. The solution is to use for fuzzy histogram computing only pixels that belong to that of areas A_1 or A_2 which the processed pixel belongs to. Therefore, we replace (5.4) with formula

$$h_{x,y}^{n,\epsilon}(t) = \sum_{i=\frac{1-n}{2}}^{\frac{n-1}{2}} \sum_{j=\frac{1-n}{2}}^{\frac{n-1}{2}} C(i,j) \delta(t, f(x+i, y+j)) \Delta_\epsilon(t, f(x+i, y+j)),$$

where

$$\Delta_\epsilon(t, f(x+i, y+j)) = \begin{cases} 1 & \text{if } |t - f(x+i, y+j)| < \epsilon \\ 0 & \text{else.} \end{cases} \quad (5.6)$$

The value of ϵ must be found experimentally. Too small values of ϵ cause image fragmentation into small areas with very high contrast features whose borders do not represent relevant boundaries in the image. Too high values of ϵ will result in identical or nearly identical with images those obtained when applying Equation (5.4). Let us denote the corresponding normalized cumulative fuzzy histogram by $L_{x,y}^{n,\epsilon}(t)$ and the corresponding fuzzy equalizing function by $g_{x,y}^{n,\epsilon}(t)$. The use of this function solves the problem.

Figure 5.7 shows the application of the NAFE method on an SDO AIA image. Faint and subtle details are enhanced in a way that no earlier method was capable of.

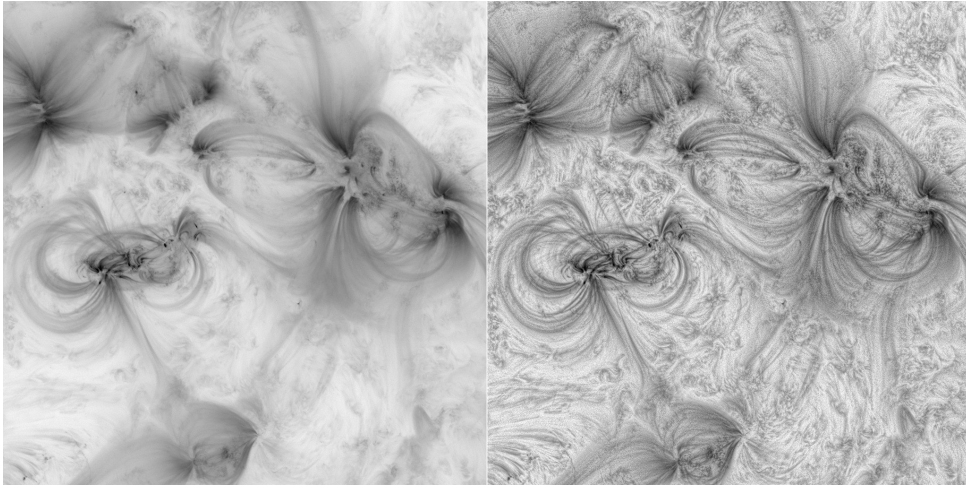


Figure 5.7: An example of an image processed with the NAFE method compared to the original unprocessed image. It is a section of an 171 \AA image acquired by the SDO AIA. Image downloaded from [dDru13] in negative.

Chapter 6

Fourier normalizing-radial-graded filter

This chapter contains the main contribution of the doctoral thesis - the newly developed Fourier normalizing-radial-graded filter (FNRGF).

As it was mentioned in Section 5.3, the disadvantage of the NRGF is that it applies the same transformation to all pixels on each circle. However, there might be both sections with relatively low contrast and fine structures and relatively high contrast and prominent structures on one circle. This is typical for the solar corona in the minimum of the solar cycle, where the polar regions are quiet (darker and with lower contrast) and the active regions with higher brightness and contrast are in a belt of latitudes around the equator (most images of the corona here are from the minimum of the solar activity in years 2006 to 2011). The NRGF does not visualize these fine structures, because their contrast is too low compared to the rest of the circle. The aim of the FNRGF, which was proposed as a part of my Ph.D. study, is to eliminate this drawback – to propose a filter which is inspired by the NRGF (normalizing by subtracting the average and dividing by the standard deviation) offering higher adaptivity. The proposed filter with its principle, with all parameters involved and the results is described in this chapter. The FNRGF was software-implemented in the FNRGF software, whose description can be found in Section 6.3. The section also contains a simple user guide for the FNRGF software. The software can be found on the enclosed CD.

In this chapter, we will assume that we have an image showing the solar corona out of the solar disk with linear dependence of pixel value on corona brightness which is a result of the sequence of steps described in Chapter 4 starting from image acquisition including image calibration, registration and composition in one high-dynamic-range image. This image will be called the original image f and will be indexed both in Cartesian and heliocentric polar coordinates in accordance with Section 3.1.2.

6.1 The principle of the filter

The first version of the FNRGF was proposed and implemented during my study stay at Institute for Astronomy, University of Hawaii in fall 2010 and was first published in [aDMH11]. This chapter is partially based on that article and contains many improvements made since the article was published.

The idea of the filter is, instead of subtracting one number from all values of pixels on one circle and then dividing all of them by the same number, these numbers are computed adaptively, different for different position angles on one circle. The basic principle of filter is described in Section 6.1.1. The filter uses trigonometric polynomials to estimate the local averages and local standard deviations of pixel values. However, after the first implementation, it turned out that the trigonometric polynomials have to be modified – attenuated with increasing order of the Fourier coefficients. The attenuation coefficients used for this purpose, their function and their setting are treated in Section 6.1.2. The noise contained in the processed images has an impact on the filter. The impact and how it can be compensated is discussed in Section 6.1.3.

6.1.1 The basic idea of the filter

The steps of the computation of the filter are enumerated, the same numbering are kept for expressing the process in formulae (below in this section), for explaining how the filter is implemented in Section 6.3.4 and for the user guide in Section 6.3.5.

- (1) **Which pixels are processed?** Only pixels on Sun-centered circles that lie completely in the corona are processed (not partially obscured by the Moon, not partially out of the image). This is a section of M_\odot as defined in Section 3.1.2, let us denote it by M_\odot .
- (2) **Angular and radial segments.** The content of M_\odot is split into one-pixel thick Sun-centered circles and those in tens of non-overlapping angular segments (n_s is the number of segments). Different segments contain generally different number of pixels, because the number of pixels in each segment increases with height r and also the circles are discrete, which means that pixels are not spread evenly in segments on one circle. Figure 6.1a is an illustration of an image being split in segments.
- (3) **Averages, standard deviations, their Fourier approximations.** Two quantities are calculated in each segment – the average pixel value and the standard deviation of pixel values. Thus we obtain two functions of two discrete variables, each of them a function of height r and segment index s . These functions are then approximated with a trigonometric polynomial of order ω . Approximation by the trigonometric polynomial was selected due to its 2π -periodicity. Figure 6.1b gives an idea of this approximation (the attenuation coefficients mentioned there to be described below).
- (4) **Normalization.** Now, the idea of the NRGF is used. The NRGF normalizes the pixel values on each circle in the sense that it subtracts the average of pixel values on whole circles and divides by the standard deviation of pixel values on whole circles. The FNRGF is more adaptive and instead of using averages and standard deviations of whole circles it uses the Fourier approximations described above. Each pixel in the image is processed by subtracting the Fourier approximation of the average and dividing by the Fourier approximation of the standard deviation, at the particular height r and position angle φ of that pixel.
- (5) **Combination with the original image.** Finally, the image filtered with the algorithm described above is combined with the original image to keep some information

6.1 THE PRINCIPLE OF THE FILTER

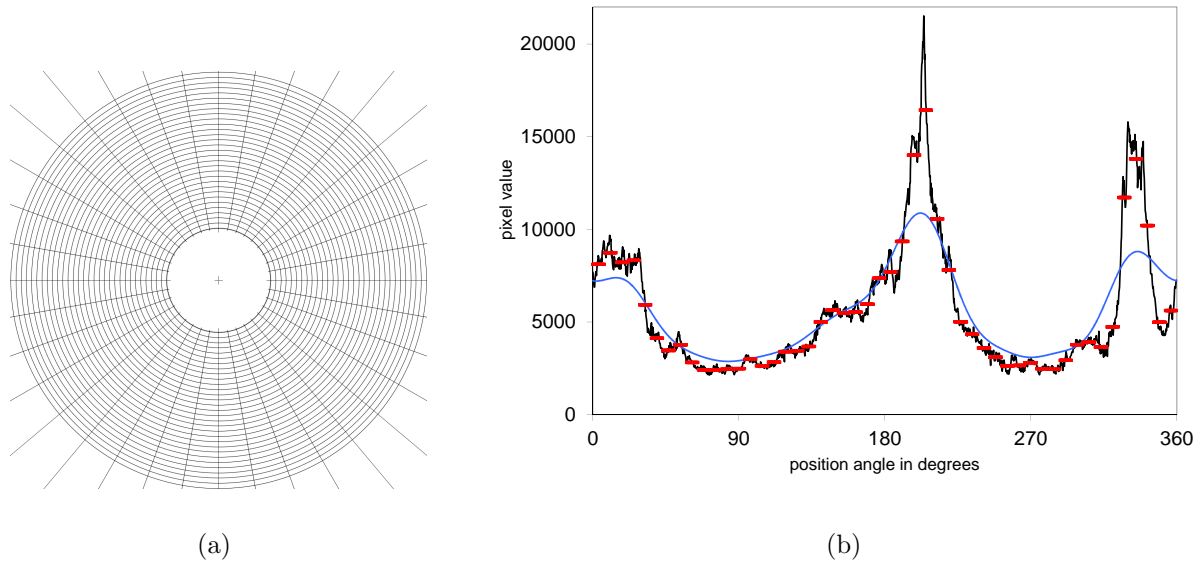


Figure 6.1: Illustration of the computation of the FNRGF. Figure (a) shows an image being split in circles and angular segments. The figure is simplified in the sense that in practice the annuli are only one pixel wide and there are more angular segments. Figure (b) documents the computation. The black line represents original image values, the red bars represent the averages in each of the 50 segments, and the blue line is a Fourier approximation of these averages with a trigonometric polynomial of order $\omega = 10$ with attenuation coefficients set to $A_0 = 1$, $A_1 = 0.9$, $A_2 = 0.8$, ..., $A_{10} = 0$. The attenuation coefficients are discussed in Section 6.1.2. Figure prepared for [aDMH11].

(feeling) about the absolute brightness of the corona in the image (same as in the ACHF – Section 5.2). Pixels that lie out of M_\odot are not processed, they are left black in the resulting image.

The steps above are described more precisely and in the formulae in the steps that follow.

- (1) The set M_\odot is defined in Section 3.1.2. For the computation, we take use a subset of M_\odot , $M_\odot = \{[r, \varphi] \subset M_\odot, r \leq r_o\}$, where r_o is the radius in pixels of the smallest circle that lies completely in the corona.
- (2) The content of M_\odot is split in segments. $s = 0, 1, \dots, n_s - 1$ are indexes of segments, which are evenly spread on each circle, therefore pixels with $\varphi \in \left(\frac{2\pi}{n_s}s, \frac{2\pi}{n_s}(s+1)\right)$ belong to the s th segment. The number of segments n_s must be at least as high as the number of Fourier coefficients involved in the filter, which is $2\omega + 1$. And still the number of segments must be several times lower (it is advised ten times) than the circumference of the smallest circle in the image that lies completely in the corona ($2\pi r_o$) so that the standard deviations of pixel values in the segments are trustworthy numbers. In the radial direction, the segments are indexed with their height r in pixels.

- (3) In this step, the average values and the standard deviations of pixel values in each segment are computed. Let us denote the average of values in segment s at height r by $E_s(r)$. With the denotation inspired by [cLiM83] it can be written as

$$E_s(r) = \overline{f(\rho, \varphi)|_{\rho=r, \varphi \in \langle \frac{2\pi}{n_s}s, \frac{2\pi}{n_s}(s+1) \rangle}} = \frac{1}{N_{r,s}} \sum_{\substack{\rho=r \\ \varphi \in \langle \frac{2\pi}{n_s}s, \frac{2\pi}{n_s}(s+1) \rangle}} f(\rho, \varphi),$$

where $N_{r,s}$ is the number of pixels in the image whose rounded distance from the center of the Sun is equal to r and which belong to the s th segment, the initial version of the filter could be described by the following formulae:

$$a_{r,0} = \frac{2}{n_s} \sum_{s=0}^{n_s-1} E_s(r) \quad (6.1)$$

$$a_{r,k} = \frac{2}{n_s} \sum_{s=0}^{n_s-1} E_s(r) \cos \frac{2\pi k(s + \frac{1}{2})}{n_s}, \quad k = 1, 2, \dots, \omega \quad (6.2)$$

$$b_{r,k} = \frac{2}{n_s} \sum_{s=0}^{n_s-1} E_s(r) \sin \frac{2\pi k(s + \frac{1}{2})}{n_s}, \quad k = 1, 2, \dots, \omega \quad (6.3)$$

Coefficients $a_{r,0}, a_{r,1}, \dots, a_{r,\omega}, b_{r,1}, \dots, b_{r,\omega}$ are coefficients of the trigonometric polynomial of the function given by values of the average pixel value in each segment at each height r . Integrals which would be necessary for the analytical computation of these coefficients (as the scalar product of the base functions $\cos \frac{2\pi k(s + \frac{1}{2})}{n_s}$, $\sin \frac{2\pi k(s + \frac{1}{2})}{n_s}$ and the function itself) are computed numerically by means of the rectangular rule. Coefficients $c_{r,0}, c_{r,1}, \dots, c_{r,\omega}, d_{r,1}, \dots, d_{r,\omega}$ are computed for the standard deviation analogically [cLiM83].

$$\begin{aligned} S_s^2(r) &= S^2 \left(f(\rho, \varphi)|_{\rho=r, \varphi \in \langle \frac{2\pi}{n_s}s, \frac{2\pi}{n_s}(s+1) \rangle} \right) = \\ &= \frac{1}{N_{r,s} - 1} \sum_{\substack{\rho=r \\ \varphi \in \langle \frac{2\pi}{n_s}s, \frac{2\pi}{n_s}(s+1) \rangle}} (f(\rho, \varphi) - E_s(r))^2 = \\ &= \frac{1}{N_{r,s}(N_{r,s} - 1)} \left(N_{r,s} \sum_{\substack{\rho=r \\ \varphi \in \langle \frac{2\pi}{n_s}s, \frac{2\pi}{n_s}(s+1) \rangle}} (f(\rho, \varphi))^2 - \left(\sum_{\substack{\rho=r \\ \varphi \in \langle \frac{2\pi}{n_s}s, \frac{2\pi}{n_s}(s+1) \rangle}} f(\rho, \varphi) \right)^2 \right) \end{aligned} \quad (6.4)$$

6.1 THE PRINCIPLE OF THE FILTER

$$c_{r,0} = \frac{2}{n_s} \sum_{s=0}^{n_s-1} \sqrt{S_s^2(r)} \quad (6.5)$$

$$c_{r,k} = \frac{2}{n_s} \sum_{s=0}^{n_s-1} \sqrt{S_s^2(r)} \cos \frac{2\pi k(s + \frac{1}{2})}{n_s}, \quad k = 1, 2, \dots, \omega \quad (6.6)$$

$$d_{r,k} = \frac{2}{n_s} \sum_{s=0}^{n_s-1} \sqrt{S_s^2(r)} \sin \frac{2\pi k(s + \frac{1}{2})}{n_s}, \quad k = 1, 2, \dots, \omega. \quad (6.7)$$

The Fourier approximations of the mean and the standard deviation in each pixel are computed as

$$F_{\bar{f}}(r, \varphi) = \frac{a_{r,0}}{2} + \sum_{k=1}^{\omega} (a_{r,k} \cos k\varphi + b_{r,k} \sin k\varphi) \quad (6.8)$$

$$F_{S(f)}(r, \varphi) = \frac{c_{r,0}}{2} + \sum_{k=1}^{\omega} (c_{r,k} \cos k\varphi + d_{r,k} \sin k\varphi). \quad (6.9)$$

Note that the sines and cosines in the formulae for $a_{r,0}$, $a_{r,k}$, $b_{r,k}$, $c_{r,0}$, $c_{r,k}$, $d_{r,k}$ (Equations (6.1)-(6.3) and (6.5)-(6.7)) and the sines and cosines in the Fourier approximations (Equations (6.8) and (6.9)) have different arguments. This is correct, because the former refer to values in n_s segments, the values are known only in tens of evenly spread points, whereas the latter refer to angles in the interval $\langle 0, 2\pi \rangle$.

- (4) The filtered image g is computed as

$$g(r, \varphi) = \begin{cases} \frac{f(r, \varphi) - F_{\bar{f}}(r, \varphi)}{F_{S(f)}(r, \varphi)} & \text{if } [r, \varphi] \in M_{\odot} \\ 0 & \text{else.} \end{cases}$$

The formula involves division, but there is no need to treat division by zero. Standard deviations of pixel values in a real image (with noise) are always strictly positive and their Fourier approximations as well (the Fourier approximation cannot be lower than the lowest value in the sequence). Note that setting the number of angular segments $n_s = 1$ (which means that $\omega = 0$) converts the FNRGF into NRGF.

- (5) To preserve some information about the absolute brightness of image f , the filtered image g is then linearly combined with the original image to create image

$$h(x, y) = \begin{cases} h(x, y) = K_1 \cdot f(x, y) + K_2 \cdot g(x, y) & \text{if } [x, y] \in M_{\odot} \\ 0 & \text{else,} \end{cases} \quad (6.10)$$

where $K_1, K_2 > 0$.

6.1.2 Attenuation coefficients

It turned out when the above described filter was implemented that a trigonometric polynomial approximates the pixel values and the local contrast of the original image too well. The filtered image contained only structures of a particular size (not the most

prominent, but also not the finest as e.g. from the ACHF – depending on the order of the trigonometric polynomial ω) and then some deviant pixel values caused by stars or impulse noise, therefore the contrast of the visualized structures was very low. The necessity to treat information on different spatial frequencies in a different manner was inevitable.

This is the reason why I introduced the *attenuation coefficients*—Equations (6.8) and (6.9) were changed to

$$F_{\bar{f}}(r, \varphi) = A_0 \frac{a_0}{2} + \sum_{k=1}^{\omega} A_k (a_{r,k} \cos k\varphi + b_{r,k} \sin k\varphi)$$

$$F_{S(f)}(r, \varphi) = C_0 \frac{c_0}{2} + \sum_{k=1}^{\omega} C_k (c_{r,k} \cos k\varphi + d_{r,k} \sin k\varphi),$$

with attenuation coefficients $A_0, \dots, A_{\omega}, C_0, \dots, C_{\omega} \in \langle 0, 1 \rangle$. The series of A_k and the series of C_k should be non-increasing so that the filter treats information on different spatial frequencies in a monotonous way in a sense similar to condition (b) in Section 5.2 about the ACHF. There are 2ω attenuation coefficients in total involved in the filter.

Figure 6.2 gives an idea of the influence of the order of the trigonometric polynomial by showing images with extreme settings of attenuation coefficients. Figure (a) shows that using a high order of the trigonometric polynomial for standard deviations which is not in accordance with the order of the trigonometric polynomial for the averages gives completely wrong results. Using a high order of the trigonometric polynomial for averages not followed by the standard deviations, on the other hand, is not such a big mistake. It is a good illustration of the properties of the original image and of what the NRGF lacks compared to the FNRGF. There is not only lower brightness in the polar regions of the Sun (in the minimum of the solar cycle when the difference between the polar and equatorial regions is the biggest), but also the contrast of the structures is much lower. Therefore, to enhance structures all around the solar disk, it is necessary to use a trigonometric polynomial (not a constant) to compensate for the different contrast in different parts of the corona. This is very well illustrated in the difference between Figures (b) and (c).

Correct values of attenuation coefficients

The proper setting of the attenuation coefficients depends on the size of the image, on its quality (signal : noise ratio) and the distribution of structures in the image. As for now, these parameters have to be set manually, the FNRGF software only contains a tools for setting more coefficient values together. Examples of suitable settings of the attenuation coefficients can be found in Section 6.2.1.

An illustration of an incorrect (too high) setting of the coefficients can be found in Figure 6.3. If the A_k s are set too high (Figure (a)), it causes artificial brightenings in low-contrast parts of the image. They are false glimmers of the higher-order sine and cosine functions. These may not appear in every image – it depends on the distribution of the structures in the image. Another indicator that the A_k s are set too high is that we are losing contrast in the image, especially on lower spatial frequencies. We are enhancing only the finest details that can be visualized with the FNRGF with one setting of ω , not the full range of structure sizes. Setting C_k s too high (Figure (c)) may have destructive effects on the image. Some structures become strongly enhanced and if the coefficients

6.1 THE PRINCIPLE OF THE FILTER

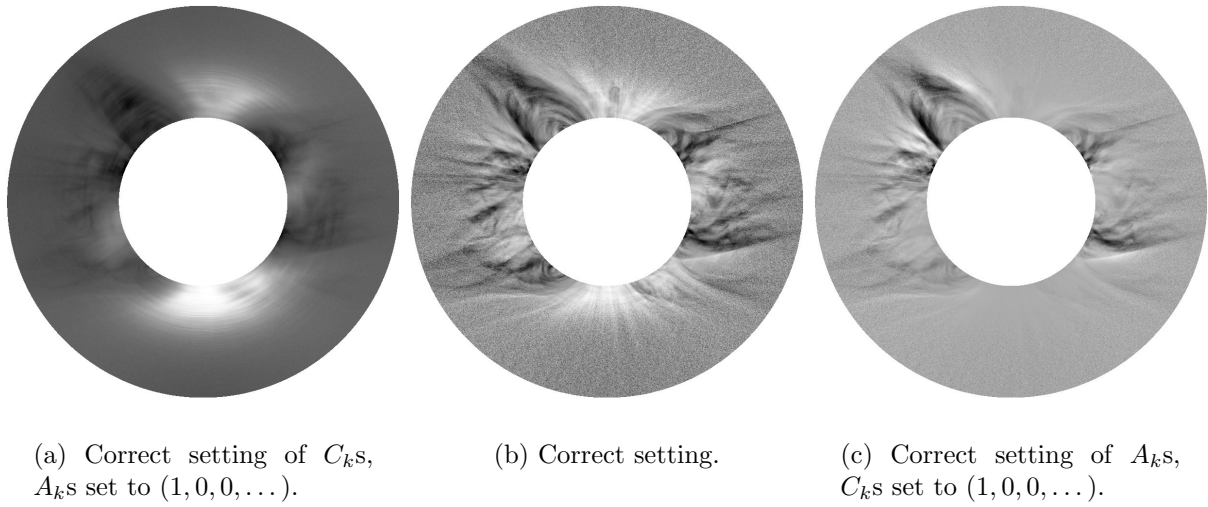


Figure 6.2: A set of images showing the effect of attenuation coefficients on their extreme settings (thus changing the order of the trigonometric polynomial). The middle image has about optimal setting of attenuation coefficients (A_k s set to $(1, 0.97, 0.94, \dots)$, C_k s set to $(1, 0.96, 0.92, \dots)$, $\omega = 50$), whereas the first image has the order of the polynomial for averages set to 0 by the setting attenuation coefficients and the last image has the order for the standard deviations set to 0. The image used is an image of the radiation of the Fe XIV line as observed during the 2010 TSE [aHDM11], in negative.

are enhanced even more, these artifacts will dominate the whole dynamic range of the image (like in Figure 6.2a or even worse depending on the image).

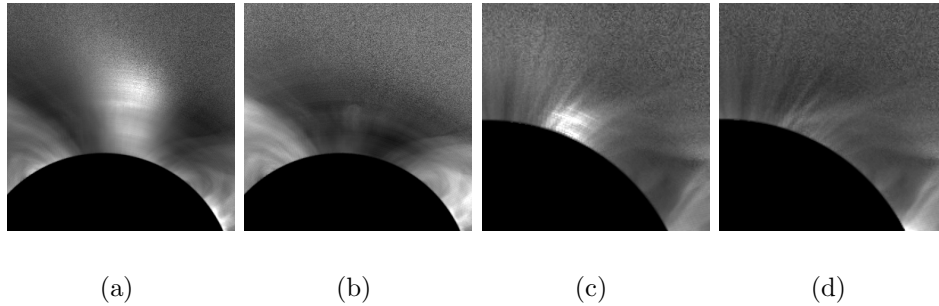


Figure 6.3: Illustration of proper and improper setting of attenuation coefficients, using the 2010 total solar eclipse observations of Fe XIV emission ((a), (b)) and Fe X emission ((c), (d)). The attenuation coefficients for the average are too high in Figure (a), but are close to optimal in (c). Similarly, the parameters for the standard deviation are too high in Figure (b) and are close to optimal in (d). Figure prepared for [aDMH11]

On the other hand, too low values of the coefficients are not as fatal as too high values provided they are low for both A_k, C_k . They only do not make use of the full advantage of the FNRGF, i.e. the structures are not visualized as much as they could. If the coefficients are around the optimum, slight increase of A_k decreases the local contrast, whereas slight increase of C_k increases the local contrast (including noise). The optimal setting of the coefficients seems to have A_k slightly slower decreasing than C_k .

One of the aims of the doctoral thesis as listed in the treatise was enabling the user to let the FNRGF software set the attenuation parameters automatically. However, I must admit that I have not succeeded finding a way how to quantify the quality of the result due to the reasons stated above. I have not found any function of the pixel values that would have a minimum or maximum in the optimal setting. Changing the attenuation coefficients for the average and for the standard deviation have completely different effect on the filtered image. And there are many ways how the coefficients can be set, there are in fact 2ω coefficients that are independent with the only condition that each of the sequences has to be non-increasing. I have experimented with sequences of coefficients that are linearly decreasing from 1 to 0 (if the linear function gives negative values, the coefficients are set to 0). The (sub-)optimal setting of the coefficients depends on the user, who has to set them according to the his / her knowledge so that the structures are enhanced as much as possible (and noise does not dominate over the coronal structures). Finally, the FNRGF software lets the user to set the coefficients arbitrarily with a tool to set them linearly decreasing and a tool to cut the coefficients at one order and set the rest of them to zero.

On the other hand, there is a setting that works for all images and the user obtains better results than using the NRGF without any knowledge about the principles of the FNRGF. Setting $\omega = 30$ and the attenuation coefficients A_k linearly decreasing with step 0.05 and C_k by 0.1 is a setting that always works without producing any artifacts. A human user who has some experience with the FNRGF can surely find a better setting, which leads to images with more detailed structures.

Fourier-analysis explanation for attenuation coefficients

The sense of attenuation coefficients can also be described in the terms of the Fourier analysis. The Fourier coefficients $a_{r,k}$, $b_{r,k}$, $c_{r,k}$, $d_{r,k}$ contain information on different spatial frequencies. The setting of attenuation coefficients attenuates information on the corresponding frequencies – they form a low-pass filter for the unsharp mask, which is used in the high-pass filter (for unsharp mask filtering see the paragraph Unsharp masking in Section 3.3.2 on page 28). In fact, the FNRGF cannot be simply expressed as subtracting an unsharp mask, but we can intuitively use the idea. This can be, in principle, always done in two ways – by multiplication in the frequency domain and by convolution in the spatial domain. Here I chose the first option due to the use of the trigonometric polynomials. Expressing the attenuation by means of convolution can be a tricky task once it is done in the frequency domain. Computing the Fourier transform analytically is in general non-trivial. However, what is necessary, the filtration must be monotone with respect to frequencies, i.e. the sequence of attenuation coefficients must be non-increasing.

First results

Figure 6.4 illustrates the result of application of the FNRGF on an Fe X image taken during the 2010 total solar eclipse as published in [aDMH11] (for more information on these observations see [aHDM11]). Since that time, the FNRGF software was improved, therefore the images in the following sections have higher quality than Figure 6.4. Figure 6.4a shows how the observation is dominated by the steep decrease of brightness - only the very innermost corona can be seen, and there is no appreciable structural detail. The FNRGF-processed image is shown in Figure 6.4b. The latitudinal profiles of the original observation and the filtered image (Figures 6.4c and 6.4d) demonstrate the effect of the

6.1 THE PRINCIPLE OF THE FILTER

FNRGF on the images. After the processing, all circles have identical mean pixel value and identical standard deviation of pixel values. Thus structures further from the Sun are enhanced much more than those close to the disk.

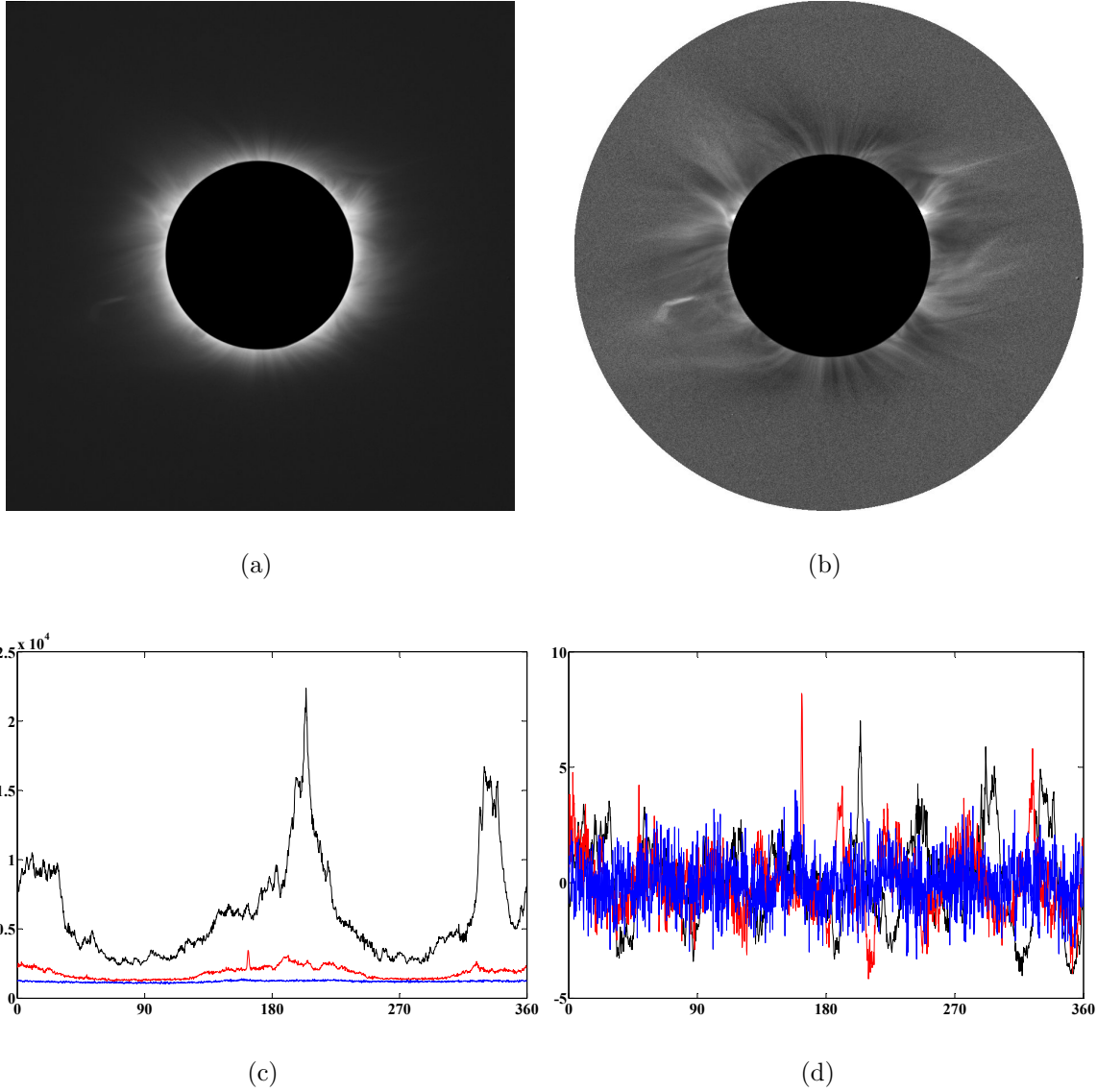


Figure 6.4:

(a) The original image (Fe X emission during the 2010 total solar eclipse) in the logarithmic brightness scale. Details on the equipment can be found in [aHDM11].

(b) Image (a) after the application of the FNRGF.

(c), (d) Latitudinal profiles of Figures (a) and (b) at heights of 1.3 (black), 1.6 (red) and 2.2 R_{\odot} (blue). The x -axis is the position angle in degrees, the y -axis is the pixel value (unit irrelevant). Figure prepared for [aDMH11].

Some images processed with the FNRGF contain visible rings (like on a gramophone disk). These are visible for example in Figure 6.3b and partially also in Figure 6.6. They are caused by the fact that there is no connection between the processing of one Sun-centered ring and the neighboring one. Each circle is processed separately. If there is

significant impulse noise in the image (especially more faulty pixels next to each other) or if there is a very high-contrast structure such as a prominence, it affects the trigonometric polynomial for the whole circle. In some cases, the effect can be eliminated by treating the impulse noise or by changing the attenuation coefficients. I tried to eliminate the effect by replacing the value of each trigonometric polynomial in each point by the median of the value in this point and two neighboring points towards the Sun and two points from the Sun. The procedure was computationally slow, because the trigonometric polynomial had to be evaluated five times instead of once (I could not use existing points in general, because the pixels are discrete and I needed information in points with the same position angle and height differing by two or less from the central pixel). However, there was absolutely no difference between an image computed with the standard FNRGF and with medians. The reason is that the radial decrease of brightness and contrast is so steep that the values of the trigonometric polynomials in every point are lower than in the point closer to the Sun by one pixel in height. Finally, I have not found any solution to the problem. I only have an idea that a globally defined function instead of separate functions in separate circles will help. This would be a completely different approach and I do not know what the functions should look like and how they would be fitted to the data (not only due to the enormous and unknown decrease of).

The profiles in Figure 6.4d show that with increasing height the image is more dominated with noise. This is a general problem of solar corona images, the signal : noise ratio decreases steeply with height. The next section brings a solution to this problem integrated in the FNRGF.

6.1.3 Influence of additive noise

Every image produced from frames acquired with a camera (i.e. not computer graphics) contains additive noise, its amount depends on the temperature, lighting of the scene, on the camera sensor and in the case of images composed from more images also on the number of images used. If the image is composed from images with different exposure settings, the amount of noise in different parts of the image is different. In TSE images of the solar corona, most of the noise comes from the noise in the eclipse images, much less from calibration images, because it is possible to take many calibration images after the totality to reduce the noise in the calibration data.

The noise in the image increases the standard deviation of pixel values that is computed as a part of the FNRGF computation. Each image f can be written as a sum of an ideal noiseless image i and the noise n , $f(x, y) = i(x, y) + n(x, y)$. If we consider i and n as two random variables, the mean of f is $\mathbb{E}f = \mathbb{E}i + \mathbb{E}n$ (both for the whole image and locally). If the noise has normal distribution with zero mean (a standard assumption), the mean of f equals to the mean of i and we can conclude that the mean of f is not affected by the noise (in the ideal, asymptotic case).

If we further assume that i and n are independent, the variance of f is the sum of variances of i and n , $\mathbb{D}f = \mathbb{D}i + \mathbb{D}n$. The presence of additive noise with a constant variance throughout the image causes a constant increase of the local variance used in the FNRGF. Since the FNRGF divides by the local standard deviation, the division by a higher number causes lower enhancement in the whole image. However, removing the effect of additive noise by subtracting its variance before using the local standard deviation in the FNRGF (as published in [aDMH11]) is a misleading idea. If there is a part in the

6.1 THE PRINCIPLE OF THE FILTER

image that contains only noise, this idea of dividing by the local $\sqrt{\mathbb{D}i}$ instead of $\sqrt{\mathbb{D}f}$ leads to infinite amplification in this part of the image (infinite amplification of noise).

The solution that is implemented in the FNRGF software is inspired by the method used in the NAFE ([cDru13], Section 5.4). The problem is that extreme amplification in low-contrast areas leads to loss of details in these parts of the image (because they will be dominated by noise), in extreme cases the amplified noise has higher contrast than the prominent structures in the inner corona causing the additive noise to set the range of the image pixel values and decrease the contrast of these prominent structures in the filtered image.

The solution is exactly the opposite – adding noise instead of subtracting. Artificial noise that is independent from the image and the image noise, added to the original image adds a constant to the local variances throughout the image and decreases the relative contrast of the original noise. In parts of the image which are dominated by noise, this decreases the amplification, i.e. decreases the influence of the noise. The noise that is added has negligible effect in parts of the image with prominent structures since the structures lead to high local variances. If the noise is added in the image, we need a random generator and a new image matrix in the computer memory to keep both the original image and the image with artificially added noise. A more efficient solution is adding the variance of the artificial noise to the local variances only in the computation of the FNRGF, i.e. Equations (6.5) - (6.7) are changed to

$$c_{r,0} = \frac{2}{n_s} \sum_{s=0}^{n_s-1} \sqrt{S_s^2(r) + V_n} \quad (6.11)$$

$$c_{r,k} = \frac{2}{n_s} \sum_{s=0}^{n_s-1} \sqrt{S_s^2(r) + V_n} \cos \frac{2\pi k(s + \frac{1}{2})}{n_s}, \quad k = 1, 2, \dots, \omega \quad (6.12)$$

$$d_{r,k} = \frac{2}{n_s} \sum_{s=0}^{n_s-1} \sqrt{S_s^2(r) + V_n} \sin \frac{2\pi k(s + \frac{1}{2})}{n_s}, \quad k = 1, 2, \dots, \omega, \quad (6.13)$$

where V_n is the variance of the artificial noise. Decreasing the relative contrast of the original noise and its amplification allows a bigger part of the dynamic range of the filtered image for the contrast of the coronal details thus allowing higher attenuation coefficients and higher enhancement of coronal structures.

The FNRGF software allows the user to set $\sqrt{V_n}$ – the standard deviation of the artificial noise. Experiments with images taken in spectral lines of Fe ions during the 2010 TSE show that optimal values of $\sqrt{V_n}$ are about 10 to 15 percent of the standard deviation of the noise originally contained in the image. This standard deviation is estimated as the median of standard deviations in all radial and angular segments that are close to the outer edge of the processed corona. Pixels in the 10 outermost rings are taken into account. Figure 6.5 shows an example of a histogram of the standard deviation of pixel values in angular and radial segments used for the noise estimation. The number of 10 to 15 percent is in accordance with test made with the NAFE [cDru13] on SDO AIA data. Figure 6.6 illustrates the effect of V_n on the filtered image. The decreasing amount of noise in the filtered image with increasing V_n is clearly visible. Other parameters are identical for all three images.

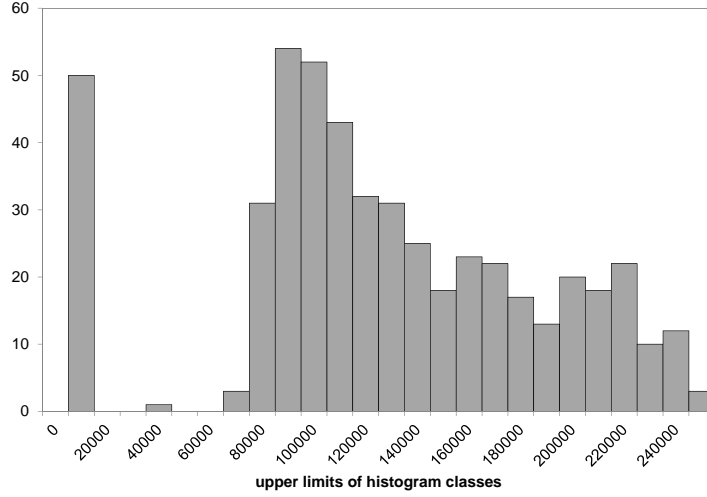


Figure 6.5: An example of a histogram of standard deviations of pixel values in angular and radial segments used for estimation of the standard deviation of noise in the original image. The image used was an image of the Fe XI radiation as observed during the 2010 TSE by the expedition of the Institute for Astronomy, University of Hawaii [aHDM11]. There were 50 angular segments, 10 outermost circles at heights 4.362 to 4.425 R_{\odot} were used.

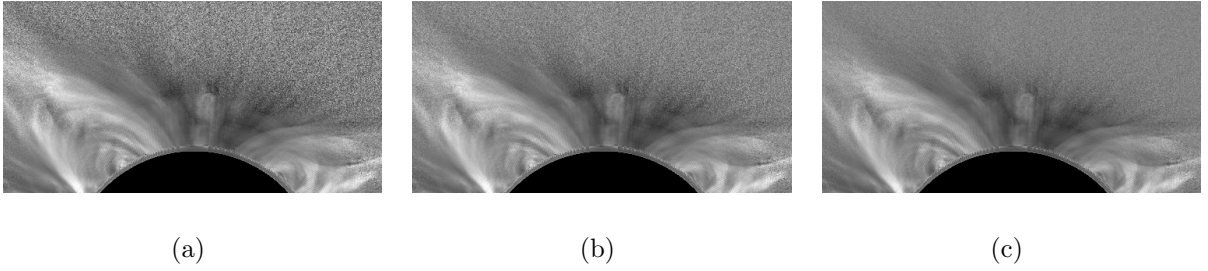


Figure 6.6: Illustration of the effect of artificially added noise in the FNRGF on a section of the Fe XIV image taken during the 2010 TSE. $\sqrt{V_n}$ was set to 0 (a), 7.5 % of the noise in the original image estimated from 2.618 to 2.68 R_{\odot} (b), and 15 % of the noise in the original image (c). The attenuation coefficients A_k were linearly decreasing with a step of 0.03, C_k with a step of 0.04. The filtered image was mixed with the original image in the ratio of 7 : 1 after being both of them normalized to $\langle 0, 1 \rangle$.

6.2 Results

6.2.1 Application to total solar eclipse observations

The FNRGF was originally designed for images of radiation of spectral lines taken during total solar eclipses, which were also its first training data. Figure 6.7 is a complete collection of images of radiation of heavy ions as observed by the team of prof. Habbal during the 2010 TSE. The images were processed with the latest version of the FNRGF software with the highest possible number of segments n_s and the highest possible order of the trigonometric polynomial ω , for most of the images, n_s was set to 100 (101 was the highest possible if we estimate the number of pixels in each of the segments in the smallest circle in the corona to 10 by setting n_s equal to one tenth of the circumference of this

6.2 RESULTS

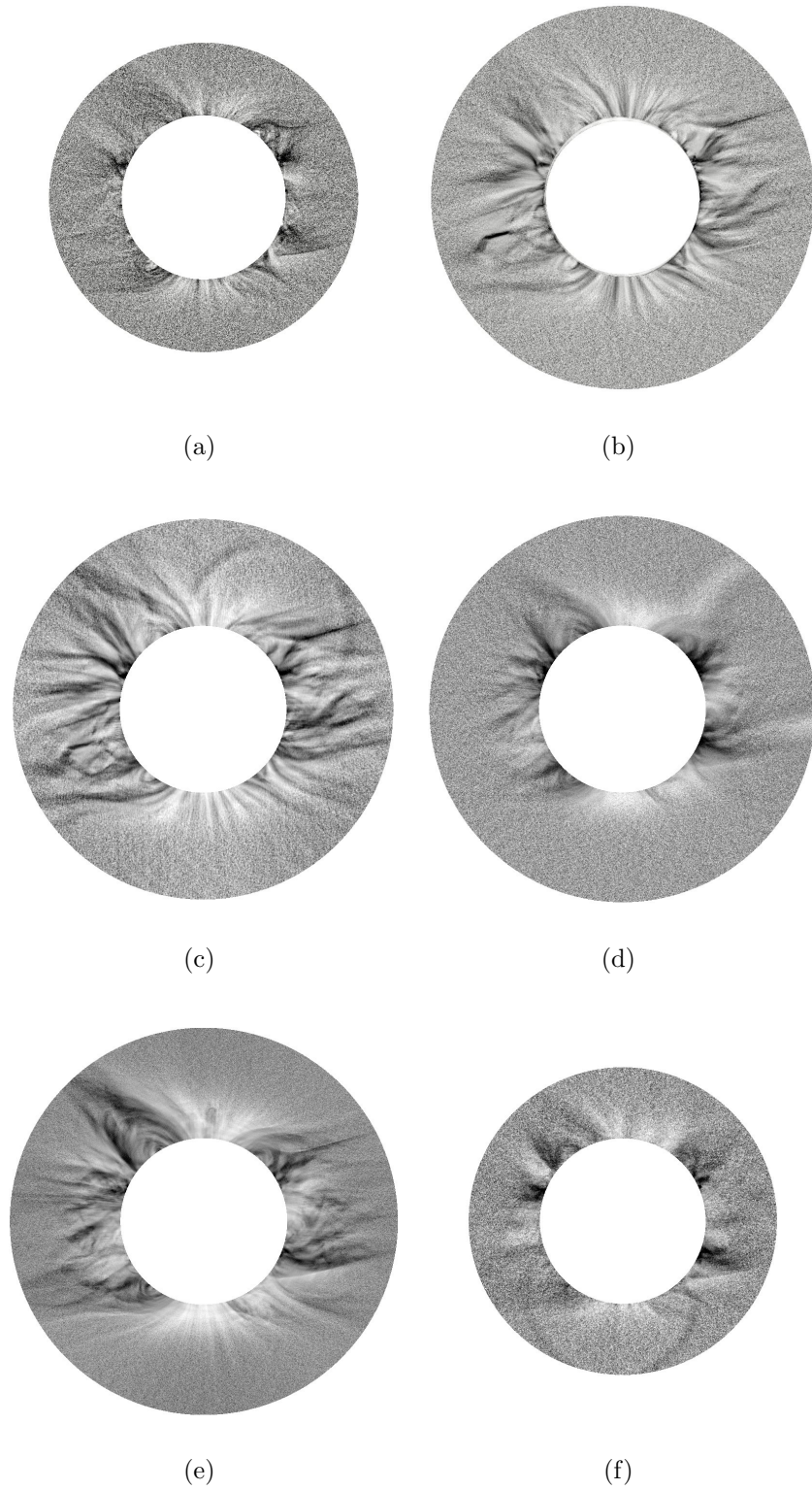


Figure 6.7: A complete set of images of radiation of heavy ions as observed during the 2010 TSE [aHDM11]. (a) Fe IX 435.9 nm, (b) Fe X 637.4 nm, (c) Fe XI 789.2 nm, (d) Fe XIII 1074.7 nm, (e) Fe XIV 530.3 nm, (f) Ni XV 670.2 nm. All images in negative. To compare the results with processing with the NRGF and ACHF see [aHDM11].

circle). For these images, the attenuation coefficients A_k were set to $(1, 0.97, 0.94, \dots)$, the coefficients C_k were $(1, 0.96, 0.92, \dots)$. The images were processed up to the height of $2.5 R_\odot$. The only two images that were processed up to the height of only $2 R_\odot$ are Fe IX and Ni XV (Figures (a) and (f)), which also had lower number of segments (50) and their trigonometric polynomials were attenuated more (A_k s set to $(1, 0.95, 0.90, \dots)$, C_k s to $(1, 0.94, 0.88, \dots)$). These images have lower signal to noise ratio, the Ni XV line is relatively weak, in the case of Fe XIII it is caused by the low quantum efficiency of the camera at this wavelength, only approximately 1.5 percent. That is why the structures in these images cannot be enhanced as strongly as in the rest of the images.

The images are nowadays the best images showing the fine structure of the corona in the spectral lines of heavy ions with radiative component. It is thanks to the high quality of the data and the high adaptivity of the FNRGF and due to higher order terms and the separate processing of each circle, which enables the filter to compensate for the enormous brightness gradient and visualize structures further from the Sun.

For application of the FNRGF to a white-light image from a total solar eclipse see the page 92 – Comparison with the ACHF in Section 6.2.3.

6.2.2 Application to space-based observations

The FNRGF is of course not limited to eclipse images. I show here how the application of this tool significantly improves the depiction of coronal structures in coronagraph and EUV images.

Figure 6.8 shows the application of the FNRGF to an EUV observation from the SOHO EIT. The EUV Imaging Telescope (EIT) aboard the Solar and Heliospheric Observatory (SOHO) (see page 57 for more information) observes the chromosphere and low corona in collisional emission lines of highly ionized iron. The 195 \AA bandpass is dominated by Fe XII at a formation temperature of around 1.5 MK, and in Figure 6.8 I present an image taken in this bandpass about five minutes after the eclipse observations of the team of prof. Habbal during the 2010 TSE. The outer part of the image was processed by means of FNRGF to enhance details in the solar corona. Before applying the filter, impulse noise (for example, faulty pixels, or hits of the sensor by high-energy particles) was filtered out from the original image by means of a one-pass median filter. The image reveals fine-scale structures in the innermost corona, as well as their connections to structures on the solar disk, which were completely invisible in the original image.

Figure 6.9 shows the application of the FNRGF to an observation by the Large Angle and Spectrometric Coronagraph (LASCO) C2 coronagraph (see page 57 for more information) near to the time of the eclipse observations of the team of prof. Habbal during the 2010 TSE. A significant amount of impulse noise was filtered from the image by means of a one-pass median filter before application of the FNRGF and still some impulse noise is visible in the images. Since the FNRGF subtracts the local average of brightness, it enhances structures in darker polar regions, thus revealing polar plumes at all heights within the field of view. These would otherwise remain invisible - even with NRGF processing, which basically enhances the structures with the highest contrast at the given height. Other interesting structural details are revealed in the equatorial streamer region.

Among successful applications of the FNRGF counts also visualization of the comet C/2011 W3 (Lovejoy) in 171 \AA images acquired by the Atmospheric Imaging Assembly aboard the Solar Dynamic Observatory (SDO AIA) (see page 59 for more information)

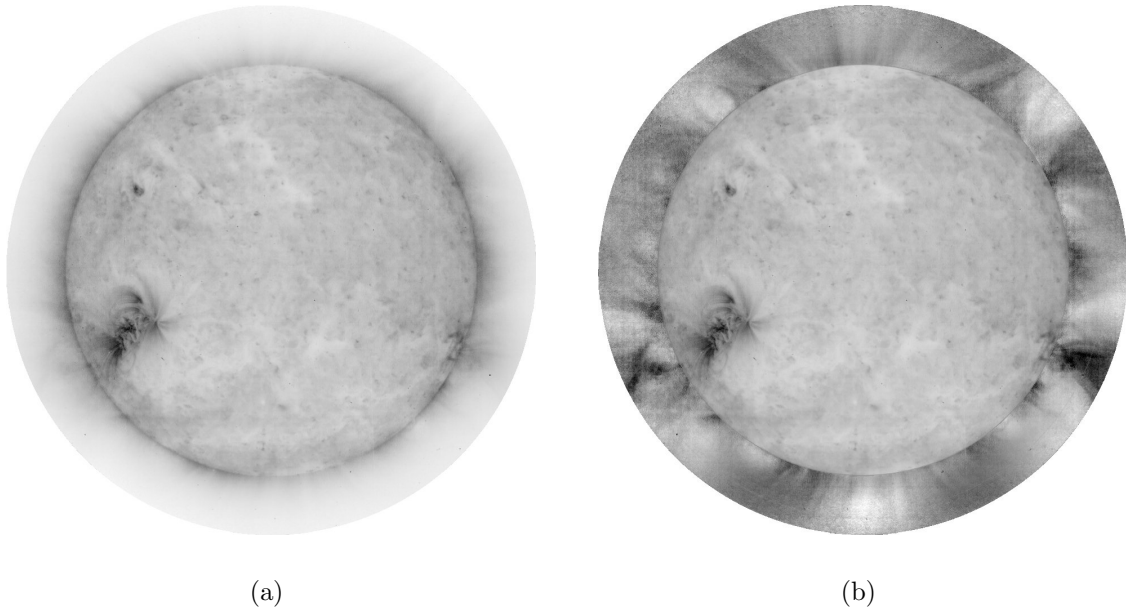


Figure 6.8: (a) A SOHO EIT 195 Å observation taken near to the time of the total solar eclipse observation by the IfA UH team on July 11, 2010. The off-limb field of view is cropped to $1.3 R_{\odot}$. (b) The same image with off-limb regions processed by the FNRGF to enhance structural details. The solar disk is taken from the original image. Figure prepared for [aDMH11], in negative.

shortly after the comet reached perihelion (Figure 6.10). Unfortunately, images of the comet approaching the Sun cannot be processed with the FNRGF, because the field of view of the instrument was shifted so that it was centered to the comet, not to the Sun. The FNRGF can only process pictures, where whole Sun-centered circles in the corona out of the solar disk are in the inside the image, when the field of view was shifted, there was no such circle. Images of the comet leaving the Sun have the standard centering, therefore they can be processed. None of the filters in Chapter 5 was able to visualize the comet and the surrounding corona in a similar way to show the tail of the comet enhancing the field lines of the solar magnetic field. The high adaptivity of a high-order FNRGF allowed the fine details to be visualized. The images are studied by astrophysicists and the results are being prepared for publication.

6.2.3 Comparison with other methods

Comparison with the NRGF

The predecessor of the FNRGF, the Normalizing-radial-graded filter (NRGF) is described in Section 5.3. Compared to the FNRGF, it has only one angular segment – the NRGF processing subtracts the average and applies a constant contrast enhancement along Sun-centered circles. Whilst this is effective in removing the average radial gradient in brightness, it does not offer a way to enhance finer structural details in the tangential (i.e. azimuthal) direction. For example, faint plumes in the coronal holes still appear faint since they are contrast-enhanced alongside the very bright streamers. This deficiency is overcome using the FNRGF, which is adaptive in the tangential direction as well as in the radial direction. For example, plumes appear far more clearly in the FNRGF image

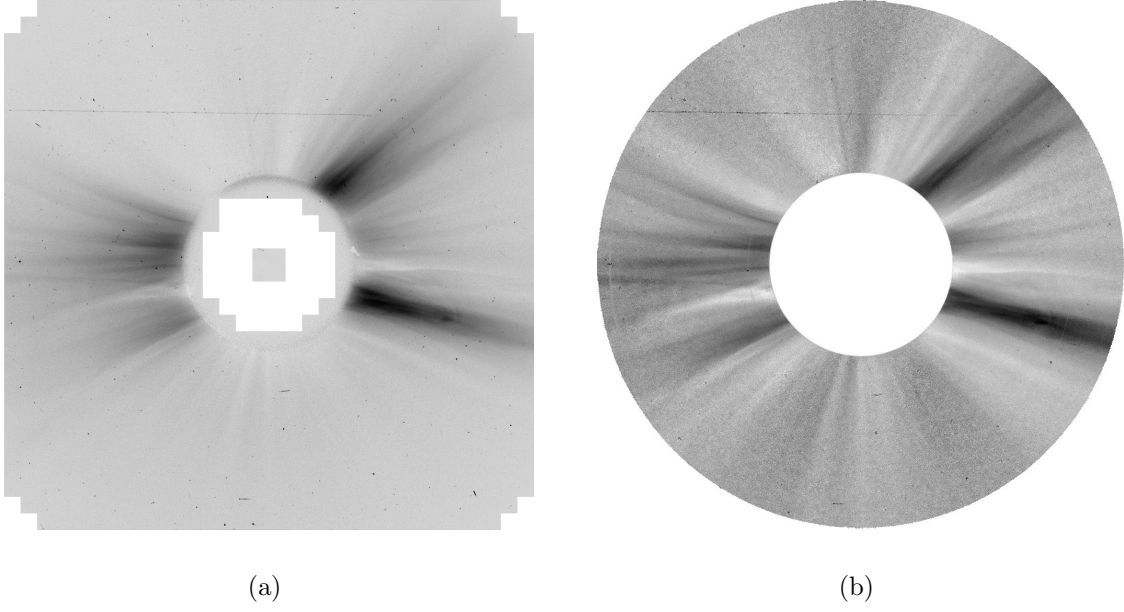


Figure 6.9: a) A LASCO/C2 white light brightness observation taken near to the time of the total solar eclipse on July 11, 2010. The inner limit of the field of view is $\sim 2.2 R_{\odot}$, as dictated by the occulting disk. The outer field of view extends to $\sim 6 R_{\odot}$ at the center of the image edges. (b) The same image processed by the FNRGF to enhance structural details. Regions outside the annulus which was processed are set to white (black in the processed image). Figure prepared for [aDMH11], in negative.

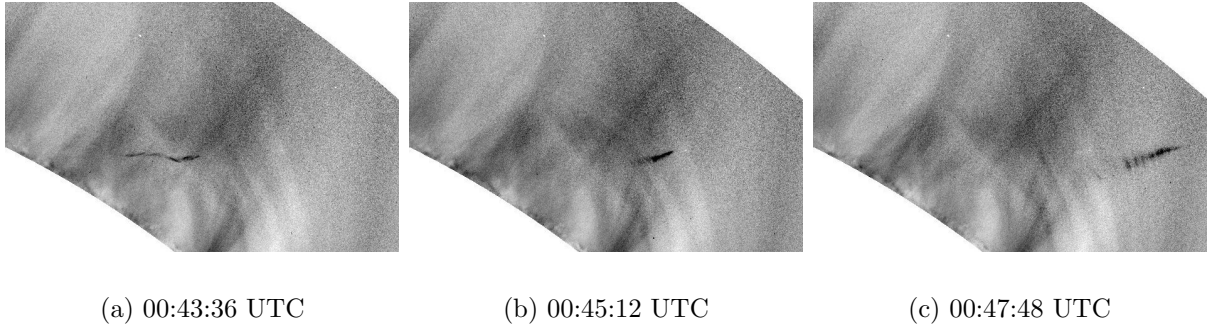


Figure 6.10: A series of images of the comet C/2011 W3 (Lovejoy) shortly after it reached perihelion on 2011-12-16 in 171 \AA images as observed by the SDO AIA. Whole images were processed with the FNRGF, only small sections are shown. Original images downloaded from [dVso13], in negative.

compared to the NRGF. Compared to the NRGF, the FNRGF gives much more detailed images, visualizes finer structures, but on the other hand, it is computationally slower and requires user setting of parameters. The NRGF is automatic and fast.

The FNRGF software enables the user to process images with the NRGF, even though it is an overkill. It requires setting $n_s = 1, \omega = 1, A_0 = C_0 = 1, A_1 = C_1 = 0$. The mathematically logical solution would be $\omega = 0$, but the FNRGF software is built in a way that it needs the trigonometric polynomial at least of order 1 (there is a for cycle for

6.2 RESULTS

k from 1 to ω).

Figure 6.11 compares the application of the NRGF and the FNRGF to the Fe XIV 530.3 nm observation of the team of prof. Habbal of the Institute for Astronomy, University of Hawaii during the 2010 TSE. Figure (a) shows the application of the NRGF, Figure (b) the FNRGF.

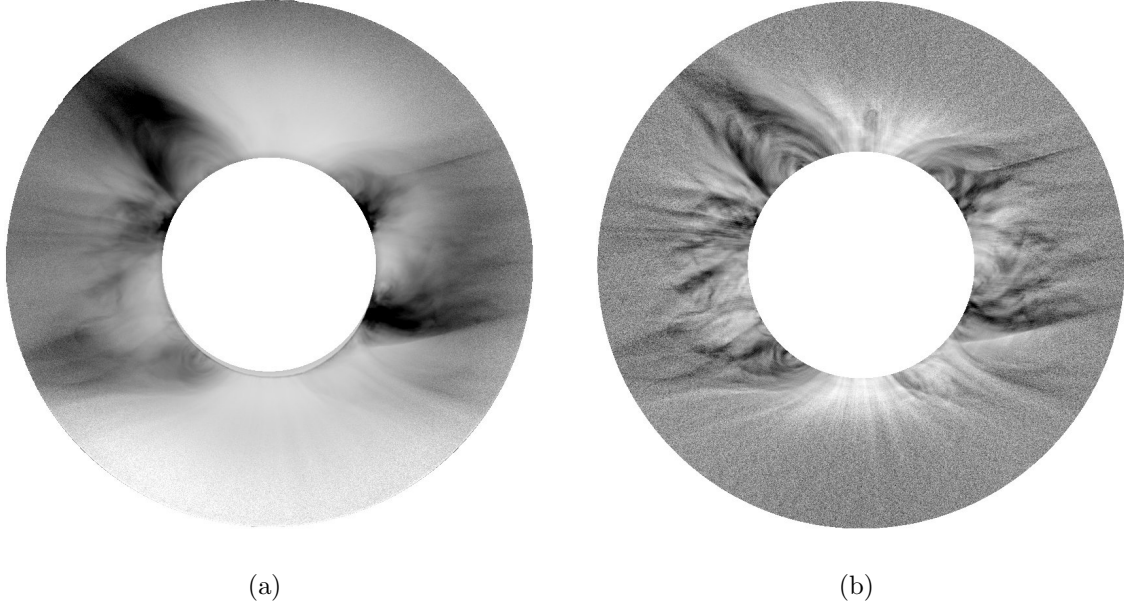


Figure 6.11: The same original image processed by NRGF (a) and FNRGF (b). The original image is an image of Fe XIV emission as observed by the team of prof. Habbal during the 2010 TSE. Figure (a) prepared for [aDMH11], Figure (b) is identical with Figure 6.2b, in negative.

A complete set of observations in lines of heavy ions of the team of prof. Habbal from the 2010 TSE processed with the NRGF can be found in [aHDM11] – compare with Figure 6.7.

Comparison with the ACHF

The Adaptive circular high-pass filter (ACHF) is described in Section 5.2. It has a completely different principle from the FNRGF – it is based on adaptive convolution with several kernels. What can be compared on the principles of the filters is the size of the enhanced structures. Both filters have a method to control the size of the enhanced structures. In the ACHF, it is the parameters of the Gaussian functions used for the kernels, in the FNRGF, it is the order of the trigonometric polynomial and the attenuation coefficients. An important advantage of the ACHF compared to the FNRGF is that it can process the whole image, the FNRGF can only process pixels in M_{\odot} .

A comparison of an image processed with the ACHF and the FNRGF is in Figure 6.12. Even with the highest possible setting of the order of the trigonometric polynomial, the FNRGF cannot enhance as fine details as the ACHF does. The advantage of the FNRGF compared to the ACHF is visualization of details in the corona at higher heights. As the FNRGF processes each circle separately, it is more successful in compensating for the high brightness gradient in the image.

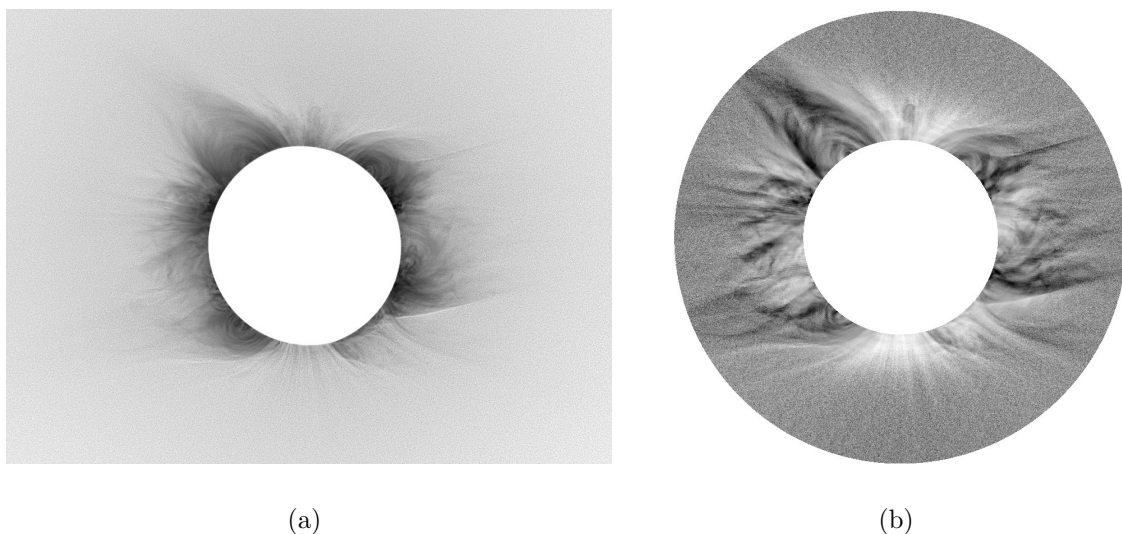


Figure 6.12: The same original image processed by ACHF (a) and FNRGF (b). The original image is an image of Fe XIV emission as observed by the team of prof. Habbal during the 2010 TSE. Figure (a) prepared for [aHDM11], Figure (b) is identical with Figure 6.2b, in negative.

A complete set of observations in lines of heavy ions of the team of prof. Habbal from the 2010 TSE processed with the ACHF can be found in [aHDM11] – compare with Figure 6.7.

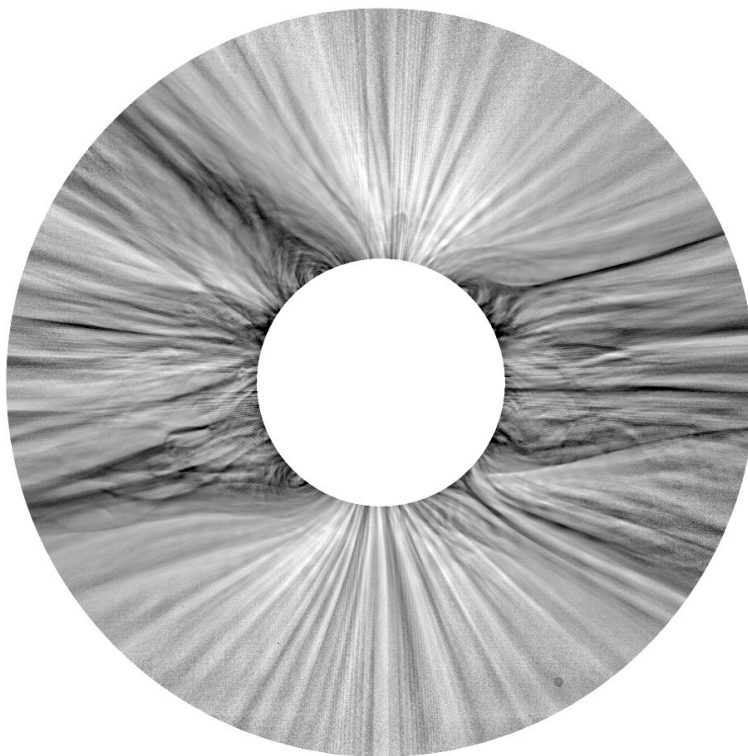
Even though the FNRGF was designed for images with relatively low signal to noise ratio, it can also be used for white-light images. The computation of Figure 6.13 takes only several seconds on current computers with the latest implementation of the FNRGF even though the radius of the largest processed circle was about 900 pixels. This is at least by an order of magnitude faster than enhancement of large-scale structures with the ACHF. However, the FNRGF can never enhance as fine details as the ACHF. It is an option to use the FNRGF for enhancement of the large-scale structures and the ACHF for fine details and then compose the results. Same as in the line images, the advantage of the FNRGF is higher contrast of the enhanced structures further from the Sun.

Comparison with the NAFE

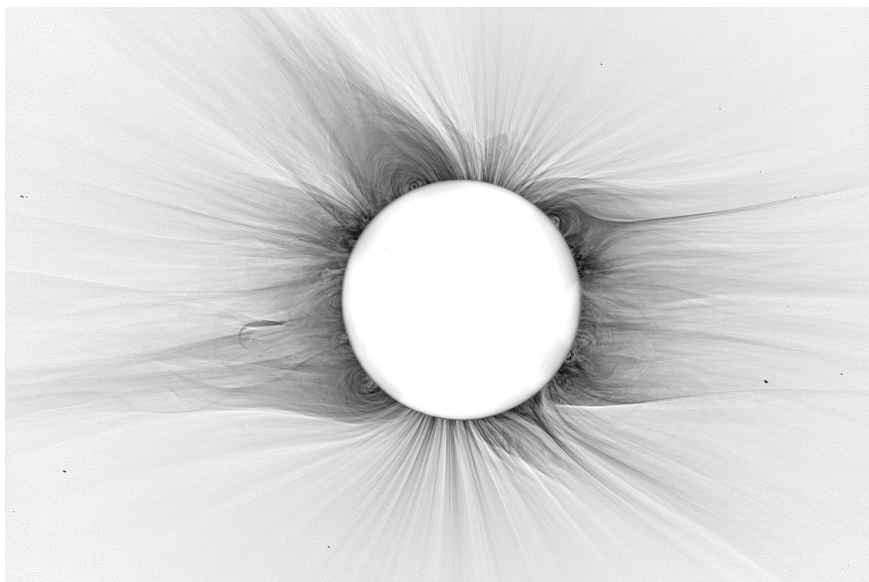
The Noise adaptive fuzzy equalization method (NAFE) is described in Section 5.4. Its target is visualization of the coronal structures on the solar disk, whereas the FNRGF visualizes structures out of the solar disk. The NAFE processes the whole image, even structures out of the solar disk. As the filters have completely different targets, they cannot compete in the visualization of structures out of the solar disk as it is illustrated in Figure 4.9 on page 62.

6.2.4 Other results – graphs of local brightness and contrast

The computation process of the FNRGF gives us an opportunity to study the local brightness and contrast of the image, either using the Fourier coefficients or directly the values of averages and standard deviations of pixel values in angular and radial segments.



(a)



(b)

Figure 6.13: A white-light image of the inner corona as observed during the 2010 TSE by the team of prof. Habbal processed with the FNRGF (a) with 150 angular segments and attenuation coefficients A_k set to $(1, 0.99, 0.98, \dots)$, C_k to $(1, 0.98, 0.96, \dots)$ and with the ACHF (b), both images in negative. Image (b) downloaded from [dDru10].

Figure 6.14 shows the dependence of coefficients a_0 and c_0 on height in an image of radiation of the Fe XI (the processed Fe XI image is in Figure 6.7c). The coefficient a_0 is the average brightness along a circle at one height. It should be similar to the Baumbach-Allen formula (see Section 2.2) and other measurements of the coronal brightness. However, it is very complicated to compare two graphs, taking into account that there is no possibility to use photometric units on the y -axis of the graph, there is no possibility to calibrate it. It also has to be taken into account that the image is an observation of radiation of one spectral line, it does not show the electron density as the Baumbach-Allen formula does. The steep brightness gradient especially in the innermost corona is clearly visible from the graph. The coefficient c_0 is the average standard deviation in each circle, which means ‘average’ local contrast. I have not encountered a graph of the dependence of local contrast on height in the solar corona earlier. As the graph shows, the local contrast decreases with height and the decrease is measurable even at the height of four solar radii. The limit of this function is the standard deviation of noise in the image.

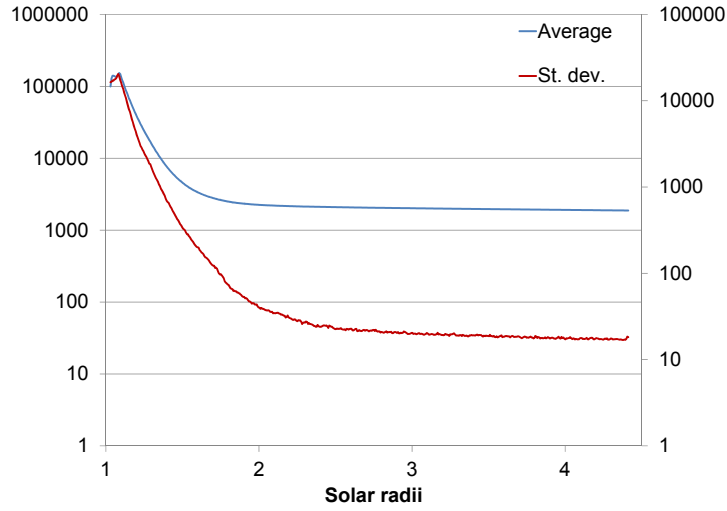


Figure 6.14: Graphs of the Fourier coefficients a_0 (blue) and c_0 (red) as a function of height in the corona in the Fe XI image (Figure 6.7c). The units on the y -axis do not have a physical meaning.

The average pixel values and the standard deviations of pixel values in angular and radial segments give us a tool to study the very local brightness and contrast. Figure 6.15 is a scatter plot of an average pixel value in an angular radial segment vs. the standard deviation of pixel values in that segment as measured in the Fe XI image (Figure 6.7c). As it can be seen, the polar areas have very low brightness and also contrast. The brightest among the studied sections of the corona is the ‘hook’ in the south-east part of the corona, which is a structure that remained in the corona after a passage of a coronal mass ejection [aHDM11]. The center of the hook is the only section in the studied corona where the brightness continues its decrease while the local contrast increases at certain heights.

The FNRGF software allows the user to export the zeroth coefficients of the trigonometric polynomials (a_0, c_0) and average values and standard deviations in segments in simple text files as a function of height. These can be studied with data analysis software and various graphs can be drawn. It is a unique tool to study the photometric properties of the corona in various types of images.

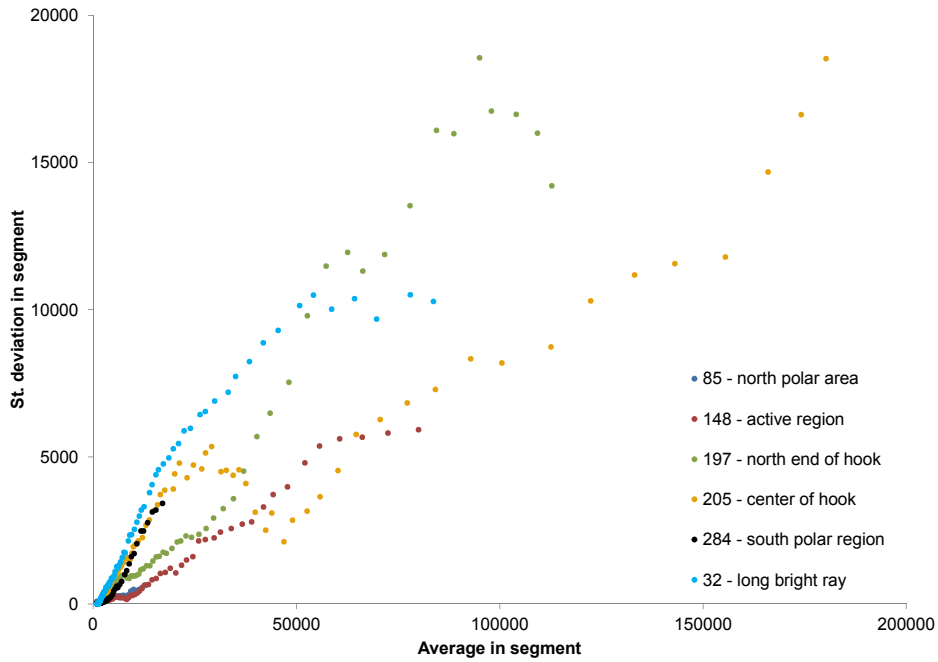


Figure 6.15: Scatter plot of average pixel value in an angular radial segment vs. the standard deviation of pixel values in that segment as measured in the Fe XI image (Figure 6.7c). These values are measured for different position angles (different segment indexes), each position angle marked with a different color.

6.3 Software implementation – FNRGF software

The FNRGF was first implemented in fall 2010 in the FNRGF software in Borland Delphi and later also by Huw Morgan in IDL (a standard scientific programming language used in astronomy, see <http://www.exelisvis.com/ProductsServices/IDL.aspx> for details) as a part of the Solar Software CORIMP package. This has been completely recoded since spring 2013. The new version is much faster, which allowed testing with various parameter setting, which led to further improvements to the software and to the filter, more detailed images showing fainter and smaller structures can be enhanced.

The application can be run in Microsoft Windows operating systems and in Windows emulators (such as Wine for Linux).

This section describes the current implementation. There are many parameters involved in the computation. This section gives an overview of all these parameters and to each of them, it gives the denotation they have in the thesis, in the GUI and in the source code of the software, their minimal and maximal values and any descriptions or comments that might be related to the parameter. Section 6.3.1 contains the parameters of the input file, Section 6.3.2 contains the parameters of the filter itself and finally Section 6.3.3 contains the parameters of image display. Next, the principles of the implementation are discussed in Section 6.3.4 and a brief user guide is provided in Section 6.3.5.

6.3.1 Parameters of the input file

File format: The FNRGF software supports BIF¹ and FITS files. The format is recognized by the file extension and checked by the structure of the file.

Data type of the image matrix in the file: Only word (16 bits per pixel/color component, integer values 0, 1, ..., 65 535) or double (64 bits per pixel/color component, float) data types are supported. All computations with pixel values are performed in double precision. Color images are converted to gray as follows: In the case of BIF files, only the red component is used. For images of ions taken with on-line and off-line filters, the red component contains the calibrated difference of the on-line and off-line component. In the case of FITS files, the red, green, and blue color components are averaged.

Position of the Sun, its radius are given in pixels as floats. The origin of the coordinate system is in the top left corner of the image with the first pixel [0, 0] in accordance with Definition 3.1. (FITS files are indexed from pixel [1, 1], which is in the bottom left corner of the image, the FNRGF software transforms it to the coordinate system of Definition 3.1).

Denotation in the thesis: $O = [o_x, o_y]$, no denotation for solar radius in pixels;

Name in GUI: SunX, SunY, SunR;

Keywords in BIF files: SUN_X, SUN_Y, SUN_R;

Keywords in FITS files: CRPIX1, CRPIX2, R_SUN;

Name in source code: SunX, SunY, SunR.

Position of the obscuring disc, its radius are given in pixels as floats. The obscuring disc is either the Moon (in the case of a total solar eclipse) or the obscuring disk in a coronagraph. If any of these numbers are undefined (e.g. in images in the EUV wavelength range), the corresponding parameter of the Sun is used instead.

Denotation in the thesis: none, the radius of the smallest circle lying completely in the corona is r_o ;

Name in GUI: none, user does not have access to these values;

Keywords in BIF files: MOON_X, MOON_Y, MOON_R;

Keywords in FITS files: not specified, depend on the instrument and telescope.

These are specified under TELESCOP, INSTRUME, DETECTOR keywords.

For details see e.g.

<http://lasco-www.nrl.navy.mil/index.php?p=content/keywords>

Name in source code: MoonX, MoonY, MoonR.

Image width, height:

Denotation in the thesis: w, h ;

¹The BIF file is a very simple non-compressed file format used by the Adaptive Contrast Control (ACC) software and many softwares used in our group for storing eclipse images. It contains a simple case-insensitive header with basic information about the file (width, height, pixel format etc.) followed by the image matrix. The header may also contain any additional information required by any software that uses the files such as the position of the Sun and Moon in the image, coordinates of the observing location and is human-readable like a text file. For more information about the format see the ACC user guide [bDŠD08]. The attached CD contains a simple viewer of BIF files that I made.

Name in GUI: Width, Height;
Keywords in BIF files: WIDTH, HEIGHT;
Keywords in FITS files: NAXIS1, NAXIS2;
Name in source code: ImgWidth, ImgHeight.

6.3.2 Parameters of the FNRGF

At the start of the application, some of the parameters are loaded from the application's ini file (if it exists – if it does not, application default values are used). The names of the parameters in this section in the ini file are listed with the parameters. The ini file is the file Settings.ini in the home directory of the application. Each parameter is saved after one or more spaces after its identifier.

Number of angular segments:

Denotation in the thesis: n_s ;
Name in GUI: Seg.count;
Name in source code: SegmentCount;
Name in ini file: SegmentCount;
Minimal value: 1;
Maximal value: Round($2\pi r_o/10$);
Default value: 130, when image is loaded, the value may be lowered automatically so that the $n_s \leq \text{Round}(2\pi r_o/10)$;

Maximal order of the trigonometric polynomial

Denotation in the thesis: ω ;
Name in GUI: none, displayed in the dialog for attenuation coefficient setting as the maximal index of the attenuation coefficients that can be set;
Name in source code: FourOrder;
Name in ini file: not applicable, is a function of n_s (see below), therefore storing n_s is sufficient;
Value: $(n_s - 1) \text{ div } 2$ – higher order is unacceptable, more Fourier coefficients would be involved than the number of segments, lower order is achieved by setting the attenuation coefficients;

Attenuation coefficients

Denotation in the thesis: $A_k, C_k, k = 0, 1, \dots, \omega$;
Name in GUI: Attenuation coefficients;
Name in source code: Atte;
Name in ini file: $i\text{Attek}$, where $i = 0$ for A_k and $i = 1$ for C_k ;
Minimal value: 0;
Maximal value: 1;
Default values: $(1, 0, 0, 0, \dots)$ both for A_k and C_k ;
Comment: The FNRGF software allows the user to set any values in $\langle 0, 1 \rangle$. $A_0 = C_0 = 1$ is advised. There are automatic tools to set the coefficients linearly decreasing and to set them to zero starting with a specified k .

Standard deviation of artificially added noise

Denotation in the thesis: $\sqrt{V_n}$;
Name in GUI: Add. noise st. dev.;
Name in source code: Noise_AddVar as its variance;
Name in ini file: not saved in the ini file, completely different for different images;
Minimal value: 0;
Maximal value: not limited;
Default value: 0;
Comment: optimal values seem to be 10 – 15 % of the standard deviation of the noise in the original image, see Section 6.1.3 for details;

Ratio which the filtered and original image are combined in (Equation (6.10)):

Denotation in the thesis: K_1, K_2 ;
Name in GUI: 1, Ratio (first normalized, see below);
Name in source code: 1, MixRatio;
Name in ini file: none, Ratio;
Minimal value: 1, must be a positive number;
Maximal value: 1, none;
Default value: 1, 1;
Comment: The FNRGF software first normalizes both the original and the filtered image into the interval $\langle 0, 1 \rangle$ and then computes a linear combination $f(x, y) + K_2g(x, y)$. In those parts of the image where the FNRGF cannot be / is not computed (are not on a circle that lies completely in the corona), the resulting values are set to zero. Lower values of K_2 give a more realistic view of the corona (interior is brighter), but they bring about lower contrast of visualized structures. Common values are 10 or lower;

Lowest height in the corona that is processed can be set by the user in solar radii with 0 in the center of the Sun.

Denotation in the thesis: none;
Name in GUI: InitR;
Name in source code: InitR;
Name in ini file: none, is specific for each image, therefore not save in the ini file;
Minimal value: $\text{Round}(\rho(O, O_M) + r_M)$, where O_M is the center of the occulter (the Moon) and r_M is the radius of the occulter, which is the radius in pixels of the smallest circle in M_\odot divided by SunR.
Maximal value: FinR;
Default value: equal to the minimal value;

Highest height in the corona that is processed can be set by the user in solar radii with 0 in the center of the Sun.

Denotation in the thesis: none;
Name in GUI: FinR;
Name in source code: FinR;
Name in ini file: none, is specific for each image, therefore not save in the ini file;
Minimal value: InitR;

Maximal value: The distance (in solar radii in the image) of the center of the Sun in the image from the closest edge of the image, which is the radius in pixels of the largest circle in M_{\odot} divided by SunR. If invalid pixels in the original image have the pixel value equal to 0, the FNRGF software enables to set FinR automatically to the smallest distance of an invalid pixel from the center of the Sun in the image.

Default value: equal to the maximal value.

6.3.3 Parameters of image display

The parameters listed in this section are not a part of the FNRGF. They are necessary for displaying the processed image. The images are also saved with the current settings of these parameters.

Number of pixels to be underflown is the number of valid pixels whose values are among the lowest and for better image viewing their value is set to zero. For more information about the pixel value transformation for image viewing see the item Gamma.

Denotation in the thesis: none;

Name in GUI: Under;

Name in source code: UnderFlow;

Name in ini file: UnderFlow;

Minimal value: 0;

Maximal value: Half of the number of pixels of the image;

Default value: 0;

Number of pixels to be overflown is the number of pixels whose values are among the highest and for better image viewing their value is set to 255. For more information about the pixel value transformation for image viewing see the item Gamma.

Denotation in the thesis: none;

Name in GUI: Over;

Name in source code: OverFlow;

Name in ini file: OverFlow;

Minimal value: 0;

Maximal value: Half of the number of pixels of the image;

Default value: 0;

Gamma transformation is a standard pixel value transformation that preserves the maximal and minimal pixel value while brightening or darkening the image. For details see page 26 in Section 3.3.

Denotation in the thesis: none;

Name in GUI: Gamma;

Name in source code: Gamma;

Name in ini file: Gamma;

Allowed values: The definition formula allows any positive γ s, but only the following values are available to the user in a combobox: 0.35, 0.4, 0.45, ..., 0.95, 1, 2.2, 3.1, 4. Typical values used for filtered images are about 0.5-0.8, for the original image it is 2.2.

Default value: 1;

Comment: The pixel values of the displayed image are computed as follows:

- Max:=maximal value of the image to be displayed, Min:=minimal value of the image to be displayed (numbers in double precision);
- Compute a histogram of 65 535 classes for the image to be displayed;
- If UnderFlow=0, then MinLevel:=0, else MinLevel is the pixel value (lower bound) corresponding to the lowest histogram class that together with all lower classes contains UnderFlow or more pixels.
- If OverFlow=0, then MaxLevel:=0, else MaxLevel is the pixel value (upper bound) corresponding to the highest histogram class that together with all higher classes contains OverFlow or more pixels.
- GammaTable is a look-up table that contains a conversion from $\{0, 1, \dots, 65\,535\}$ to $\{0, 1, \dots, 255\}$ using a gamma transformation.
- Displayed pixel values (as numbers in $\{0, 1, \dots, 255\}$) are computed as

$$t := \text{GammaTable}^{\lceil \text{Round}((\text{Value} - \text{MinLevel}) / (\text{MaxLevel} - \text{MinLevel}) * 65535) \rceil};$$
where **Value** is the pixel value of the image that is displayed and the **t** is the value of the pixel on the screen.

6.3.4 Principles of the software implementation

Most of the user possibilities to affect the computation and display were listed in the previous sections. In this section, I describe the principles how the computation is implemented. I am not going to go in details, in how the code is organized in procedures, functions and units. I will rather show how the computation is organized and how the data are stored. The key idea is how the computation on circles is effectively done, how the data are organized for the computation. The steps (1) to (5) in this section are identical with steps in Section 6.1.1 – The basic idea of the filter.

Some of the source codes below are not complete or contain different identifiers than in the source code of the FNRGF software to keep this code here as simple and comprehensive as possible. The purpose of the source codes in the thesis is to explain the principle of the implementation.

- (1) Only pixels in M_{\odot} can be processed. All image matrices in the software are rectangular double-precision arrays. I am using one-dimensional dynamic arrays of size `ImgWidth * ImgHeight`, their pixels are addressed with indexes `y*ImgWidth+j`. When the image is re-indexed to polar coordinates, all pixels out of M_{\odot} have `R_cart=0` (see step (2)).

The user can further limit this set by the setting of `InitR` and `FinR`. The computation of the FNRGF (the averages and standard deviations and their Fourier approximations) is performed in a for cycle for r from `Round(InitR*SunR)` to `Round(FinR*SunR)` (`SunR` is defined in Section 6.3.1, `InitR` and `FinR` in Section 6.3.2). This limitation appears in the source code as:

```
if (R_cart^[i]>Round(FinR*SunR)) or (R_cart^[i]<Round(InitR*SunR))
  then Data^.Img^[i]:=0 // used in step (4) and (5)
```

where `Data` refers either to the filtered image or the final image.

- (2) Even for the computation of the FNRGF, the data are not transformed to the heliocentric polar coordinate system, only a system of re-indexing is introduced. It saves memory compared to transforming all image matrices to the polar coordinate system. The auxiliary arrays used for re-indexing are identical for all image arrays and require smaller data formats (single, word or integer). The arrays that are used are

PixelsOnRadius – array of word, for each height it contains the number of pixels on that circle.

Polar2Cart – array of integer, this is the core of re-indexing. It is an array starting with all elements lying on the innermost circle of M_{\odot} , followed by all circles on the next circle etc. ending with elements on the largest circle that lies completely in the image. For each element, the value in the array is the index of that element in the one-dimensional image array (implementing the Cartesian image matrix). Array **PixelsOnRadius** is necessary for orientation in the array.

HeightToIndex – array of integer, for each height (i.e. circle) it says at which element of **Polar2Cart** this height starts.

R_cart, **Phi_cart** – arrays of word, of single, Cartesian arrays, for each pixel $[x, y]$, which is $y \cdot \text{ImgWidth} + x$ in one-dimensional indexing of arrays, the arrays contain the rounded distance from the center of the Sun in pixels (**R_cart**) or the angle of that position angle in degrees (**Phi_cart**) respectively.

The image is never in fact split in angular segments in the sense that the segment index would be stored somewhere. The segment number is computed from the position angle of each pixel by the line

```
seg:=Trunc(Phi_Cart^[Polar2Cart^[HeightToIndex[r]+i]]/360*SegmentCount);
```

- (3) In this step, the average values and standard deviations in each segment are computed and then the Fourier coefficients for both trigonometric polynomials are computed. The Fourier coefficients are stored in one dynamic array **FourCoefArray** consisting of elements of type **TFourCoef** = **array**[**TWhatSeries**,**TAB**,**TWhatOrder**] of **double**. Each element of **FourCoefArray** describes both trigonometric polynomials at one height. **TWhatSeries** is an enumerated type saying if the trigonometric polynomial is for averages (**Ave**) or standard deviations (**Dev**). **TAB** is an enumerated type saying if the coefficients are for $a_{r,k}, c_{r,k}$ (**A**) or $b_{r,k}, d_{r,k}$ (**B**)² as shown in the following table:

	Ave	Dev
A	$a_{r,k}$	$c_{r,k}$
B	$b_{r,k}$	$d_{r,k}$

The value of type **TWhatOrder** is the order k of the Fourier coefficient.

Circles is processed circle-by-circle. The averages and standard deviations in each segment are only used for the evaluation of the Fourier coefficients.³

²This means that elements $b_{r,0}, d_{r,0}$ (which make no sense, are not defined) are stored too, but this is a negligible loss of memory.

³It means that the values of the averages and standard deviations is stored just for the given circle and then replaced in the memory by the values for the next circle.

The effective method of computation of the average and variance (or standard deviation) of a set of values uses the sum of the values and the sum of squares of the values. The used formula can be found on the last line of formula (6.4) on page 77. This is implemented as:

```
for i:=0 to PixelsOnRadius[r]-1 do
begin
  seg:=Trunc(Phi_Cart^[Polar2Cart^[HeightToIndex[r]+i]]/360*SegmentCount);
  //the previous line implements a part of step (2)
  SumX12[Ave,seg]:=SumX12[Ave,seg]+ Image^[Polar2Cart^[HeightToIndex[r]+i]];
  SumX12[Dev,seg]:=SumX12[Dev,seg]+sqr(Image^[Polar2Cart^[HeightToIndex[r]+i]]);
  Inc(N[seg]);
end;
```

Then the sum of values and the sum of squares of values are converted to the averages and standard deviations, the variance of the artificial noise is added:

```
for j:=0 to SegmentCount-1 do
begin
  SumX12[Dev,j]:=sqrt(SumX12[Dev,j]/(SegmentN[j]-1)-(sqr(SumX12[Ave,j])/
    (SegmentN[j]-1)/SegmentN[j])+Noise_AddVar);
  SumX12[Ave,j]:=SumX12[Ave,j]/SegmentN[j];
end;
```

The Fourier coefficients for the averages and standard deviations for the current circle are computed according to formulae (6.1)-(6.3) and (6.11)-(6.13) and the result is stored in the suitable elements of the array **FourCoefArray**.

- (4) The fourth step, normalization, consists of evaluating the attenuated trigonometric polynomial and subtracting the value of the polynomial for the average and then dividing by the value of the polynomial for the standard deviation. In this step, the for cycle over the array is two-dimensional, over the vertical and horizontal coordinate. This is possible by use of the auxiliary arrays **R_cart** and **Phi_cart**, which contain the rounded height and position angle in pixels.

```
for i:=0 to ImgWidth*ImgHeight-1 do
if (R_cart^[i]>Round(FinR*SunR)) or (R_cart^[i]<Round(InitR*SunR))
then MaskData^.Img^[i]:=0 // from step (1)
else
  MaskData^.Img^[i]:=(ImgData^.Img^[i]
    -PointAttenFourier(R_cart^[i]-RoundSunR,Phi_cart^[i]*Pi/180,Ave))/
    PointAttenFourier(R_cart^[i]-RoundSunR,Phi_cart^[i]*Pi/180,Dev);
```

PointAttenFourier is a function which evaluates the attenuated trigonometric polynomial at a specified height and position angle.

- (5) The final step is computing a linear combination of the original image and the filtered image. This is done in a for cycle similar to the cycle in step (4).

6.3.5 FNRGF software user guide

The main window of the FNRGF software is shown in Figure 6.16. The basic steps (image loading, FNRGF parameter setting, processing with the FNRGF, and saving) followed with description of parameter setting, batch processing, and the tools for exporting additional information are described in this section.

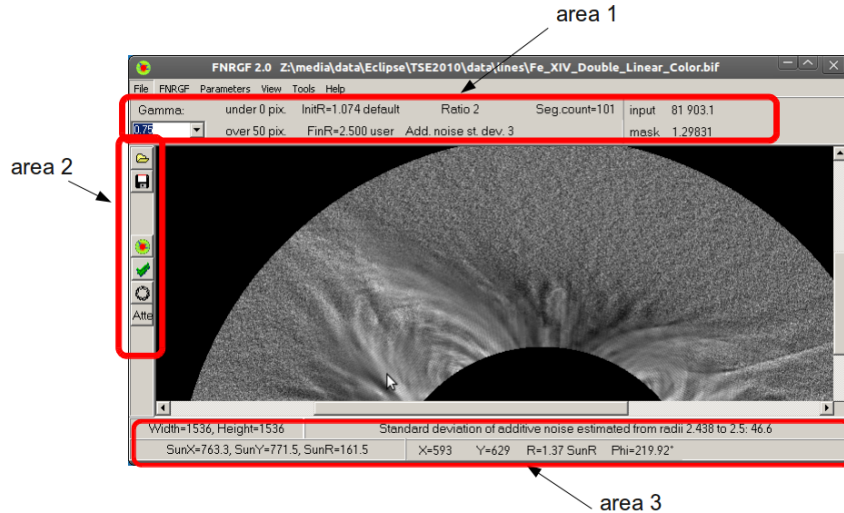

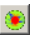



Figure 6.16: A screenshot of the main window of the FNRGF software. The areas 1-3 are referenced in the text for easier orientation.

Basic steps

Image loading. Menu item *File / Open* or button  in area 2. Only BIF and FITS files are supported.

Parameter setting. Optional step. Parameters of the FNRGF and of image display are taken from the previously set values. If the application was just started, then from the ini file. If such file does not exist, then default values are used. For more information about setting these parameters see the paragraph FNRGF parameter setting below.

Processing the image. The image is processed with the FNRGF with all currently set parameters after a click on button  in area 2 or menu item *Tools / Compute FNRGF*.

File saving. The original image, the filtered image or the processed image can be displayed at any time (if these images exist) using the *View* menu. The displayed image (with all display parameters applied) is saved using button  in area 2 or the menu item *File / Save current image*. The available formats are BMP, PNG, and BIF (gray-scale word). If the BIF format is chosen, the header of the file will contain all information about the parameters of the processing and display.


FNRGF parameter setting


The parameters are described in Section 6.3.2. When a parameter is changed, its information panel turns red and its color is changed to the default color when the processed image is recomputed.

InitR (step 1). Set in a dialog that is opened after a click on the *InitR* information panel in area 1 or on menu item *Parameters / Initial Sun R*. When the image file is loaded, the value is automatically set to r_o .

FinR (step 1). Set in a dialog that is opened after a click on the *FinR* information panel in area 1 or on menu item *Parameters / Final Sun R*. When the image file is loaded, the value is automatically set to the radius of the largest circle in the image (in solar radii). There is an option (menu item *FNRGF / Ignore 0 pixel value*) to let the value set automatically to the radius of the largest circle in the corona that does not contain zero values (used as invalid pixels in BIF files).

Segment count (step 2). Set in a dialog that is opened after a click on the *Seg.count* information panel in area 1 or on menu item *FNRGF / Segment count*.

Standard deviation of artificially added noise (step 3). Set in a dialog that is opened after a click on the *Add. noise st. dev.* information panel in area 1 or on Menu item *FNRGF / Add noise – st. deviation*. The standard deviation of the noise in the image can be measured by clicking on button  in area 2 or menu item *Tools / Estimate noise / From outer ring*. The estimation method is described in Section 6.1.3. The estimated value is displayed in area 2.

Attenuation parameters (step 4). Set in a dialog that is opened after a click on button  in area 2 or on menu item *FNRGF / Parameters / Attenuation coefficients*. The table in the dialog has columns numbers 0 to ω . There is an option to set the coefficients linearly decreasing from 1 by a set value for each step and an option to set all coefficients to zero starting from a set order. The setting is done separately for the averages and for the standard deviations.

Ratio original : filtered image (step 5). Set in a dialog that is opened after a click on the *Ratio* information panel in area 1 or on menu item *Ratio orig. : filtered*.


Display parameter setting

The display parameters are the number of pixels that are underflown, i.e. set to black (does not include those set to 0 due to their position closer to the Sun center than InitR or further from the Sun center than FinR), the number of pixels that are overflown, i.e. set to white, and Gamma. Their description can be found in Section 6.3.3. The number of undeflown (overflown) pixels is set in a dialog that is opened after a click on the *under (over)* information panel in area 1 or menu item *View / Settings / Pixels underflown (overflown)*. Gamma is set in a combobox in area 1.

Information panels

The set parameters are displayed in area 1. There are also information panels in areas 1 and 3 displaying information that the user cannot change. Some of them are static (image *Width* and *Height* in area 3 and *SunX*, *SunY*, and *SunR* in area 3), some of them are dynamic and change with the position of the mouse cursor in the image. These are the pixel values of the original image (*input*) and the filtered image (*mask*) in area 1 and Cartesian and heliocentric polar coordinates in area 3. The standard deviation of additive noise estimated from the outer ring of 10 circles is also displayed in area 3 if this number is available.

Batch processing

The FNRGF software has a tool to process images in batch provided that all the images have the same size, same file format and are located in the same directory. Moreover, all parameters of the FNRGF and of display have to be identical. The processed files are saved in the original directory with a suffix specified by the user. The dialog for batch processing can be found in Figure 6.17. It can be activated by clicking on button  in

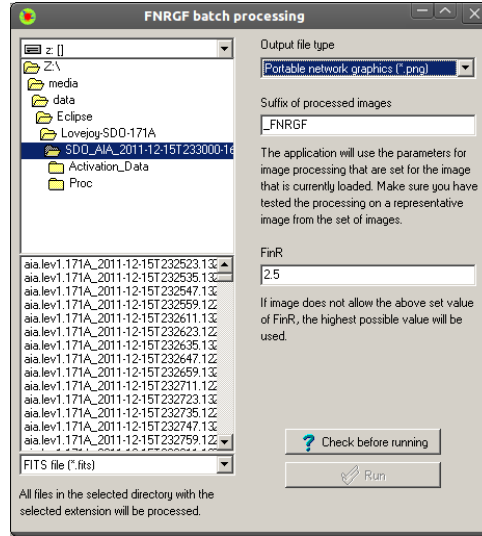


Figure 6.17: A screenshot of the dialog for FNRGF batch processing.

area 2 or the menu item *FNRGF / Batch processing*. All parameters that are not set in the dialog are taken from the application main window. Before running the batch, the user has to press the *Check before running* button to let the application check that all images have the same size. The batch is run after pressing the *Run* button.

Additional tools

The FNRGF application has the following tools for exporting the data for graphical and statistical analysis.

Ring profile. A tool to export the pixel values along one circle at a user-selected height (in solar radii) in a text file. The profile is computed from the currently displayed image (original, filtered, processed) from its double-precision array. The option can be found in menu *Tools* and is active after the FNRGF is computed.

Zeroth Fourier coefficients. A tool to export the coefficients a_0, c_0 for all circles in a text file. It can be found in menu *FNRGF*.

Ave, Dev in segments. A tool to export the values of averages and standard deviations in all segments at all heights in a text file. It can be found in menu *FNRGF*.

Chapter 7

Conclusion

The doctoral thesis *Application of Adaptive Filters in Processing of Solar Corona Images* gives a systematic overview of the solar corona imaging, about processing of acquired images and image structure enhancement. The whole procedure of solar corona imaging in visible and near infrared part of the spectrum during total solar eclipses is described – starting from acquiring a suitable sequence of digital images and calibrating them over registration and composing in one high-dynamic-range image to structure enhancement. The necessary mathematical background is given, all steps of the processing sequence are accompanied with mathematic reasoning. The aim of the thesis was proposing, implementing and testing new filters suitable for images which contain more noise than regular white-light compositions of total solar eclipse images, i.e. images from coronagraphs, from cosmic probes in both visible and shorter-wavelength part of the spectrum and images taken during total solar eclipses in specific spectral lines.

The filter described above was proposed, implemented, and tested on various types of data. Many processed images can be found in the thesis. It is the Fourier-normalizing-radial-graded filter (FNRGF), which is based on the nowadays commonly used Normalizing-radial-graded filter and has much higher adaptivity than this filter. The filter was published in [aDMH11] and after being fully recoded, the implementation was much faster and enabled testing various parameters and improving the filter to enhance even finer details than the original filter. The filter is a numerical method for enhancing coronal structures in images both from total solar eclipses and space-born observations that is based on approximating the local brightness and contrast with attenuated trigonometric polynomials. The filter enables visualization of faint coronal structures in images with relatively low signal to noise ratio while compensation both for the steep decrease of brightness and of contrast in the corona in the radial direction and also for the local changes of these quantities in the azimuthal direction. The processed images of the radiation of heavy ions during the 2010 total solar eclipse are nowadays the most detailed images showing inner corona in spectral lines with a radiative component in the visible wavelength ranges.

The doctoral thesis fulfills most of the goals set in the treatise:

- The current version of the FNRGF compensates for adaptive noise contained in the images, the compensation rate can be set by the user.
- The filter allows higher scalability, the order of the trigonometric polynomial can be set indirectly by the user by setting the number of angular segments on each circle.

- The filter was newly implemented, the efficiency is by orders faster and enables the user to try different settings of parameters in a short time.
- I did not succeed finding a method to set the attenuation coefficients automatically. The images are too complicated for that. There is no good way to quantify the quality of the enhancement. However, there are tools that allow the user to set the values of the coefficients easily and the computation is optimized so that the re-computation after a change of attenuation coefficients is quick and the user can optimize the settings visually. Furthermore, there is a possibility for unexperienced users to choose a setting that gives results better than the NRGF and works for all images, even though an experienced human user can find a better setting that gives more detailed images.

In some cases, I was not successful in fulfilling the goals set in the treatise. These cases are also documented in the thesis together with comments on how I tried to solve the problems and why the solution did not work. Among them is improving the continuity of the filter in radial direction and full automation of setting the attenuation coefficients.

Even though the filter was improved very much since its first publication, there are still things that are worth experimenting. They will be a subject of further research. Namely:

- The segments can be eliminated from the procedure. The values of all pixels on one Sun-centered circle can be used instead of pixel value averages. The standard deviations can be computed in segments that will be shifting along the circles. Since there would be no segments, the order of the trigonometric polynomial could be much higher, enabling higher adaptivity of the filter – even finer details could be enhanced. On one hand, this would slow the procedure very much, on the other hand, it would only slow the part that is computed once. Changing the attenuation coefficients would not require this part to be recomputed.
- The standard deviation can be also computed after subtracting the Fourier approximation of pixel values (possibly of a lower order) from the pixel values. This solution would reflect better the sense of the standard deviation, in the current solution the averages and standard deviations remove partially the same feature, the local changes of brightness. This would also slow the computation, since the current version computes the averages in segments as by-products of the standard deviation.
- Smoothing the radial profile of the filter. One option is changing completely the principle of the filter – to use one global function of two variables instead of separate functions for each height. This would remove the artifacts similar to rings on a gramophone disk that are visible in some of the processed images. A disadvantage of the solution would probably be losing the extreme adaptivity in the radial direction.
- Further optimization of the computation – parallelization of processes.
- Extending the computation to circles that do not lie completely in the image.
- Applying a non-linear pixel value transformation on the original image before computing its linear combination with the filtered image (gamma transformation, logarithm, ...). The processed images would be more realistic in the sense that there

would be stronger feeling of the brightness decrease in the radial direction while preserving the adaptivity for enhancing faint structures in the corona.

- Use suitable quantiles (their estimates) in stead of the estimate of mean to subtract from the pixel values. This would subtract the background, e.g. the influence of the sky and possibly the K-corona.

Bibliography

Author's publications

- [aDrD14] MILOSLAV, Druckmüller and Hana DRUCKMÜLLEROVÁ. A Noise Adaptive Fuzzy Equalization Method with Variable Neighborhood for Processing of High Dynamic Range Images in Solar Corona Research. Accepted in *Lecture Notes in Computer Science*.
- [aDru05] DRUCKMÜLLEROVÁ, Hana. A new numerical method for solar corona image processing. *I.A.P.P.P. Communications*. 2005, No. 99, pp. 1-4.
- [aDMH11] DRUCKMÜLLEROVÁ, Hana, Huw MORGAN, and Shadia R. HABBAL. ENHANCING CORONAL STRUCTURES WITH THE FOURIER NORMALIZING-RADIAL-GRADED FILTER. *The Astrophysical Journal*. 2011-08-20, Vol. 737, No. 2, pp. 88-97. ISSN 0004-637x. DOI: 10.1088/0004-637X/737/2/88. Available from: <http://stacks.iop.org/0004-637X/737/i=2/a=88?key=crossref.5dd91db1442b5fc7799beb6953ba19ff>
- [aDru10] DRUCKMÜLLEROVÁ, Hana. *Phase-correlation based image registration*. Brno, 2010. Available from: https://www.vutbr.cz/www_base/zav_prace_soubor_verejne.php?file_id=27760. Master thesis. Faculty of Mechanical Engineering, Brno University of Technology. Supervisor Jana Procházková.
- [aHDM11] HABBAL, Shadia R., Miloslav DRUCKMÜLLER, Huw MORGAN, Adalbert DING, Judd JOHNSON, Hana DRUCKMÜLLEROVÁ, Adrian DAW, Martina ARNDT, Martin DIETZEL, and Jon SAKEN. THERMODYNAMICS OF THE SOLAR CORONA AND EVOLUTION OF THE SOLAR MAGNETIC FIELD AS INFERRED FROM THE TOTAL SOLAR ECLIPSE OBSERVATIONS OF 2010 JULY 11. *The Astrophysical Journal*. 2011, Vol. 734, No. 2, pp. 120-137. ISSN 0004-637x. DOI: 10.1088/0004-637X/734/2/120. Available from: <http://stacks.iop.org/0004-637X/734/i=2/a=120?key=crossref.7d305176173b49b98d661d855fa560b0>
- [aKoD13] KONEČNÝ, Zdeněk and Hana DRUCKMÜLLEROVÁ. PHASE-CORRELATION BASED MEASUREMENT OF SOLAR ROTATION RATE. In: *19th International Conference on Soft Computing, MENDEL 2013*. Brno: Brno University of Technology, Faculty of Mechanical Engineering, 2013, pp. 331-336. ISBN 978-80-214-4755-4.

- [aMaD11] MARTIŠEK, Karel and Hana DRUCKMÜLLEROVÁ. A NUMERICAL METHOD FOR THE VISUALIZATION OF THE Fe XIV EMISSION IN THE SOLAR CORONA USING BROADBAND FILTERS. *The Astrophysical Journal Supplement Series*. 2011-12-01, Vol. 197, Issue 2. DOI: 10.1088/0067-0049/197/2/23. Available from: <http://stacks.iop.org/0067-0049/197/i=2/a=23?key=crossref.625f7b4750cfa8ce2cb8372dc300184c>

Scientifically less trustable references

Especially web links, listed to give a more complete overview of the topic.

- [bDrD09] DRUCKMÜLLER, Miloslav and Hana DRUCKMÜLLEROVÁ. Instructions for 2009 TSE. [online]. 18. 3. 2009 [cit. 2013-02-08]. Available from: http://www.zam.fme.vutbr.cz/~druck/eclipse/TSE2009_Instructions.pdf
- [bDru03] DRUCKMÜLLEROVÁ, Hana. *Počítačové zpracování obrazů sluneční korony*. Brno, 2003. Středoškolská odborná činnost. Gymnázium, Brno-Řečkovice. Supervisor Dalibor Kott.
- [bDŠD08] SOFO, Miloslav DRUCKMÜLLER, Pavel ŠTARHA and Hana DRUCKMÜLLEROVÁ. *Adaptive Contrast Control: Image Structure and Object Analyzer, version 6.1*. Brno, 2008, 135 pp.

Other references

- [cASC05] ASCHWANDEN, Markus J. *Physics of the Solar Corona: an Introduction with Problems and Solutions*. 2nd edition. Berlin, Heidelberg: Praxis Pub., Chichester, UK, 2005. ISBN 35-403-0766-4.
- [cBaO07] BADALYAN, O. G. and V. N. OBRIDKO. To the problem of solar coronal heating. *Astronomy Letters*. 2007, Vol. 33, No. 3. ISSN 1063-7737. DOI: 10.1134/S106377370703005X. Available from: <http://www.springerlink.com/index/10.1134/S106377370703005X>
- [cBJS88] BEZVODA, Václav, Josef JEŽEK, Stanislav SAIC, and Karel SEGETH. *Dvojměrná diskrétní Fourierova transformace a její použití: I. Teorie a obecné užití*. First edition. Praha: Státní pedagogické nakladatelství, n. p., 1988, 181 pp. ISBN 17-135-88.
- [cBHK95] BRUECKNER, G. E., R. A. HOWARD, M. J. KOOMEN, C. M. KORENDYKE, D. J. MICHELS, J. D. MOSES, D. G. SOCKER, K. P. DERE, P. L. LAMY, A. LLEBARIA, M. V. BOUT, R. SCHWENN, G. M. SIMNETT, D. K. BEDFORD, and C. J. EYLES. The Large Angle Spectroscopic Coronagraph (LASCO). *Solar Physics*. 1995, Vol. 162, Issue 1-2, pp. 357-402. ISSN 0038-0938. DOI: 10.1007/BF00733434. Available from: <http://link.springer.com/10.1007/BF00733434>

BIBLIOGRAPHY

- [cCLW09] CAIRNS, I. H., V. V. LOBZIN, A. WARMUTH, B. LI, P. A. ROBINSON, and G. MANN. DIRECT RADIO PROBING AND INTERPRETATION OF THE SUN'S PLASMA DENSITY PROFILE. *The Astrophysical Journal*. 2009-12-01, vol. 706, issue 2, L265-L269. DOI: 10.1088/0004-637X/706/2/L265. Available from: <http://stacks.iop.org/1538-4357/706/i=2/a=L265?key=crossref.f88ea206b442b8563e13523978045f6c>
- [cČíž81] ČÍŽEK, Václav. *Diskrétní Fourierova transformace a její použití*. first edition. Praha: SNTL - Nakladatelství technické literatury, n.p., 1981, 160 pp. Matematický seminář SNTL. ISBN 04-019-81.
- [cDAB95] DELABOUDINIÈRE, J. -P., G. E. ARTZNER, J. BRUNAUD, A. H. GABRIEL, J. F. HOCHEDÉZ, F. MILLIER, X. Y. SONG, B. AU, K. P. DERE, R. A. HOWARD, R. KREPLIN, D. J. MICHELS, J. D. MOSES, J. M. DEFISE, C. JAMAR, P. ROCHUS, J. P. CHAUVINEAU, J. P. MARIOGE, R. C. CATURA, J. R. LEMEN, L. SHING, R. A. STERN, J. B. GURMAN, W. M. NEUPERT, A. MAUCHERAT, F. CLETTE, P. CUGNON, and E. L. DESSEL. EIT: Extreme-ultraviolet Imaging Telescope for the SOHO mission. *Solar Physics*. 1995, Vol. 162, 1-2, pp. 291-312. ISSN 0038-0938. DOI: 10.1007/BF00733432. Available from: <http://link.springer.com/10.1007/BF00733432>
- [cDru09a] DRUCKMÜLLER, Miloslav. PHASE CORRELATION METHOD FOR THE ALIGNMENT OF TOTAL SOLAR ECLIPSE IMAGES. *The Astrophysical Journal*. 2009, Vol. 706, No. 2. ISSN 0004-637X. DOI: 10.1088/0004-637X/706/2/1605. Available from: <http://stacks.iop.org/0004-637X/706/i=2/a=1605?key=crossref.6052059cb0fc7aae880ee12a3552e6a2>
- [cDru13] DRUCKMÜLLER, Miloslav. A NOISE ADAPTIVE FUZZY EQUALIZATION METHOD FOR PROCESSING SOLAR EXTREME ULTRAVIOLET IMAGES. *The Astrophysical Journal Supplement Series*. 2013, vol. 207, issue 2, s. 25-29. DOI: 10.1088/0067-0049/207/2/25. Available from: <http://stacks.iop.org/0067-0049/207/i=2/a=25?key=crossref.7c1a4ee3e6e36dffddd5ce0b18daa7eb>
- [cDru09b] DRUCKMÜLLEROVÁ, Zdena. *Korekce pozadí zobrazení fáze v digitálním holografickém mikroskopu užitím konvoluce*. Brno, 2009. Available from: https://www.vutbr.cz/wwwbase/zav_prace_soubor_verejne.php?file_id=28198. Bachelor thesis. Faculty of Mechanical Engineering, Brno University of Technology. Supervisor Hana Uhlířová.
- [cDRM06] DRUCKMÜLLER, Miloslav, Vojtech RUŠIN, and Milan MINAROVJECH. A new numerical method of total solar eclipse photography processing. *Contributions of the Astronomical Observatory Skalnaté Pleso*. Vol. 36, No. 3, pp. 131-148. Available from: <http://adsabs.harvard.edu/abs/2006CoSka...36..131D>

- [cEsp00] ESPENAK, Fred. Digital Compositing Techniques for Coronal Imaging. In: LIVINGSTON, W. and Atila ÖZGÜÇ. *The last total solar eclipse of the millennium in Turkey*. San Francisco: Astronomical Society of the Pacific, 2000, pp. 101-112. ISBN 1-58381-032-3. Available from: <http://adsabs.harvard.edu/abs/2000ASPC..205..101E>
- [cFol92] FOLLAND, Gerald B. *Fourier analysis and its applications*. Providence: American Mathematical Society, 1992, 433 pp. Pure and applied undergraduate texts. ISBN 978-0-8218-4790-9.
- [cGoP10] GOLUB, Leon and Jay M. PASACHOFF. The Solar Corona. 2nd edition. New York: Cambridge University Press, 2010, xiv, 390 pp. ISBN 05-218-8201-X.
- [cHMJ07] HABBAL, Shadia R., Huw MORGAN, Judd JOHNSON, Martina ARNDT, Adrian DAW, Sarah JAEGGLI, Jeff KUHN a Don MICKEY. Localized Enhancements of Fe +10 Density in the Corona as Observed in Fe xi 789.2 nm during the 2006 March 29 Total Solar Eclipse. *The Astrophysical Journal*. 2007, Vol. 663, No. 1, pp. 598-609. DOI: 10.1086/518403. Available from: <http://stacks.iop.org/0004-637X/663/i=1/a=598>
- [cHDM10a] HABBAL, Shadia R., Miloslav DRUCKMÜLLER, Huw MORGAN, Isabelle SCHOLL, Vojtech RUŠIN, Adrian DAW, Judd JOHNSON, and Martina ARNDT. TOTAL SOLAR ECLIPSE OBSERVATIONS OF HOT PROMINENCE SHROUDS. *The Astrophysical Journal*. 2010, Vol. 719, No. 2. ISSN 0004-637x. DOI: 10.1088/0004-637X/719/2/1362. Available from: <http://stacks.iop.org/0004-637X/719/i=2/a=1362?key=crossref.8f2748fc791c7661d1ab453824136d2b>
- [cHDM10b] HABBAL, Shadia R., Miloslav DRUCKMÜLLER, Huw MORGAN, Adrian DAW, Judd JOHNSON, Adalbert DING, Martina ARNDT, Ruth ESSER, Vojtech RUŠIN, and Isabelle SCHOLL. MAPPING THE DISTRIBUTION OF ELECTRON TEMPERATURE AND Fe CHARGE STATES IN THE CORONA WITH TOTAL SOLAR ECLIPSE OBSERVATIONS. *The Astrophysical Journal*. 2010, Vol. 708, No. 1, pp. 1650-1662. ISSN 0004-637x. DOI: 10.1088/0004-637X/708/2/1650. Available from: <http://stacks.iop.org/0004-637X/708/i=2/a=1650?key=crossref.517117e2b43fab770e1a275d646b38bc>
- [cHMT09] HE, Jiansen, Eckart MARSCH, Chuanyi TU, and Hui TIAN. EXCITATION OF KINK WAVES DUE TO SMALL-SCALE MAGNETIC RECONNECTION IN THE CHROMOSPHERE?. *The Astrophysical Journal*. 2009-11-10, Vol. 705, No. 2, L217-L222. ISSN 0004-637x. DOI: 10.1088/0004-637X/705/2/L217. Available from: <http://stacks.iop.org/1538-4357/705/i=2/a=L217?key=crossref.7ddb042f17070973c7ede88761d371c2>
- [HuN01] HUNTER, John K. and Bruno NACHTERGAELE. *Applied Analysis*. 1st edition. World Scientific Publishing Company, 2001. ISBN 978-9812705433.

BIBLIOGRAPHY

Available from:

<https://www.math.ucdavis.edu/~hunter/book/pdfbook.html>

- [cKTV09] KIENREICH, I. W., M. TEMMER a A. M. VERONIG. STEREO QUADRATURE OBSERVATIONS OF THE THREE-DIMENSIONAL STRUCTURE AND DRIVER OF A GLOBAL CORONAL WAVE. *The Astrophysical Journal*. 2009, Vol. 703, č. No, L118-L122. ISSN 0004-637x. DOI: 10.1088/0004-637X/703/2/L118. Available from: <http://stacks.iop.org/1538-4357/703/i=2/a=L118?key=crossref.b90b1419248a81841886fcb89a3d53a8>
- [cKEG95] KOHL, J. L., R. ESSER, L. D. GARDNER, S. R. HABBAL, P. S. DAIGNEAU, E. F. DENNIS, G. U. NYSTROM, A. PANASYUK, J. C. RAYMOND, P. L. SMITH, L. STRACHAN, A. A. VAN BALLEGOOLJEN, G. NOCI, S. FINESCHI, M. ROMOLI, A. CIARAVELLA, A. MODIGLIANI, M. C. E. HUBER, E. ANTONUCCI, C. BENNA, S. GIORDANO, G. TONDELLO, P. NICOLSI, G. NALETTO, C. PERNECHELE, D. SPADARO, G. POLETO, S. LIVI, O. VON DER LÜHE, J. GEISS, J. G. TIMOTHY, G. GLOECKLER, A. ALLEGRA, G. BASILE, R. BRUSA, B. WOOD, O. H. W. SIEGMUND, W. FOWLER, R. FISHER a M. JHABVALA. The Ultraviolet Coronagraph Spectrometer for the solar and heliospheric observatory. *Solar Physics*. 1995, Vol. 162, 1-2, pp. 313-356. DOI: 10.1007/BF00733433. Available from: <http://link.springer.com/10.1007/BF00733433>
- [cKom01] KOMRSKA, Jiří. *Fourierovské metody v teorii difrakce a ve strukturní analýze*. 1st edition. Brno: VUTIU, 2001, 222 s. ISBN 80-214-2011-1.
- [cKSK78] KOUTCHMY, S., G. STELLMACHER, O. KOUTCHMY, N. I. DZUBENKO, V. I. IVANCHUK, O. S. POPOV, G. A. RUBO, S. K. VSEKHSVIATSKII, and P. LAMY. Photometrical analysis of the June 30, 1973 solar corona. *Astronomy and Astrophysics*. 1978, Vol. 69, pp. 35-42. Available from: http://adsabs.harvard.edu/cgi-bin/nph-data_query?bibcode=1978A%26A...69...35K&link_type=ARTICLE&db_key=AST&high=4fc70b223d049333
- [cKKN88] KOUTCHMY, Olga, Serge KOUTCHMY, Christian NITSCHHELM, Július SÝKORA, and Raymond N. SMARTT. Image processing of coronal pictures. In: *Solar and stellar coronal structure and dynamics: Proceedings of the Ninth Sacramento Peak Summer Symposium*. Alrock, R. C. Sunspot, NM, U.S.A.: National Solar Observatory, 1988, pp. 256-266. Available from: <http://adsabs.harvard.edu/abs/1988sscd.conf..256K>
- [cKuH75] KUGLIN, C. D. and D. C. HINES. The Phase Correlation Image Alignment Method. In: *Proceedings of 1975 International Conference on Cybernetics and Society*. New York: IEEE Conference on Cybernetics and Society, 1975, pp. 163-165.

- [cLiM82] LIKEŠ, Jiří and Josef MACHEK. *Počet pravděpodobnosti*. 1st edition. Jarmila Novotná. Praha: SNTL - Nakladatelství technické literatury, n.p., 1982, 160 pp. Matematika pro vysoké školy technické.
- [cLiM83] LIKEŠ, Jiří and Josef MACHEK. *Matematická statistika*. 1st edition. Jarmila Novotná. Praha: SNTL - Nakladatelství technické literatury, n.p., 1983, 180 s. Matematika pro vysoké školy technické.
- [cLyo32] LYOT, Bernard. Étude de la couronne solaire en dehors des éclipses. Avec 16 figures dans le texte. *Zeitschrift für Astrophysik*. 1932, Vol. 5, pp. 73-95.
Available from: <http://adsabs.harvard.edu/abs/1932ZA.....5...73L>
- [cMHW06] MORGAN, Huw, Shadia R. HABBAL, and Richard WOO. The Depiction of Coronal Structure in White-Light Images. *Solar Physics*. 2006, Vol. 236, No. 2, pp. 263-272. ISSN 0038-0938. DOI: 10.1007/s11207-006-0113-6. Available from: <http://www.springerlink.com/index/10.1007/s11207-006-0113-6>
- [cMoH07] MORGAN, Huw and Shadia R. HABBAL. Are solar maximum fan streamers a consequence of twisting sheet structures?. *Astronomy and Astrophysics*. 2007, Vol. 465, No. 3, L47-L50. ISSN 0004-6361. DOI: 10.1051/0004-6361:20077126. Available from: <http://www.aanda.org/10.1051/0004-6361:20077126>
- [cNew61] NEWKIRK, Gordon, Jr. The Solar Corona in Active Regions and the Thermal Origin of the Slowly Varying Component of Solar Radio Radiation. *The Astrophysical Journal*. 1961, vol. 133, pp. 983-1013. DOI: 10.1086/147104. Available from: <http://adsabs.harvard.edu/doi/10.1086/147104>.
- [cNDS70] NEWKIRK, Gordon, Robert G. DUPREE, and Edward J. SCHMAHL. Magnetic fields and the structure of the solar corona: II: Observations of the 12 November 1966 Solar Corona. *Solar Physics*. 1970, Vol. 15, No. 1, pp. 15-39. ISSN 0038-0938. DOI: 10.1007/BF00149469. Available from: <http://www.springerlink.com/index/10.1007/BF00149469>
- [cOwS67] OWAKI, Naoaki and Kuniiji SAITO. Photometry of the Solar Corona at the 1962 February Eclipse. *Publications of the Astronomical Society of Japan*. 1967, Vol. 19, pp. 279-289. Available from: <http://adsabs.harvard.edu/abs/1967PASJ...19..279O>
- [cPra01] PRATT, William K. *Digital image processing: PIKS inside*. 3rd edition. New York: Wiley, 2001, xix, 735 pp. ISBN 04-713-7407-5.
- [cReC96] REDDY, B. Srinivasa. and B.N. CHATTERJI. An FFT-based technique for translation, rotation, and scale-invariant image registration. *IEEE Transactions on Image Processing*. 1996, vol. 5, issue 8, pp. 1266-1271. DOI: 10.1109/83.506761. Available from: <http://ieeexplore.ieee.org/lpdocs/epic03/wrapper.htm?arnumber=506761>
- [cRDA10] RUŠIN, V., M. DRUCKMÜLLER, P. ANIOL, M. MINAROVJECH, M. SANIGA, Z. MIKIĆ, J. A. LINKER, R. LIONELLO, P. RILEY, and

BIBLIOGRAPHY

- V. S. TITOV. Comparing eclipse observations of the 2008 August 1 solar corona with an MHD model prediction. *Astronomy and astrophysics*. 2010, Vol. 513, id. A45. ISSN 1432-0746. DOI: 10.1051/0004-6361/200912778. Available from: <http://www.aanda.org/10.1051/0004-6361/200912778>
- [cSta02] STAUNING, Peter. High-voltage power grid disturbances during geomagnetic storms. In: *Solspa 2001, Proceedings of the Second Solar Cycle and Space Weather Euroconference*. Huguetta Sawaya-Lacoste. Vico Equense, Italy: Noordwijk: ESA Publications Division, 2002, pp. 521-524. ESA Special Publication, 477. ISBN 92-9092-749-6. Available from: http://adsabs.harvard.edu/cgi-bin/nph-data_query?bibcode=2002ESASP.477..521S&link_type=ARTICLE&db_key=AST&high=
- [cStW75] STEIN, Elias M and Guido L WEISS. *Introduction to Fourier analysis on Euclidean spaces*. Princeton, N.J.: Princeton University Press, 1975, 297 pp. ISBN 06-910-8078-X.
- [cWil01] WILLIAMS, David. *Weighing the odds: a course in probability and statistics*. New York: Cambridge University Press, 2001, 547 pp. ISBN 05-210-0618-X.
- [cZad65] ZADEH, Lotfi A. Fuzzy sets. *Information and Control*. 1965, vol. 8, issue 3, pp. 338-353. DOI: 10.1016/S0019-9958(65)90241-X. Available from: <http://linkinghub.elsevier.com/retrieve/pii/S001999586590241X>
- [cZiF03] ZITOVÁ, Barbara and Jan FLUSSER. Image registration methods: a survey. *Image and Vision Computing*. 2003, vol. 21, issue 11, pp. 977-1000. DOI: 10.1016/S0262-8856(03)00137-9. Available from: <http://linkinghub.elsevier.com/retrieve/pii/S0262885603001379>
- [cŽBF98] ŽÁRA, Jiří, Bedřich BENEŠ, and Petr FELKEL. *Moderní počítačová grafika*. 1st edition. Praha: Computer Press, 1998, xvi, 448 pp. ISBN 80-722-6049-9.

Scientifically less trustable references

Especially web links, listed to give a more complete overview of the topic.

- [dCbu06] CBURNETT. File:Bayer pattern on sensor.svg: From Wikipedia, the free encyclopedia. *Wikipedia, the Free Encyclopedia* [online]. 2006 [cit. 2014-03-30]. Available from: http://en.wikipedia.org/wiki/File:Bayer_pattern_on_sensor.svg
- [dCor04] CORLAN, Radu. CCD Reduction. *GCX User's Manual: Version 0.7.6 December 7, 2004* [online]. 2004, 2004-12-10 [cit. 2013-07-16]. Available from: <http://astro.corlan.net/gcx/html/node7.html>.
- [dDpr08] Canon EOS 450D (EOS Rebel XSi / EOS Kiss X2). *Digital Photography Review* [online]. 2008 [cit. 2013-06-20]. Available from: http://www.dpreview.com/products/canon/slrs/canon_eos450d/specifications.

- [dDru07] DRUCKMÜLLER, Miloslav. Total solar eclipse 1980, India: Slovak Academy of Sciences expedition. Eclipse Photography Homepage: by Miloslav Druckmüller [online]. 2007, 2010-03-10 [cit. 2013-06-19]. Available from: <http://www.zam.fme.vutbr.cz/~druck/eclipse/Ecl1980i/0-info.htm>
- [dDru08] DRUCKMÜLLER, Miloslav. Inner corona. *Eclipse Photography Home Page: by Miloslav Druckmüller* [online]. 2008, 2009-03-19 [cit. 2013-03-11]. Available from: http://www.zam.fme.vutbr.cz/~druck/eclipse/Ecl2008r/Tse2008_tsa102_1/0-info.htm
- [dDru09] DRUCKMÜLLER, Miloslav. Fe XIV emission on/off line animation. *Eclipse Photography Home Page by Miloslav Druckmüller* [online]. 2009, 2009-10-09 [cit. 2014-02-21]. Available from: http://www.zam.fme.vutbr.cz/~druck/eclipse/Ecl2008m/Tse2008_green_line1/0-info.htm
- [dDru10] Corona up to 3.5 solar radii. DRUCKMÜLLER, Miloslav. *Eclipse Photography Homepage by Miloslav Druckmüller* [online]. 2010, 2010-09-27 [cit. 2014-03-18]. Available from: http://www.zam.fme.vutbr.cz/~druck/eclipse/Ecl2010t/Tse2010t_1000mm_1/Hr/Tse2010t_wrr1.png
- [dDru13] DRUCKMÜLLER, Miloslav. Input data and examples of NAFE processing. *NAFE Image Analyzer 1.0* [online]. 2013 [cit. 2014-03-07]. Available from: <http://www.zam.fme.vutbr.cz/~druck/nafe/Data/0-info.htm>
- [dEsp07] ESPENAK, Fred. T06-cmp105bw.JPG. *2006 Total Solar Eclipse - Photo Gallery A* [online]. 2006, 2007-01-27 [cit. 2013-08-07]. Available from: <http://www.mreclipse.com/SEphoto/TSE2006/image/T06-cmp105bw.JPG>
- [dEsA08] ESPENAK, Fred and Jay ANDERSON. *Annular and Total Solar Eclipses of 2010*. Greenbelt, Maryland: National Aeronautics and Space Administration, 2008, 77 pp. Available from: <http://eclipse.gsfc.nasa.gov/SEpubs/2010/TP214171a.pdf>
- [dFle11] FLECK, Bernhard. Fact sheet: SOHO. *SOHO: Solar and Heliospheric Observatory* [online]. 2003, 2011-01-19 [cit. 2013-08-02]. Available from: http://sohowww.nascom.nasa.gov/about/docs/SOHO_Fact_Sheet.pdf
- [dGre12] GREEKGEEK. *If the Massive Solar Flare of 1859 (the "Carrington Flare") Happened Today...* [online]. 2012, 2012-11-10 [cit. 2012-12-28]. Available from: <http://greekgeek.hubpages.com/hub/massive-solar-flare-1859>
- [dGur10] GURMAN, Joseph B. The SOHO Extreme ultraviolet Imaging Telescope. *Solar Data Analysis Center* [online]. 2010 [cit. 2013-08-02]. Available from: <http://umbra.nascom.nasa.gov/eit/>
- [dGSF13] SDO - Solar Dynamics Observatory. GODDARD SPACE FLIGHT CENTER. *SDO - Solar Dynamics Observatory* [online]. [cit. 2013-08-05]. Available from: <http://sdo.gsfc.nasa.gov/mission/about.php>

BIBLIOGRAPHY

- [dKer01] IMG0008. KERN, Jonathan. NEWKIRK Camera Images Zambia, '01 [online]. 2001 [cit. 2013-02-22]. Available from: <http://touro.ligo-la.caltech.edu/~jkern/Eclipse01/coronalimages/pages/IMG0008.htm>
- [dLMM10] LOCKHEED MARTIN MISSILE & SPACE and THE LOCKHEED MARTIN SOLAR AND ASTROPHYSICS LABS. *Transition Region and Coronal Explorer* [online]. 2010 [cit. 2013-08-02]. Available from: <http://trace.lmsal.com/>
- [dLHM13] Atmospheric Imaging Assembly. LOCKHEED MARTIN. *AIA - Atmospheric Imaging Assembly* [online]. [cit. 2013-08-05]. Available from: <http://aia.lmsal.com/public/instrument.htm>
- [dNov07] NOVÝ, Jindřich. Multican. [online]. 2005, 2007-04-26 [cit. 2013-07-12]. Available from: <http://multican.sourceforge.net/>
- [dROB14] ROYAL OBSERVATORY OF BELGIUM. *Proba 2* [online]. 2014 [cit. 2014-03-03]. Available from: <http://proba2.sidc.be/>
- [dSSG10] Helioseismic and Magnetic Imager. STANFORD SOLAR GROUP. *Helioseismic and Magnetic Imager* [online]. Stanford, California, 2010, 2010-07-13 [cit. 2013-08-05]. Available from: <http://hmi.stanford.edu/>
- [dSte13] *STEREO* [online]. 2013-07-28 [cit. 2013-08-02]. Available from: http://www.nasa.gov/mission_pages/stereo/main/index.html
- [dUSN12] LASCO Calibration Page. U. S. NAVY. *The SOHO/LASCO Instrument Homepage* [online]. 2012-11-06 [cit. 2013-08-05]. Available from: http://lasco-www.nrl.navy.mil/index.php?p=content//level_1/lascocal_index
- [dVso13] *Virtual Solar Observatory* [online]. [cit. 2013-02-06]. Available from: <http://sdac.virtualsolar.org/cgi/search>
- [dWik10] File:SDO first light.png: From Wikipedia, the free encyclopedia. *Wikipedia, the Free Encyclopedia* [online]. 2010 [cit. 2014-03-30]. Available from: http://en.wikipedia.org/wiki/File:SDO_first_light.png
- [dWik13a] Solar and Heliospheric Observatory. WIKIPEDIA CONTRIBUTORS. *Wikipedia* [online]. 2013, 2013-07-16 [cit. 2013-08-02]. Available from: http://en.wikipedia.org/wiki/Solar_and_Heliospheric_Observatory
- [dWik13b] Solar Dynamics Observatory. WIKIPEDIA CONTRIBUTORS. *Wikipedia* [online]. 2013-07-29 [cit. 2013-08-05]. Available from: http://en.wikipedia.org/wiki/Solar_Dynamics_Observatory
- [dWik13c] STEREO. WIKIPEDIA CONTRIBUTORS. *Wikipedia* [online]. 2013, 2013-07-24 [cit. 2013-08-02]. Available from: <http://en.wikipedia.org/wiki/STEREO>

- [dWik13d] TRACE. WIKIPEDIA CONTRIBUTORS. *Wikipedia* [online]. 2013, 2013-04-24 [cit. 2013-08-02]. Available from: <http://en.wikipedia.org/wiki/TRACE>
- [dYoh01] The Yohkoh Satellite. *Solar Flare Theory* [online]. [cit. 2013-08-02]. Available from: <http://hesperia.gsfc.nasa.gov/sftheory/yohkoh.htm>

Used symbols and abbreviations

The following tables contain the list of symbols and abbreviations throughout the thesis, both ordered alphabetically (with a few exceptions). If any symbol or abbreviation used in the text is missing, it is because it is used only locally in a short part of the thesis.

Abbreviations

ACHF	Adaptive circular high-pass filter, see Section 5.2
AIA	Atmospheric Imaging Assembly aboard the Solar Dynamics Observatory, see page 59
C2, C3	second contact, third contact – the beginning and the end of the total solar eclipse
DLSR	digital single-lens reflex (camera)
EIT	Extreme ultraviolet Imaging Telescope aboard the Solar and Heliospheric Observatory, see page 57
EUV	extreme ultra-violet (wavelength ranges)
FNRGF	Fourier normalizing-radial-graded filter, Chapter 6 and [aDMH11]
GUI	graphical user interface
LASCO	Large Angle and Spectrometric Coronagraph aboard the Solar and Heliospheric Observatory, see page 57
NAFE	Noise adaptive fuzzy equalization, see Section 5.4 and [cDru13]
NRGF	Normalizing-radial-graded filter, Section 5.3 and [cMHW06]
SDO	Solar Dynamics Observatory, see page 59
SOHO	Solar and Heliospheric Observatory, see page 56
TSE	total solar eclipse

Symbols

z^*	complex conjugate of number z
$f * g$	convolution of functions f and g , see page 20, or the discrete periodic convolution, see page 23
$a_{r,k}, b_{r,k}$	coefficients of the Fourier series the average values in segments at radius r are approximated with, see Section 6.1.1
A_k, C_k	attenuation coefficients for the trigonometric polynomials for the averages and for the standard deviations, see Section 6.1.2
\mathbb{C}	the set of complex numbers
$c_{r,k}, d_{r,k}$	coefficients of the Fourier series the standard deviations in segments at radius r are approximated with, see Section 6.1.1
$\mathcal{D}, \mathcal{D}^{-1}$	discrete Fourier transform, inverse discrete Fourier transform, see page 20
$f(x, y)$	a gray-scale image (if not stated otherwise), see page 14
$\mathcal{F}, \mathcal{F}^{-1}$	Fourier transform, inverse Fourier transform, see page 18
h	image height, see page 14
$\Im z$	imaginary part of a complex number z
M	domain of a gray-scale image as a function of two variables, see page 14
M_\odot	part of the domain of a gray-scale image that lies inside or on that largest circle
M_\odot	part of M_\odot that lies completely in the corona, i.e. from inside it starts with the smallest circle that lies completely in the corona – $M_\odot = \{[r, \varphi] \subset M_\odot, r \leq r_o\}$
n_s	number of angular segments, indexed by s , see Section 6.1.1
\mathbb{N}	the set of numbers $1, 2, 3, \dots$
\mathbb{N}_0	the set of numbers $0, 1, 2, \dots$
$O = [o_x, o_y]$	coordinates of the center of the Sun in the image, $O = [o_x, o_y] \in (0, w) \times (0, h)$
(r, φ)	polar coordinates of point (x, y) with origin in the center of the Sun in the image, see Section 3.1.2
r_o	radius in pixels of the smallest circle that lies completely in the corona
R	image of a gray-scale image as a function of two variables, see page 14
R_\odot	solar radius (numbers of solar radii measured from the center of the Sun if not stated otherwise)
$\Re z$	real part of a complex number z
Round	rounding to the nearest integer
w	image width, see page 14
\mathbb{Z}	the set of integers, i.e. numbers $\dots, -2, -1, 0, 1, 2, \dots$
$\rho(A, B)$	distance between points A and B , i.e. ρ is the Euclidean metric unless stated otherwise
ω	order of the trigonometric polynomial in FNRGF, see Section 6.1.1

Appendix A

Enclosed CD

The CD enclosed to the thesis contains:

- The doctoral thesis in a pdf file with active cross-references.
- The FNRGF software with source codes and auxiliary files, **FNRGF.exe** is the application, input data can be downloaded from [dVso13].
- BIFview – a simple viewer of BIF files and some types of FITS files.